HYDRAULIC ANALYSIS OF TRANSIENT FLOWS WITH INTERFACE BETWEEN PRESSURIZED AND FREE SURFACE FLOWS AND ITS APPLICATIONS

HAMID BASHIRI ATRABI

2015

HYDRAULIC ANALYSIS OF TRANSIENT FLOWS WITH INTERFACE BETWEEN PRESSURIZED AND FREE SURFACE FLOWS AND ITS APPLICATIONS

HAMID BASHIRI ATRABI

Department of Urban Management

Kyoto University

Submitted in partial fulfillment of the requirements

for the degree of

Doctor of Philosophy

August 2015

Abstract

Hydraulic transients from free surface flow to pressurized flow and vice versa are called mixed flows. These flows can be observed in many hydraulic systems such as hydropower plants tailrace tunnels, drainage systems, qanat tunnels, storm sewers, and irrigation pipes. In this study, the air cavity is due to sudden opening of one end of a filled duct. After opening the gate, the hydraulic transients between the pressurized pipe flow and the free surface flow occur. Entrapped air cavities can be generated in these systems and may increase the pressure and crack the pipe. Thus, in this study, we developed simple, accurate, and efficient numerical models to investigate the characteristics of such kind unsteady flows.

Two fundamental one-dimensional (1D) numerical models are developed for hydraulic transients with the propagation of an interface between the pressurized pipe flow and the free surface flow in rectangular cross-section ducts. These models can be used for air cavities moving in ducts. For calibration and evaluation of the proposed models, we used three test cases. Comparisons between the simulation results and experimental data showed that the proposed model is applicable to predict the water surface profile in the horizontal and inclined rectangular ducts. Disadvantage of this model is that, it cannot reproduce the confined cavity water surface profile properly. A solution is to use Boyle's law to take into account the temporal air pressure change inside the cavity. This model is validated by experimental data. The numerical simulation results revealed that the effects of the pressure drop and air pressure on the entrapped air cavity are significant during the

pipeline emptying.

We also developed a one-dimensional (1D) model for investigation of water surface profile of an entrapped air cavity while emptying water in an initially filled inclined duct. To reproduce a better profile around the cavity front, we developed a pressure drop model. This section focuses on air pressure changes inside the confined cavity to simulate a kind of transient flow with an entrapped air cavity. Without taking into account the pressure drop and air pressure changing, the confined cavity soon vanishes, in contrast to results from previous experiments. Comparisons between the simulated results and experimental data showed that the model can accurately reproduce the water surface profile of an entrapped air cavity while emptying inclined ducts.

In addition to rectangular ducts, we study the air cavity intrusion into horizontal and inclined circular pipes. Laboratory experiments were carried out to observe the negative surge during the depressurization in a circular pipe. To generate the undular bore in a circular pipe, in some cases we used a sharp-crested weir at the open end of the horizontal pipe. For reproducing the undular bore in circular pipes (when depth is greater than the radius), we derived the depth-averaged shallow water equations with the effects of vertical acceleration, which is called the Boussinesq equation. Comparisons of the results that were obtained by using the hydrostatic and Boussinesq momentum equations with the observed data showed that, the computed results were affected significantly by Boussinesq terms. Although many methods have been developed for the air-water flow in circular pipes, the current method is relatively easy for programming and gives good results.

The study of air cavity intrusion is extended by conducting a fundamental study of air-water flow in two directions. A two-dimensional (2D) depth-averaged model is developed to simulate the transient flow from pressurized to free surface flow. In this section, our main goal is investigation of Benjamin bubble in two directions and verification of the proposed 2D model. This kind of flow can be occured due to the rapid movement of a gate. To evaluate the numerical model, we conducted a few experiments in a square box with an L-type gate using air and water as two fluids. The main aim of this study is to simulate the water surface profile near the cavity front and also downstream of it. The two-dimensional numerical simulations were compared with the experimental data. The results showed a good agreement and lead to the conclusion that taking into account the pressure drops at the interfaces are necessary.

Rapid advances in computer technologies persuade the researchers to use more complex CFD models. For more evaluation of 2D Benjamin bubble, we conducted a three-dimensional (3D) model. The model uses the volume of fluid (VOF) method to define fluid regions. A 3D Reynolds-averaged equation with nonlinear URANS turbulence model and standard k-ε model are used to model two-phase flow in rectangular ducts. The CIP-CSL2 method is employed to solve the convection term in the momentum equation and the advection equation of the VOF function. Applicability of the model is validated by comparison with some experimental data, a one-dimensional (1D) Boussinesq model, and a 2D hydrostatic model. 3D computations with URANS-type turbulence model were developed and verified through a series of test problems. The computational results show an acceptable accuracy of the 3D URANS model to a wide range of mixed flow problems in the rectangular duct. The positions of interfaces, front positions of free surface flow, and water surface profiles were simulated well.

Acknowledgements

I am enormously thankful to my supervisor, Professor Takashi Hosoda, for his encouragement, and his material and intellectual supports. I appreciate all his contributions of time, ideas, and funding to make my Ph.D. experience exciting and productive. He has been a source of ideas and knowledge, his wisdom allowed me to direct my research successfully.

Associate Professors Kiyoshi Kishida and Eiji Harada acted as co-supervisors on my thesis. I am extremely thankful for their support and guidance. I express my sincere thanks to Assistant Professor Shinichiro Onda for his continued support and help in purchasing the lab equipment and components. I would like to acknowledge the examiners of my thesis, Professors Hitoshi Gotoh and Keiichi Toda for their valuable comments to improve my thesis.

The members of the River System Engineering and Management group have contributed immensely to my personal and professional time at Kyoto. The group has been a source of friendships as well as good advice and collaboration. At the risk of leaving someone out, I would specifically like to thank Dr. Puay How Tion, Dr. Hidekazu Shirai, Dr. Manojkumar Namdeo Langhi, Mrs. Kikuko Morisaki, Mr. Sumit Maskey, and all other Japanese students for their friendship, support, and helpful discussions over many issues.

Finally, I would like to thank my parents and wife for their encouragement and love. For my parents who raised me with a love of science and have supported me in all aspects of my life. My loving thanks to my wife for her support and patience during my Ph.D. years. For their support and partnership, I will always be in debt.

Hamid Bashiri Atrabi
Kyoto University
August 2015

Contents

List of Tables

List of Figures

Chapter 1

Introduction

The transition between pressurized flow and free surface flow is one of the interesting topics in mixed-flow conditions. This kind of flow is relevant in many environmental hydraulics and industrial engineering domains. The primary study of this type of flow was conducted by Benjamin (1968) in a rectangular duct. The so-called Benjamin flow has been studying by many researchers since 1968. This transition flow from pressurized to free surface flow (mixed-flow) can be seen in many hydraulic systems (drainage systems, storm sewer systems, hydropower plants, and pipeline pump stations).

Several theoretical and experimental investigations have been done to study this phenomenon in ducts of rectangular cross-section. The earlier studies of such kind of flow were implemented by Zukoskei (1966), Cola (1967), and Benjamin (1968). Laboratory experiments have improved the understanding of this kind of air cavity intrusion into circular pipes since the 1960s. These studies include those of Cola (1967), Benjamin (1968), Cardle et al. (1989), Alves et al. (1993), Hager (1999), Trajkovic et al. (1999), Vasconcelos and Wright (2008), and Bousso and Fuamba (2014).

Benjamin (1968) presented the properties of steady gravity currents by perfect-fluid theory and simple extensions of it. The model of Benjamin was considered as ideal fluid in which the fluid was assumed to be incompressible, and the effects of surface tension and viscosity were assumed to be negligible. Wilkinson (1982) carried out an experimental study of the motion of an air cavity into a long horizontal duct of rectangular cross-section. He studied both the energy-conserving flow and the non-conserving flow. He mentioned that the steady flow is possible only when the water depth beneath the cavity is exactly half or is greater than about 0.78 of the ducts height. Baines and Wilkinson (1986) carried out an investigation on the air propagation into an inclined rectangular duct. They measured and predicted cavity shape of their experiments. A simple model of the flow, based on the theory of steady cavity flow and the classical theory of hydraulic jumps, was developed by Baines et al. (1985). Baines (1991) classified gravity currents by the mode of generation in inclined square ducts into free overfall, lock exchange, controlled buoyancy flux, and finite volume cavity types. Hosoda et al. (1994) investigated the propagation of an interface between open channel flow and pressurized pipe flow in a rectangular duct experimentally and numerically.

In the case of circular pipes, Alves et al. (1993) extended Benjamin's simple approach to the horizontal and inclined circular pipes. They tried to find an approximate approach for the solution of water surface profile equation. Zukoskei (1966) conducted a series of experiments to investigate the influence of surface tension, viscosity, and pipe angle on motion of the bubbles in circular pipes. His experiments were carried out with various pipe diameters with different fluids. He showed that as the surface tension increases the propagation rate decreases.

Several numerical methods were applied to transient flow in free surface-pressurized systems. Bousso et al. (2013) classified numerical modeling of mixed flows in storm water systems according to the solution strategy, air effect, and some equations. According to their study, instabilities in the transition flow regime can be divided to dry bed instability, supercritical-subcritical instability, open channel-pressurized flow instability, fully pressurized instability, and roll wave instability. Vasconcelos and Wright (2008) performed an experimental investigation on air intrusion during flow startup in filled horizontal pipelines. They found that two-component pressure approach (TPA) model can simulate the gradually varying flow. León et al. (2010) proposed a FVM based on a two-equation model to simulate the free surface and pressurized flows. In their model, mixed flows were simulated using two sets of equations, the modified 1D Saint-Venant equations for the free surface regions and the classical 1D compressible water hammer equations for the pressurized regions.

1.1 Motivation

The main objective of this research is developing simple, accurate and applicable methods for simulation of air cavity intrusion into rectangular and circular ducts. Firstly, various flow regimes are investigated experimentally and theoretically and then various numerical models are proposed to simulate such kind of flows inside ducts. We examine hydrostatic and Boussinesq models to reproduce the water surface profile near the cavity front and downstream flow.

In the case of rectangular ducts, we propose a depth-averaged model to simulate the mixed-flow into horizontal and inclined ducts using hydrostatic and Boussinesq assumptions. Also, a solitary wave solution is tested for reproducing the air cavity profile. A damping function and pressure drop are considered in that model.

Afterward, we try to develop a Boussinesq model for circular pipes and conduct some experiments to evaluate the numerical model. We extended our model for 2D Benjamin bubble and carried out experiments to investigate the characteristics of pressurized-free surface flow in two directions. Also, we applied a 3D URANS model to evaluate the 2D model and experimental achievements. The main objectives of our research are summarized below:

I. Develop a hydrostatic simulation model to reproduce the air cavity advancing in a rectangular duct

II. Apply the Boussinesq equation to simulate free surface undulation due to opening a gate

III. Use damping function in Boussinesq model

IV. Evaluate the ability of the numerical models using experimental data

V. Analyze the sensitivity of Boyle's law and pressure drop in front of the cavity on the entrapped cavity

VI. Investigate the air cavity intrusion into horizontal and inclined circular pipes and observation of various types of cavities caused by the mode of generation through experiments

VII. Derive the Boussinesq equations for circular cross section, when the water depth is higher than the pipe radius

VIII. Model the air cavity water surface profile using the Boussinesq model

IX. Present a numerical method to simulate a 2D Benjamin flow in a square box

X. Conduct experiments to observe the propagation of an air cavity in two directions in a square duct

XI. Simulate the mixed-flow using a 3D model

1.2 Organization

This thesis contains detailed theoretical and numerical approaches to investigate the hydraulic transients with an interface between pressurized and free surface flow in rectangular and circular ducts and their applications. The main body of the thesis consists of five chapters followed by the conclusion in the last chapter. The remainder of this thesis is organized as follow:

Chapter 2 presents a theoretical and numerical study of air-water flow in rectangular ducts. The theoretical model is based on Benjamin theory. Two fundamental one-dimensional (1D) models are proposed and applied to simulate the transient flows with the propagation of an interface in a water filled duct. The proposed models are developed to simulate the mixed flows based on a Finite Volume Method (FVM). Finally, the numerical simulations are performed under the hydraulic conditions of previous experiments, and then simulated results are compared with the experimental data.

In chapter 3, the motion of entrapped air cavities in inclined ducts and influence of air pressure on the cavity profile are studied. This chapter focuses on air pressure changes inside the confined cavity to simulate a kind of transient flow with an entrapped air cavity. Results show without taking into account the pressure drop and air pressure changing, the confined cavity soon vanishes, in contrast to results from previous experiments. Comparisons between the simulated results and experimental data show that the model can accurately reproduce the water surface profile of an entrapped air cavity while emptying inclined ducts.

Chapter 4 presents an experimental, theoretical and numerical study of air cavity intrusion into horizontal and inclined circular pipes. Laboratory experiments were carried out to observe a negative surge during the depressurization in a circular pipe. Various behaviors of air cavity in circular pipes were observed according to a series of weir height. Following Benjamin (1968) theory we proposed a relation between front velocity and downstream depth for three types of flow. A fundamental one-dimensional (1D) numerical model is proposed and applied to the cavity flow in a circular pipe. For reproducing the undular bore in circular pipes (when depth is greater than the radius), we have derived the depth-averaged shallow water equations with the effects of vertical acceleration. Finally, the applicability of numerical and theoretical models is validated using experimental data.

Chapter 5 presents an experimental and numerical simulation of transient mixed flow in a rectangular duct. Initially, we extended the experiment of 1D Benjamin flow to the 2D Benjamin flow. We observed an interesting interface shape between pressurized and free surface flow in our experiments. In this chapter, we also present a three-dimensional simulation of transient mixed flows with depressurizing wavefront in a duct. Numerical results showed a good agreement with the experimental data, especially the interface shape.

In chapter 6, a two-dimensional (2D) depth-averaged model is developed to simulate the transient flow from pressurized to free surface flow. This kind of flow can be generated due to the rapid movement of a gate. A fully initially pressurized dam-break experiment is considered to verify the 2D model. The numerical model is based on the hydrostatic pressure distribution in free surface region and the depth-averaged continuity and momentum equations are used for the pressurized flow, free surface flow and the interfaces of both regions. The numerical approach is an interface tracking and after finding the positions of interfaces, a pressure drop is considered at the interfaces. The model can simulate the transition from pressurized flow (pipe flow) to free surface flow that would occur during sudden valve or gate opening. Applicability of the 2D model is validated by comparison with some experimental data.

Finally, Chapter 7 summarizes all the results and the major conclusions drawn from the current study and presents some suggestions for the future research.

1.3 References

Alves, I. N., Shoham, O., and Taitel, Y. (1993). "Drift velocity of elongated bubbles in inclined pipes." *Chem. Eng. Sci.*, 48(17), 3063–3070.

Baines, W. D. (1991). "Air cavities as gravity currents on slope." *J. Hydraul. Eng.*, 117(12), 1600–1615.

Baines, W. D., and Wilkinson, D. L. (1986). "The motion of large air bubbles in ducts of moderate slope." *J. Hydraul. Res.*, 25(3), 313–327.

Baines, W. D., Rottman, J. D., and Simpson, J. E. (1985). "The motion of constant-volume air cavities in long horizontal tubes." *J. Fluid Mech.*, 161, 313–327.

Benjamin, T. B. (1968). "Gravity currents and related phenomena." *J. Fluid Mech.*, 31(2), 209–248.

Bousso, S., Daynou, M., and Fuamba, M. (2013). "Numerical modeling of mixed flows in storm water systems: critical review of literature.” *J. Hydraul. Eng.*, 139(4), 385–396.

Bousso, S., and Fuamba, M. (2014). “Numerical and experimental analysis of the pressurized wave front in a circular pipe.” *J. Hydraul. Eng.*, 140(3), 300–312.

Cardle, J. A., Song, C. C. S., and Yuan, M. (1989). “Measures of mixed transient flows.” *J. Hydraul. Eng.*, 115(2), 169–182.

Cola, R. (1967). “Esame teorico e sperimantale dei fenomeno ondosi di vuotamento di una condotta a sezione circolare.” Atti dell'Istituto Veneto di Scienze, Lettere ed Arti 125, 257–294 (in French).

Hager, W. H. (1999). “Cavity outflow from a nearly horizontal pipe.” *Int. J. Multiphase Flow*, 25, 349–364.

Hosoda, T., Tada, A., Inoue, K., and Kitahara, M. (1994). “Hydraulic analysis of unsteady flows with propagation of an interface between free surface flow and pressurized flow.” *J. Hydraul.*, *Coast. and Envir. Eng.*, JSCE, Japan, No. 503/II-29, 89–97 (in Japanese).

Trajkovic, B., Ivetic, M., and Calomino, F. (1999). “Investigation of transition from free surface to pressurized flow in a circular pipe.” *Wat. Sci. Tech.*, 39(9), 105–112.

Vasconcelos, J. G., and Wright, S. J. (2008). “Rapid flow startup in filled horizontal pipelines.” *J. Hydraul. Eng.*, 134(7), 984–992.

Wilkinson, D. L. (1982). “Motion of air cavities in long horizontal ducts.” *J. Fluid. Mech.*, 118, 109–122.

Zukoski, E. E. (1966). “Influence of viscosity, surface tension, and inclination angle on motion of long bubbles in closed tubes.” *J. Fluid Mech.*, 25(4), 821–840.

León, A. S., Ghidaoui, M. S., Schmidt, A. R., and Garcia, M. H. (2010). “A robust two-equation model for transient mixed flows.” *J. Hydraul. Res.*, 48(1), 44–56.

Chapter 2

One-dimensional depth-averaged model for air-water flow in rectangular ducts

2.1 Introduction

This chapter presents a numerical study of air cavity propagation into a long rectangular duct. The air cavity, which is discussed in this study, is due to sudden opening of one end of a filled duct. After opening the gate, the hydraulic transients between the pressurized pipe flow and the free surface flow occur. Such kind of mixed flows are seen to occur in the power plant tailrace tunnels, storm sewage systems, qanat systems, irrigation systems, and pipelines with air vents or undersized surge tanks (Sundquist and Papadakis, 1983).

Several theoretical and experimental investigations have been done to study this phenomenon in ducts of rectangular cross-section. Benjamin (1968) presented the properties of steady gravity currents by perfect-fluid theory and simple extensions of it. The model of Benjamin was considered as ideal fluid in which the fluid was assumed to be incompressible, and the effects of surface tension and viscosity were assumed to be negligible. Wilkinson (1982) carried out an experimental study of the motion of an air cavity into a long horizontal duct of rectangular cross-section. He studied both the energy-conserving flow and the non-conserving flow. He mentioned that the steady flow is possible only when the water depth beneath the cavity is exactly half or is greater than about 0.78 of the ducts height. Baines and Wilkinson (1986) carried out an investigation on the air propagation into an inclined rectangular duct. They measured and predicted cavity shape of their experiments. A simple model of the flow, based on the theory of steady cavity flow and the classical theory of hydraulic jumps, was developed by Baines et al. (1985). Baines (1991) classified gravity currents by the mode of generation in inclined square ducts into free overfall, lock exchange, controlled buoyancy flux, and finite volume cavity types. Hosoda et al. (1994) investigated the propagation of an interface between open channel flow and pressurized pipe flow in a rectangular duct experimentally and numerically.

The flow regime in the duct with downstream weir and gentle slopes can be dissipative regime which is followed by a bore and developing a train of waves. The dissipative region takes the form of a hydraulic jump, and it may cause a rapid change of depth and generation of turbulence (Wilkinson, 1982; Baines and Wilkinson, 1986; Baines, 1991).

Several numerical methods have been applied to transient flow in free surface-pressurized systems. Bousso et al. (2013) classified numerical modeling of mixed flows in storm water systems according to the solution strategy, air effect, and a number of equations. According to their study, instabilities in the transition flow regime can be divided to dry bed instability, supercritical-subcritical instability, open channel-pressurized flow instability, fully pressurized instability, and roll wave instability. Vasconcelos and Wright (2008) performed an experimental investigation on air intrusion during flow startup in filled horizontal pipelines. They found that two-component pressure approach (TPA) model can simulate the gradually varying flow. León et al. (2010) proposed a FVM based on a two-equation model to simulate the free surface and pressurized flows. In their model, mixed flows were simulated using two sets of equations, the modified 1D Saint-Venant equations for the free surface regions and the classical 1D compressible water hammer equations for the pressurized regions.

It should be pointed out that the Preissmann slot model is not used to track the interface between free surface and pressurized flows in this study. Since the method presented in this paper tracks interface in mixed flows, it falls into the category of interface tracking methods.

This paper aims to: (1) develop a hydrostatic simulation model to reproduce the air cavity advancing in a duct; (2) apply the Boussinesq equation to simulate free surface undulation due to opening a gate; (3) use damping function in Boussinesq model; and (4) evaluate the ability of the numerical models using experimental literature data.

2.2 Numerical Model

2.2.1 Governing equations

The basic model presented herein is composed of the 1D continuity and momentum equations of free surface and pressurized flows and the momentum equation of an interface between both flows. The fundamental 1D model is applied to the Benjamin cavity flow caused by instantaneous opening of a gate as shown in Figure 2.1. The fundamental equations are given as follow

- Free surface open channel flow

Continuity equation

$$\frac{\partial A}{\partial t}+\frac{\partial Q}{\partial x}=0 \tag{2.1}$$

where A = cross-sectional area; t = time; Q = discharge; and x = spatial coordinate.

Momentum equation (Govier and Aziz, 1972; Kimura et al., 2009)

$$\frac{\partial Q}{\partial t}+\frac{\partial uQ}{\partial x}+gA\cos\theta\frac{\partial h}{\partial x}=gA\left(\sin\theta-\frac{\tau_{bx}}{\rho gR}\right)+\frac{\partial(-\overline{u'^2}A)}{\partial x} \tag{2.2}$$

where u = depth-averaged velocity; x = streamwise distance; g = gravitational acceleration; θ = bottom slope of the duct; h = flow depth; τ_{bx} = wall shear stress; ρ = mass density of fluid; R = hydraulic radius; and $\overline{u'^2}$ = turbulence intensity.

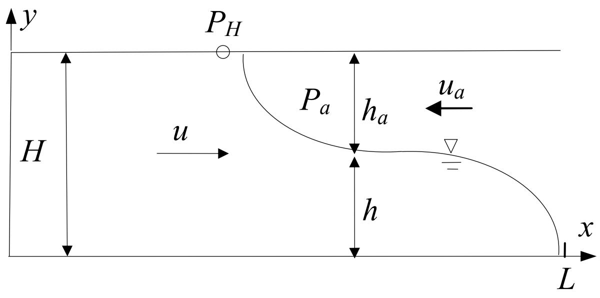

Figure 2.1: Coordinate system.

- Pressurized pipe flow

  Continuity equation

$$\frac{\partial Q}{\partial x} = 0 \tag{2.3}$$

This equation is derived with hypotheses on the homogeneous and incompressible fluid in which the elasticity and changing the cross section are negligible (Yen and Pansic, 1980).

Momentum equation

$$\frac{\partial Q}{\partial t} + \frac{\partial uQ}{\partial x} + gA\frac{\partial}{\partial x}\left(\frac{P_H}{\rho g} + H\cos\theta\right) = gA\left(\sin\theta - \frac{\tau_{bx}}{\rho g R}\right) + \frac{\partial(-\overline{u'^2}A)}{\partial x} \tag{2.4}$$

where P_H = pressure at the top of the duct; and H = duct height.

The wall shear stress is evaluated by Manning's formula (Equation 2.5). In this study, Manning roughness coefficient n = 0.01. The momentum equation at the interface is derived as Equation (2.6) by integrating of Equations (2.2) and (2.4) from $x_{i\text{-}1/2}$ to $x_{i+1/2}$ (Hosoda et al., 1993; Hosoda et al., 1994).

$$\frac{\tau_{bx}}{\rho} = \frac{gn^2u|u|}{h^{1/3}} \tag{2.5}$$

$$\frac{\partial Q}{\partial t}\Delta x+\left(uQ\right)_{x_{i+1/2}}-\left(uQ\right)_{x_{i-1/2}}+gA\left\{h_{i+1/2}-\left(\frac{P_H}{\rho g}+H\right)_{i-1/2}\right\}=$$
$$-gA_{x_i}\Delta x\left(\frac{\tau_{bx}}{\rho gR}\right)_{x_i}+\left(-\overline{u'^2}A\right)_{x_{i+1/2}}-\left(-\overline{u'^2}A\right)_{x_{i-1/2}} \tag{2.6}$$

The oldest proposal for modeling the turbulent or Reynolds stresses is related to Boussinesq's (1877) eddy viscosity concepts. The turbulent or eddy viscosity in contrast to the molecular viscosity is not a fluid property but depends strongly on the state of turbulence (Rodi, 1993). In this investigation, the eddy diffusivity term is evaluated by an empirical formula in the depth-average zero equation model that proposed by Hosoda et al. (1994).

$$\frac{\partial\left(-\overline{u'^2}A\right)}{\partial x}=\frac{\partial}{\partial x}\left(AD_h\frac{\partial u}{\partial x}\right);\quad D_h=\alpha h\left|u\right|;\quad \alpha=0.05 \tag{2.7}$$

where D_h = eddy viscosity; and α = constant coefficient of eddy viscosity that is defined by comparison of observation data and theoretical formula (= 0.05). In idealized flow, the eddy viscosity coefficient must be proportional to the product (hu_*), where u_* = friction velocity. In almost all cases, this coefficient has been in the range of 0.1-1 (Fischer et al., 1979). Since the u is one order less than u_*, the selected value for α falled into this range.

2.2.2 Boussinesq model

In the Boussinesq model, the effects of vertical acceleration of flow which causes the non-hydrostatic distribution of fluid pressure should be included in the momentum equation of open channel flow to reproduce the free surface profile near an interface and undular bore. The Boussinesq model can be achieved by adding following terms to the left-hand side of Equation (2.2). One-dimensional Boussinesq equation is followed as (Iwasa, 1955a; Chaudhry, 1993)

$$\frac{\partial Q}{\partial t}+\frac{\partial uQ}{\partial x}+gA\cos\theta\frac{\partial h}{\partial x}+\frac{\partial}{\partial x}\left(\frac{1}{3}h^2u^2\frac{\partial^2 A}{\partial x^2}+\frac{2}{3}h^2u\frac{\partial^2 A}{\partial t\partial x}+\frac{1}{3}h^2\frac{\partial^2 A}{\partial t^2}\right)$$
$$+\frac{\partial}{\partial x}\left(\frac{1}{3}h^2\frac{\partial u}{\partial t}\frac{\partial A}{\partial x}-\frac{1}{3}hu^2\frac{\partial h}{\partial x}\frac{\partial A}{\partial x}-\frac{1}{3}hu\frac{\partial h}{\partial x}\frac{\partial A}{\partial t}\right)=gA\left(\sin\theta-\frac{\tau_{bx}}{\rho gR}\right)+\frac{\partial\left(-\overline{u'^2}A\right)}{\partial x} \tag{2.8}$$

2.2.3 Consideration of damping function

Turbulence intensity in the vertical direction increases toward the water surface. The damping effect of turbulence near the free surface reduces the vertical fluctuations and length scale causing the parabolic shape of the eddy viscosity. Therefore, to model this effect, the damping function is multiplied by eddy viscosity term in Boussinesq model. The damping function given by Hosoda et al. (1994) is

$$\begin{aligned} f_{damp} &= \exp\left[-\beta\left(\left|\frac{\partial h}{\partial x}\right|_{\max}-\left|\frac{\partial h}{\partial x}\right|_{cr}\right)\right] \quad if \quad \left|\frac{\partial h}{\partial x}\right|_{\max}\geq\left|\frac{\partial h}{\partial x}\right|_{cr} \\ f_{damp} &= 1.0 \qquad\qquad\qquad\qquad\qquad\qquad if \quad \left|\frac{\partial h}{\partial x}\right|_{\max}<\left|\frac{\partial h}{\partial x}\right|_{cr} \end{aligned} \tag{2.9}$$

where β = constant value (= 10); and $\left|\frac{\partial h}{\partial x}\right|_{cr}$ = 0.225 and this value calculated based on the breaking wave condition that has been investigated by Sandover and Zienkiewicz (1957).

2.2.4 Pressure near stagnation point

The pressure P_1 and P_s can be related by applying the Bernoulli equation along the dividing streamline. P_s denotes the pressure at the stagnation point, which is shown in Figure 2.2, is located some distance h_s below the upper boundary. Thus, we have

$$\frac{P_1}{\rho}=\frac{P_s}{\rho}-\frac{c^2}{2}-\frac{\delta}{\rho r}-gh_s \tag{2.10}$$

where c = celerity of the cavity; δ = the surface tension; r = the radius of curvature of

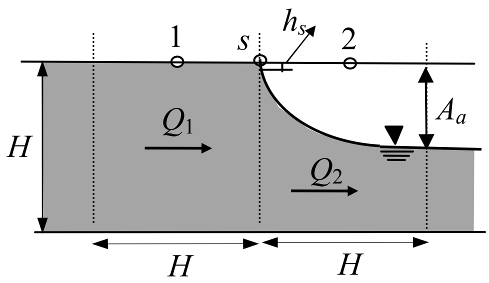

Figure 2.2: Evaluation of pressure near the stagnation point.

the water-air interface at the stagnation point; and subscripts 1 and s refer to the region of flow upstream of the front and stagnation point, respectively. The density of the air is assumed to be negligible compared with water density. Surface tension can noticeably affect the shape and celerity of the cavity (Gardner and Crow, 1970; Wilkinson, 1982). The surface tension and h_s are constants in the same experiments, and the magnitudes of these parameters are given by experimental data. Note that the radius of curvature used in evaluating the surface tension forces is the tube radius (Zukoski, 1966).

The celerity of cavity, surface tension and h_s given by Wilkinson (1982) are

$$c = \kappa \frac{Q_1 - Q_2}{A_a}; \quad (\kappa = 1.0) \tag{2.11}$$

$$\frac{\delta}{\rho g r} = 0.0023 \text{ (m)}, \quad h_S = 0.0015 \text{ (m)} \tag{2.12}$$

where A_a = area of the air above water; and Q_1 and Q_2 are the discharge of water upstream and downstream, respectively.

2.3 Procedure of Numerical Simulation

As mentioned earlier, the flow field is divided into three regions of: (1) free surface open channel flow, (2) pressurized pipe flow, and (3) interface of both flows. Figure 2.3 shows the arrangement of hydraulic variables in the framework of control volume method.

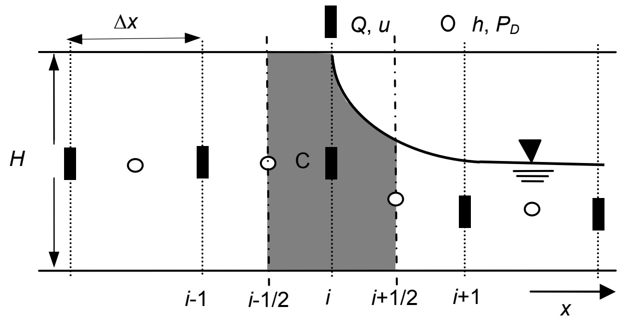

Figure 2.3: Arrangement of the hydraulic variable along the x-axis.

For the free surface open channel flow region, the method of flood invasion analysis in flood plains is used for the time integral of Equations (2.1) and (2.2) (Inoue, 1986). Equations (2.3) and (2.4) are applied to the pressurized flow region to calculate velocities and pressures, by using the HSMAC method for the incompressible fluids (Hirt and Cook, 1972). Supposing that Q and P_H at $t = n.\Delta t$ are known, the hydraulic variables at $t = (n+1).\Delta t$ are calculated according to the following steps:

I. Q^* is calculated by Equation (2.13)

$$\frac{Q^* - Q^n}{\Delta t} = -(\text{inertia term})^n - (\text{pressure term})^n - (\text{wallshear term})^n \quad (2.13)$$

II. Pressure P_H is corrected by Equation (2.14)

$$P_H^* = -P_H^n + \delta P_H^* \quad (2.14)$$

δP_H^* for $P_{H_{i+1/2}}$ is given by

$$\delta P^*_{H_{i+1/2}} = -\frac{\omega \varepsilon^*}{2H\Delta t\left(\frac{1}{\Delta x^2}\right)}; \quad \omega = 0.5 \tag{2.15}$$

$$\varepsilon^* = \frac{Q^*_{i+1} - Q^*_i}{\Delta x} \tag{2.16}$$

III. Q^* is re-calculated by substituting P^*_D into Equation (2.13). If $\left|\varepsilon^*\right|$ is smaller than the criterion error (er = 0.0001), Q^* is considered as Q^{n+1} at $t = (n+1).\Delta t$, otherwise the same procedures of (I) and (II) have to be continued until $\left|\varepsilon^*\right| <$ er.

The Q at the interface C in Figure 2.3 is calculated by Equation (2.6). The position of an interface between free surface flow and pressurized flow and the depth h at $t = (n+1/2).\Delta t$ and u at $t = n.\Delta t$ are known. The depth h at $t = (n+1).\Delta t$ of both the free surface and the control volume bordering, and the interface is calculated by Equation (2.1). If $h^{n+1/2}$ of the free surface region is greater than H, the control volume is regarded as the volume of the pressurized flow region. If $h^{n+1/2}$ of the free surface region is smaller than H, the control volume is going to be free surface region and the new position of an interface is determined. A series of above steps are repeated up to the essential time. The FVM with Harten's TVD scheme for the convective inertia term is adopted as numerical simulation (Harten, 1983). The staggered allocation of depth and discharge is used in a computational grid. Figure 2.4 presents the structure of the proposed model.

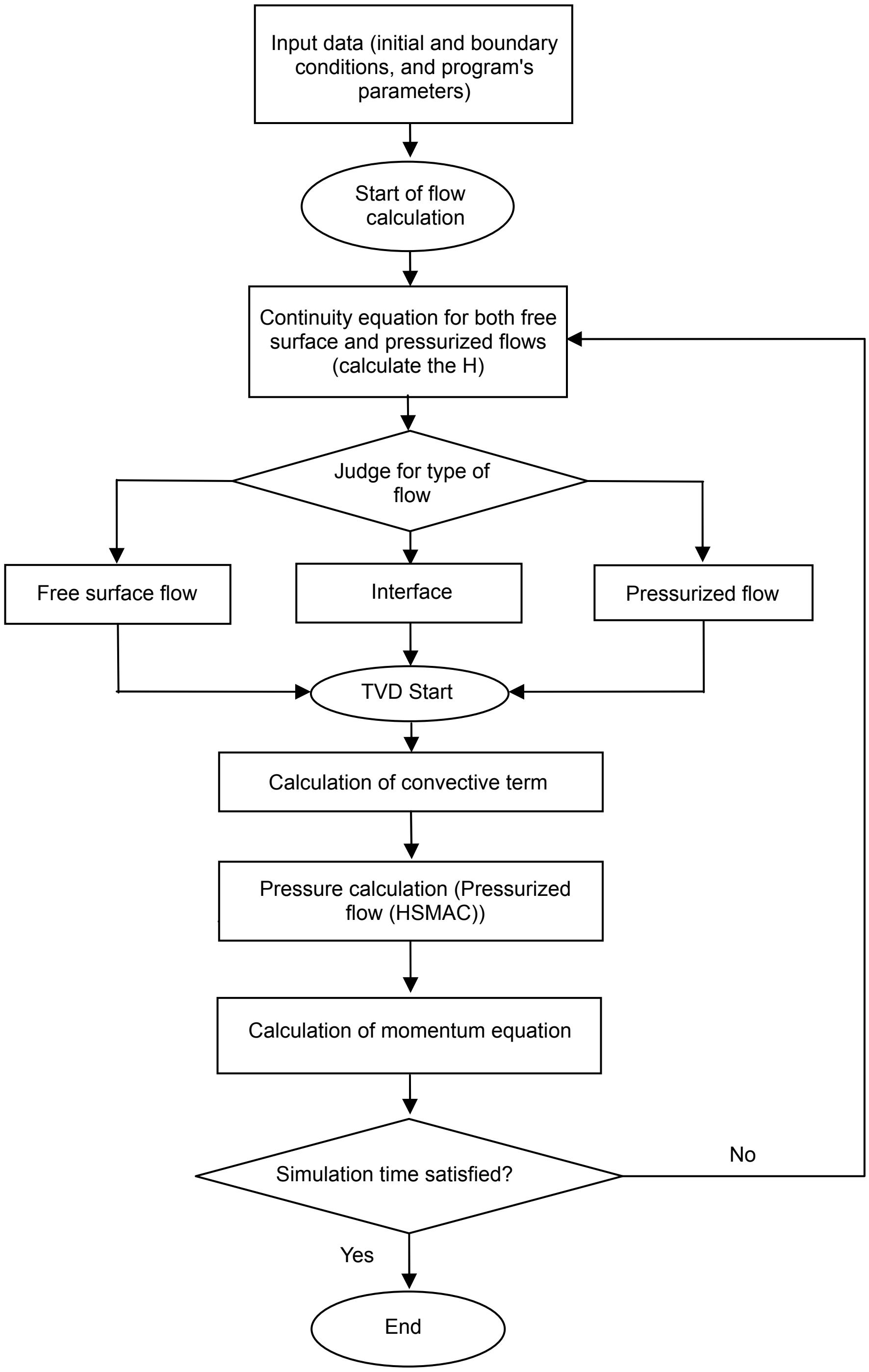

Figure 2.4: Flowchart of the proposed model.

2.4 Results

2.4.1 Effects of model parameters

The sensitivity of the empirical constants of interface length (L_{int}) and interface pressure drop (P_{drop}) are examined for all experiments of Hosoda et al. (1994), Wilkinson (1982), and Baines (1991). These parameters have been used to calculate the pressure in the interface of mixed flow. It should be pointed out that, these parameters didn't apply for the initial stages of the flow (when the cavity initiated its motion) and for short region of the duct near the gate and dead wall. The combination of these parameters was used to get a good agreement with the experimental data. Each model was run 20 times for each case. Table 2.1 shows the values of these parameters that used in the simulations. As a sample, the influences of these parameters on first experiments of Hosoda et al. (1994) are shown in this study. Figures 2.5 and 2.6 show variations of numerical results as a function of model parameters for hydrostatic pressure and Boussinesq models, respectively. Experimental data and numerical simulations show the water surface profile t = 0.6 s after opening the gate. Parameters values that used in each run are shown in Table 2.2. As Figures 2.5 and 2.6 show, run 33 is in good agreement with the experimental data in both hydrostatic pressure and Boussinesq models. According to run 33, the best parameters for hydrostatic and Boussinesq models are $L_{\mathrm{int}} / H = 1$ and $P_{\mathrm{drop}} / H = 1$. To increase the numerical efficiency, reasonable small time steps and a large number of grids are needed.

Table 2.1: Range of constant variables that are considered during the simulation.

Empirical constant variables	Considered ranges
L_{int} / H	0.6, 0.8, 1, 1.2, and 1.4
P_{drop} / H	0, 1, 5, and 10

Table 2.2: Run parameters.

Run number	L_{int} / H	P_{drop} / H
13	1	0
31	0.6	1
32	0.8	1
33	1	1
34	1.2	1
35	1.4	1
53	1	5
73	1	10

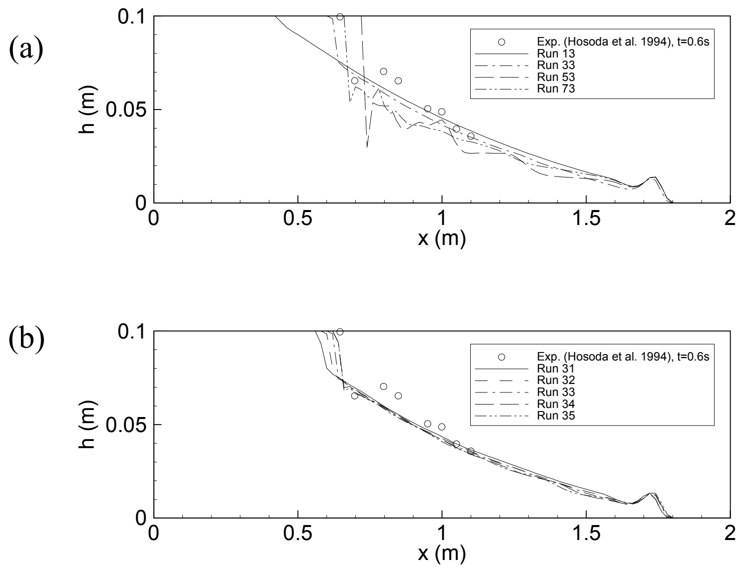

Figure 2.5: Effect of variation of: (a) L_{int} / H; (b) P_{drop} / H on water surface profile in Hydrostatic model (Hosoda et al. 1994, $h_t = 0.0H$, $t = 0.6$ s).

(a)

(b)

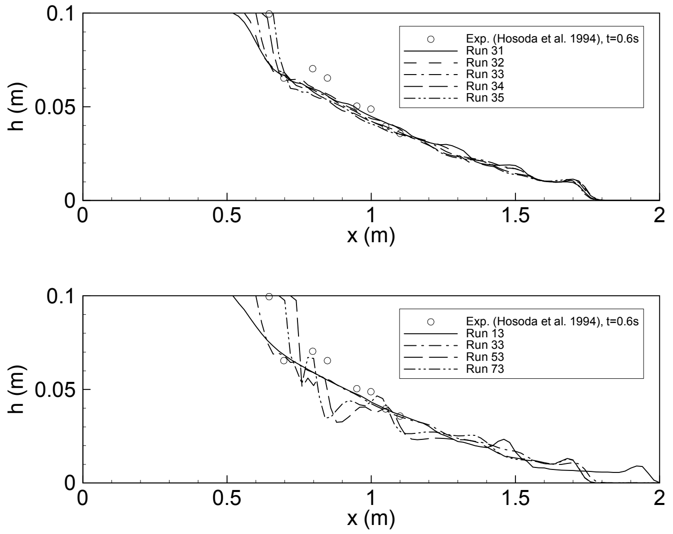

Figure 2.6: Effect of variation of: (a) L_{int} / H; (b) P_{drop} / H on water surface profile in Boussinesq model (Hosoda et al. 1994, $h_t = 0.0H$, $t = 0.6$ s).

2.4.2 Evaluation of model

The purpose of this section is to analyze the model parameters and evaluate the performance of the proposed model to simulate air cavity intrusion into ducts. Three test cases which are considered in this section are as follow:

1. Experiments of Wilkinson (1982) (air cavity in horizontal duct without weir or weir with small height)
2. Experiments of Hosoda et al. (1994) (air cavity in horizontal duct with constant height of water in downstream); and
3. Experiments of Baines (1991) (air cavity in an inclined duct with weir and without weir in the downstream end).

Similar to most mixed flow models, the dry bed challenge can be seen in the practical application of this model. To overcome this difficulty, a minimum depth is added to initial conditions.

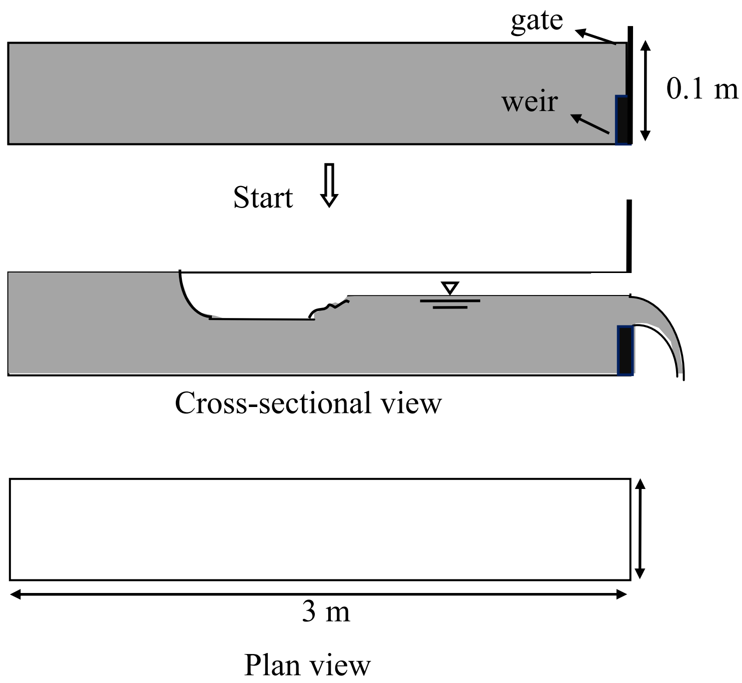

Figure 2.7: Sketch of the experimental setup of Wilkinson (1982).

2.4.2.1 Experiment of Wilkinson

The purpose of this section is to test the ability of the proposed model to simulate the water surface profile and air cavity shape in the horizontal duct without weir or with a short weir. The test considered was conducted by Wilkinson (1982). The setup consisted of a Perspex-walled duct of 3 m long, 0.1 m width and 0.1 m height. One end of the duct was closed, and at the other end a gate was installed. The flow of water from the duct was impeded by a weir located at the open end. The height of the weir in the experiment was 0.333 H (0.0333 m). Figure 2.7 shows the layout of the experimental facility. Downstream Froude number and depth of water were measured in his experiments.

An extended Boussinesq equation that suggested by Hosoda et al. (1994) and Hager (1999) can reproduce the water surface profile of Benjamin cavity in a rectangular cross-section. The solitary wave equation in a rectangular duct that represented by Iwasa (1955b), can reproduce the interface surface profile as Equation (2.17).

$$h_2 = h_1 + \left(\mathrm{Fr}_1^2 - 1\right) h_1 \operatorname{sech}^2 \left[\frac{1}{2h_1} \sqrt{\frac{3\left(\mathrm{Fr}_1^2 - 1\right)}{\mathrm{Fr}_1^2}} x \right] \tag{2.17}$$

where the subscripts 1 and 2 represent the upstream and downstream of the cavity; and x = the horizontal distance from nose of the cavity.

The solitary wave equation and Boussinesq approximation model were used to reproduce the air cavity water surface profile of Wilkinson (1982) experiment (Figure 2.8). As Figure 2.8 shows, Boussinesq model with $P_{\mathrm{drop}} / H = 0$ is in good agreement with solitary wave solution. Also, the Boussinesq model with $P_{\mathrm{drop}} / H = 1$ shows reasonable agreement with experimental data. The simulated water surface profile was obtained using 150 cells, time interval $\Delta t = 0.001$ s and Manning roughness coefficient of $n = 0.01$ m$^{-1/3}$s. The results for the water surface profile along the duct and near the air cavity showed a good agreement between the Boussinesq model, solitary wave solution, and test.

2.4.2.2 Experiments of Hosoda et al.

Here, the proposed model is used to reproduce a set of experiments conducted at the Kyoto University, by Hosoda et al. (1994). The performance of the numerical model is tested to simulate the water surface profile in experiments with a constant level of water in downstream. The experiments were conducted in a tube of 0.1 m height, 0.05 m width, and 2 m length. A vertical gate was installed in the tube 1 m from one end to contain the volume of air. A hand-operated device, which was located in the middle of the duct enabled an operator to withdraw the gate.

The initial heights of water in downstream of the duct were 0.0, 0.5 and 0.7 of the height of the duct. Figure 2.9 shows the layout of the experimental facility. The upstream (left) half of the tube was fully filled with water while the downstream (right) half of the duct was partially filled with water. The air was released into the duct by withdrawing the middle gate. They observed three flow regimes in their experiments; the steady flow regime; the unsteady regime with developing train of waves; and the steady dissipative regime. It was found that with increasing height of water on the right side, the flow depth on the downstream side of the bore and the celerity of the bore also increased.

Simulated results with hydrostatic and Boussinesq models are shown in Figure 2.10. It is pointed out that the results are in good agreement with experimental data with adding vertical acceleration term for the pressure distribution in the momentum equation of free surface open channel flow near the air cavity. It was also found that the Boussinesq model with damping function can reproduce better water surface profile in comparison with other simulation models (Figure 2.11).

As shown in Figure 2.11, the simulated results with damping function can reproduce the better profile of undular bore. The ability of the model to conserve mass is tested in these experiments. The zero flux boundary conditions were used in the experiments of Hosoda et al. (1994), so the total mass in the duct was constant with time. The mass traces in the case with tail water = 0.0 is shown in Figure 2.12. The results show that this model conserves mass.

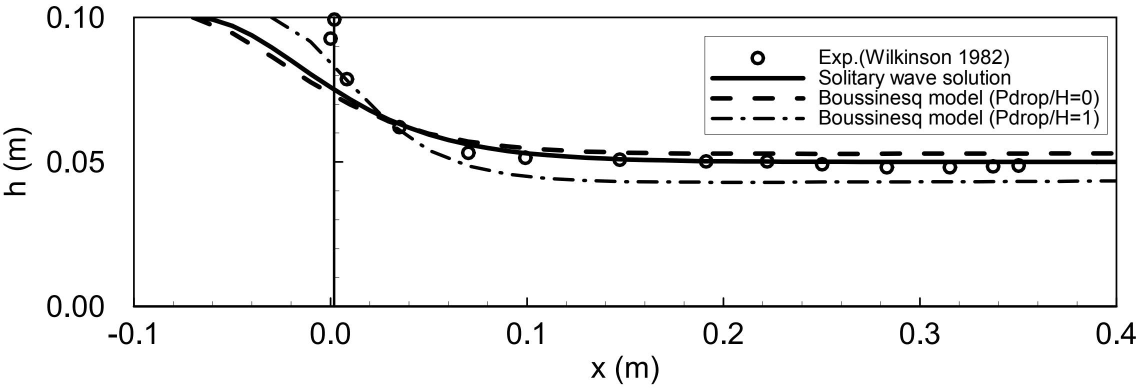

Figure 2.8: Comparison between the solitary wave equation, Boussinesq model, and experiment of Wilkinson (1982).

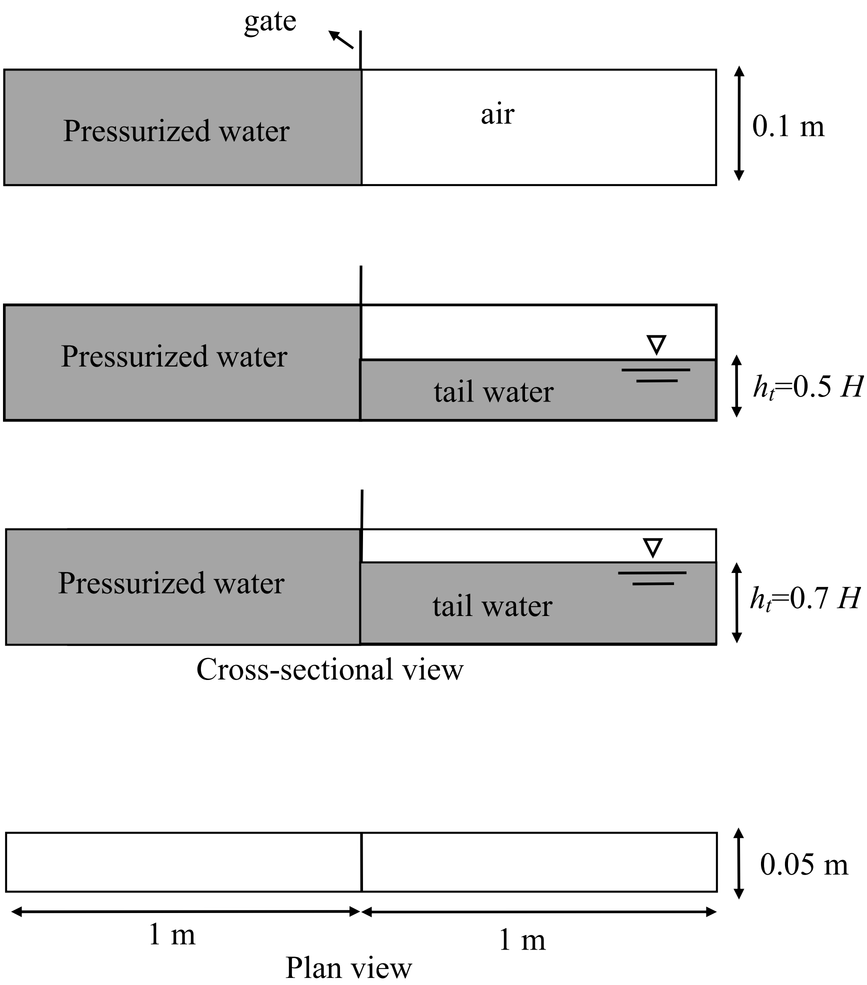

Figure 2.9: Sketch of the experimental setup of Hosoda et al. (1994).

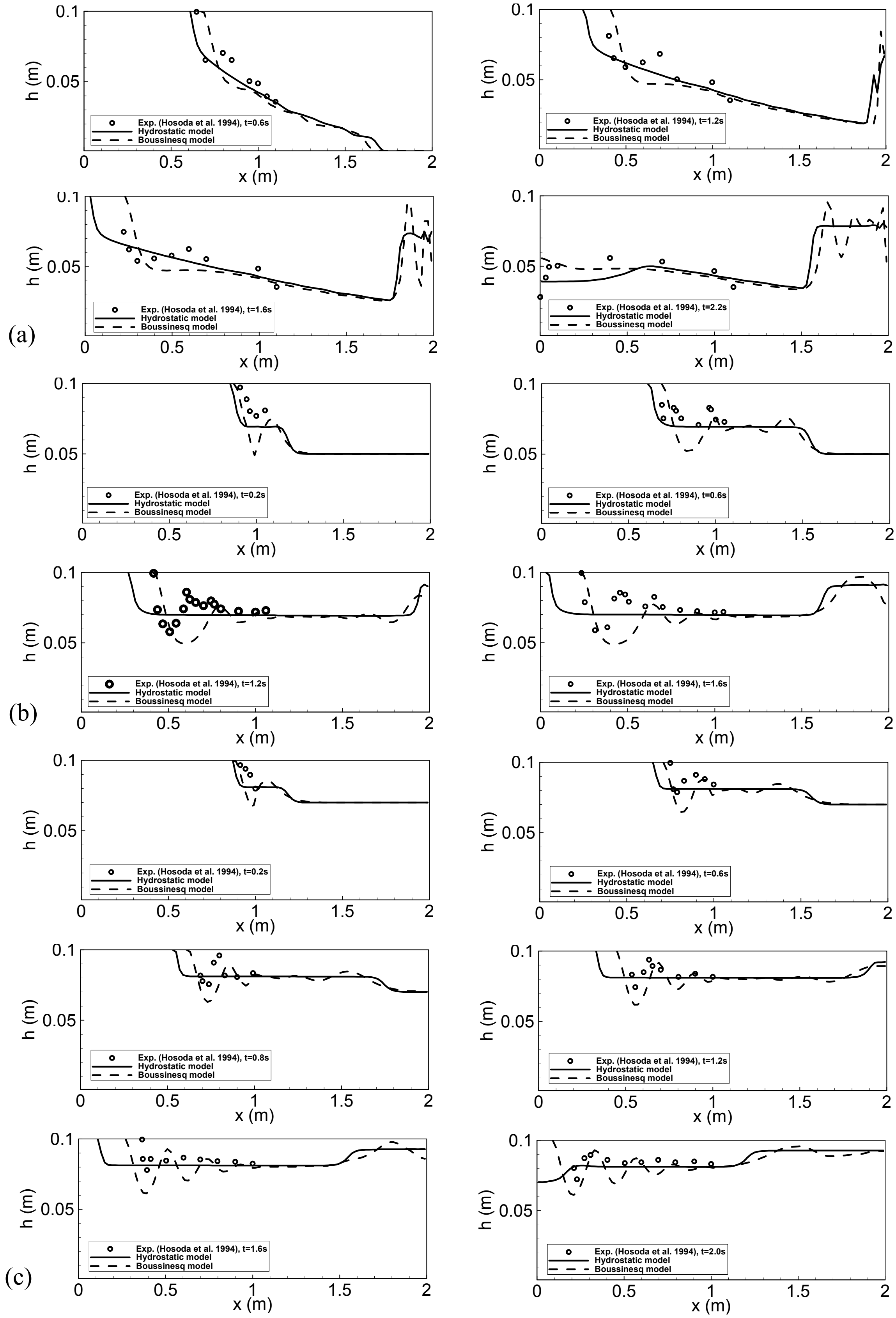

Figure 2.10: Water surface profile for experiments of Hosoda et al. (1994): (a) case with tail water = 0.0; (b) case with tail water = 0.5 H; (c) case with tail water = 0.7 H.

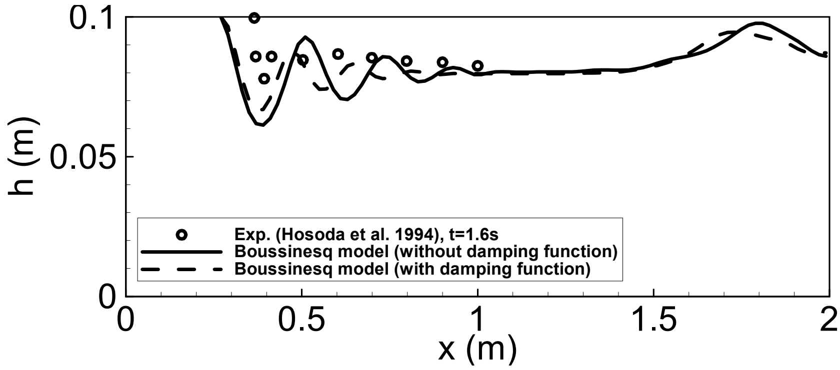

Figure 2.11: Comparison between simulation with damping function and without damping function for Boussinesq model (Hosoda et al. 1994) ($h_t = 0.7\ H$).

2.4.2.3 Experiments of Baines

The tests of Baines (1991) consisted of a 0.1 m square duct and 4 m length. The experiments described the effect of duct slope for the air cavity formed by opening a gate at the downstream end. Figure 2.13 shows the experimental setup of Baines (1991). If there is no weir at the outlet, the flow falls free, and the surface is the smooth curve. A train of waves, which move with a speed less than cavity speed, can be observed in this case. The air cavity water surface profiles on 6˚ slope with free overfall were simulated by the hydrostatic and Boussinesq models. The simulations were done by using Δx = 0.02 and Δt = 0.001. Figures 2.14(a) and 2.14(b) show the results for the air cavity on 6˚ slope with free overfall at t = 1.6 s and t = 2.62 s after gate opening, respectively. As Figure 2.14(a) and 2.14(b) show, the Boussinesq model results are in good agreement with the experimental data. Figure 2.15 shows the flow with a sufficiently high weir to produce a hydraulic jump. In this case, the duct slope was 2˚ and w = 0.5 H. Flow passes from supercritical to subcritical when it reaches the weir. The discharge over the weir was calculated by the weir formula (Rouse, 1946)

$$q = \frac{2}{3} C_d \sqrt{2g} h^{\frac{3}{2}} \tag{2.18}$$

where q = unit discharge; h = weir head (water surface elevation above the weir); and C_d = the discharge coefficient follows by

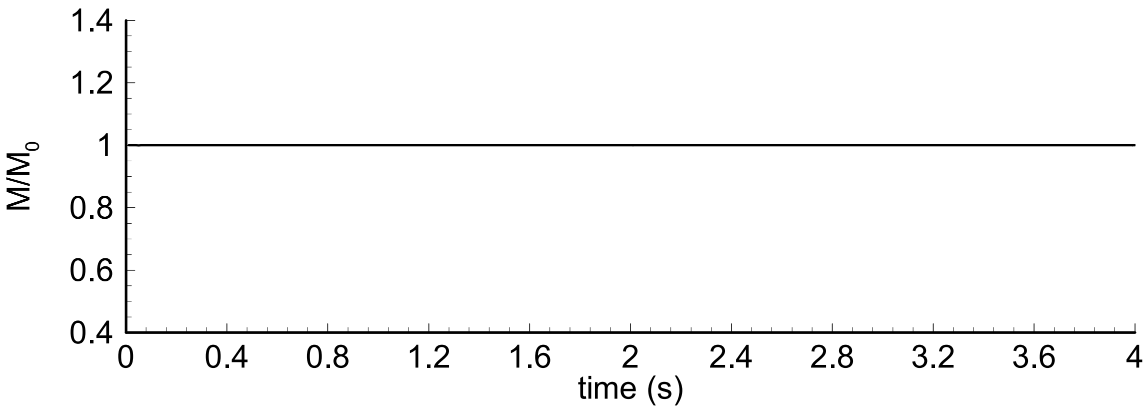

Figure 2.12: Mass traces (Hosoda et al., 1994) (h_t = 0.0).

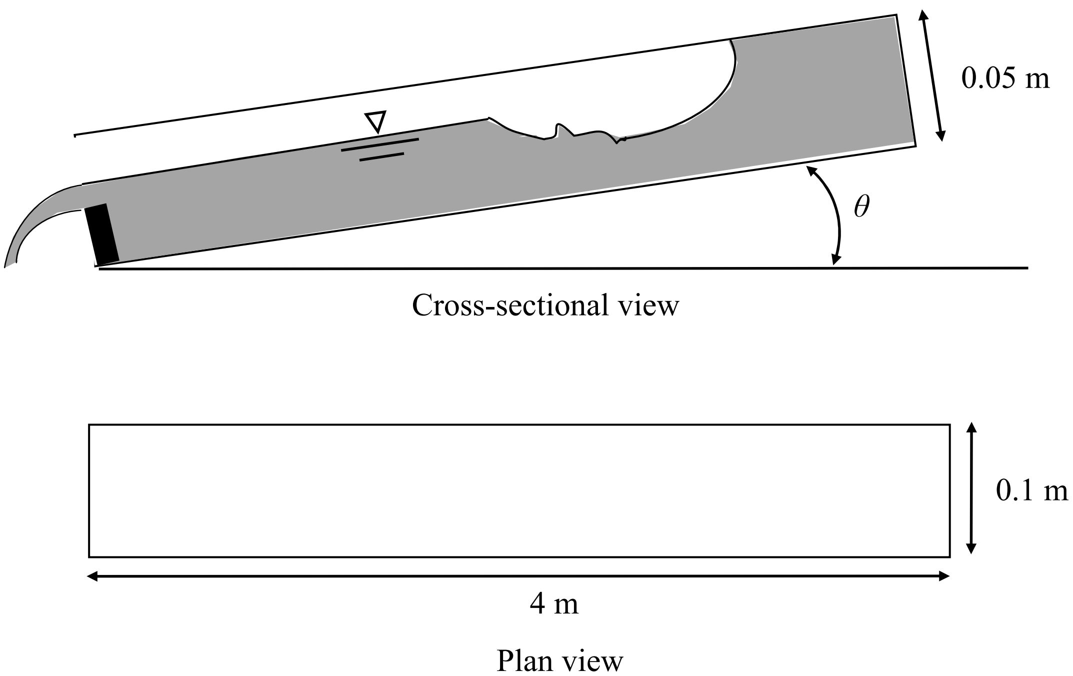

Figure 2.13: Sketch of the experimental setup of Baines (1991).

(a)

(b)

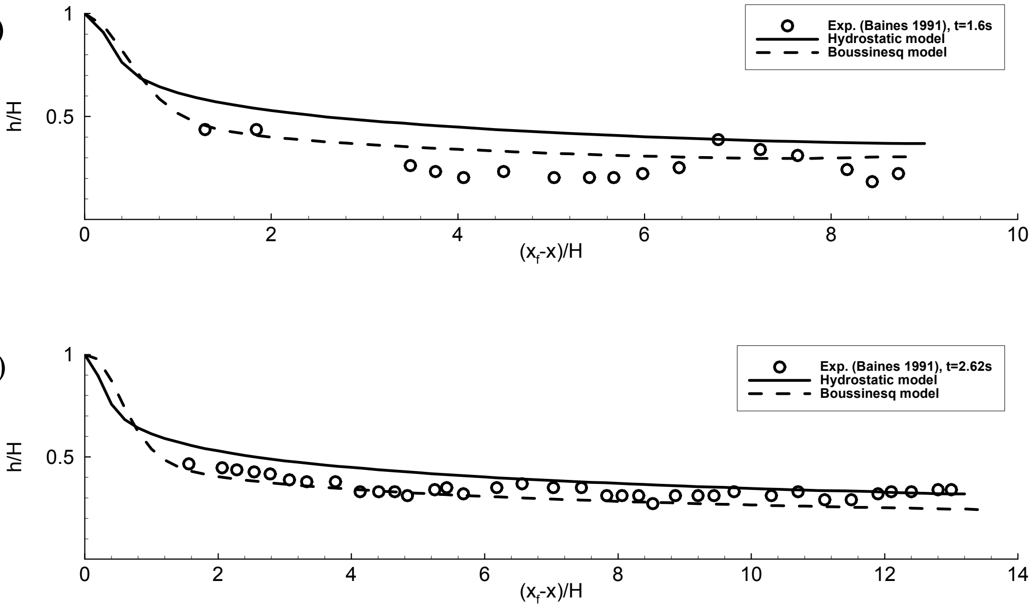

Figure 2.14: Measured and simulated water surface profile on 6° slope with free overfall: (a) t = 1.6 s; (b) t = 2.62 s after gate opening (Baines, 1991).

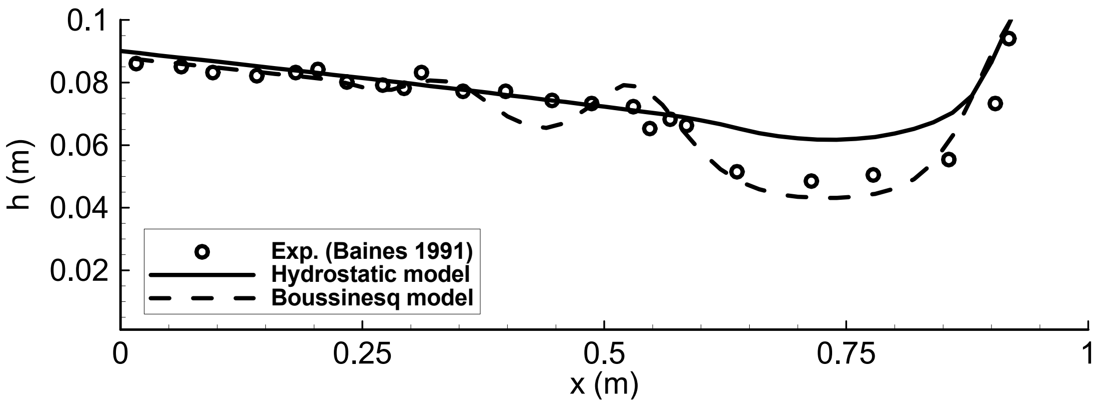

Figure 2.15: Comparison of measured and simulated water surface profile with w / H = 0.5 and θ = 2° (Baines, 1991).

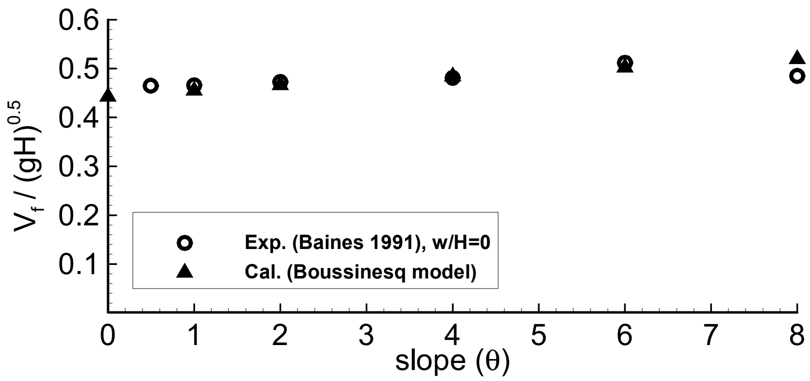

Figure 2.16: Comparison of measured and simulated velocity of the front as a function of channel slope for fronts with a height of $w / H = 0$ (Baines, 1991).

$$C_d = 0.611 + 0.075\frac{h}{w} \tag{2.19}$$

Figure 2.16 shows a plot of the front velocity as a function of slope and includes data for $w = 0$. The results are in good agreement with experimental data. For higher weirs, the jump moves faster than the cavity front.

2.5 Summary

The 1D numerical models were developed for hydraulic transients with the propagation of an interface between the pressurized pipe flow and the open channel free surface flow in rectangular cross-section ducts. The numerical simulation models are proposed to reproduce the surface profile of the unsteady flow and air cavity in the rectangular ducts on the assumption of the incompressible fluids. From comparisons of numerical and theoretical models with the experimental data we concluded:

1. Results showed a good agreement between the solitary wave solution and experiments
2. In contrast to the hydrostatic model, the Boussinesq model can reproduce the

shape of the solitary wave and had a good agreement with experimental data

3. Existence of damping function in Boussinesq model is effective to reproduce the better water surface profile

4. It is pointed out from comparisons between the simulation results and experimental data that the proposed model is applicable to predict the water surface profile in the horizontal and inclined rectangular ducts

Although a good agreement between the model results and the observations tends to validate the proposed models, further studies are essential to illustrate the advantages or disadvantages of the fundamental model in comparison with other numerical models.

2.6 References

Baines, W. D. (1991). "Air cavities as gravity currents on slope." *J. Hydraul. Eng.*, 117(12), 1600–1615.

Baines, W. D., Rottman, J. D., and Simpson, J. E. (1985). "The motion of constant-volume air cavities in long horizontal tubes." *J. Fluid Mech.*, 161, 313–327.

Baines, W. D., and Wilkinson, D. L. (1986). "The motion of large air bubbles in ducts of moderate slope." *J. Hydraul. Res.*, 25(3), 313–327.

Benjamin, T. B. (1968). "Gravity currents and related phenomena." *J. Fluid Mech.*, 31(2), 209–248.

Boussinesq, J. (1877). "Essai sur la théorie des eaux courantes." *Mémoires presents à l'Académie des Sciences*, Paris 23(1), 1–680 (in French).

Bousso, S., Daynou, M., and Fuamba, M. (2013). "Numerical modeling of mixed flows in storm water systems: critical review of literature." *J. Hydraul. Eng.*, 139(4), 385–396.

Chaudhry, M. H. (1993). *Open channel flow*, Prentice-Hall, Englewood Cliffs, N.J.

Fischer, H. B., List, E. J., Koh, R. C. Y., Imberger, J. and Brooks, N. H. (1979). *Mixing in inland and coastal waters*, Academic Press, New York.

Gardner, G. C., and Crow, I. G. (1972). "The motion of large bubbles in horizontal channels." *J. Fluid Mech.*, 43, 247–255.

Govier, G. W., and Aziz, K. (1972). *The flow of complex mixtures in pipes*, Van Nostrand Reinhold Comp., New York.

Hager, W. H. (1999). "Cavity outflow from a nearly horizontal pipe." *Int. J. Multiphase Flow*, 25, 349–364.

Harten, A. (1983). "High resolution schemes for hyperbolic conservation laws." *J. Comput. Phys.*, 49, 357–393.

Hirt, C. W., and Cook, J. L. (1972). "Calculating three-dimensional flows around structures and over rough terrain", *J. Comput. Phys.*, 10, 324–340.

Hosoda, T., Inoue, K., and Iwasa, Y. (1992). "Intrusion process of flood water into underground space." *Annual J Hydraul. Eng.,* JSCE, 36, 317–322.

Hosoda, T., Inoue, K., and Tada, A. (1993). "Hydraulic transient with propagation of interface between open-channel free surface flow and pressurized pipe flow." *Proc. 5th Int. Symp. on Computational Fluid Dynamics*, JSCFD, Sendai, Japan, 1, 291–296.

Hosoda, T., Tada, A., Inoue, K., and Kitahara, M. (1994). "Hydraulic analysis of unsteady flows with propagation of an interface between free surface flow and pressurized flow." *J. Hydraul., Coast. and Envir. Eng.*, JSCE, Japan, No. 503/II-29, 89–97 (in Japanese).

Inoue, K. (1986). "Studies on the numerical methods of the unsteady flows in open channels and their applications in hydraulic engineering." Ph.D. Dissertation, Kyoto University, Japan (in Japanese).

Iwasa, Y. (1955a). "Analytical considerations on cnoidal and solitary waves." *Memoirs of the Fac. of Eng.*, Kyoto Univ., 17(4), 264–276.

Iwasa, Y. (1955b). "Undular jump and its limiting condition for existence." *Proc. 5th Japan National Congress for Applied Mech.*, Japan, II-14, 315–319.

Kimura, I., Uijttewaal, W. S. J., .Hosoda, T., and Shahjahan, A. (2009). "URANS computations of shallow grid turbulence." *J. Hydraul. Eng.*, 135(2), 118–131.

León, A. S., Ghidaoui, M. S., Schmidt, A. R., and Garcia, M. H. (2010). "A robust two-equation model for transient mixed flows." *J. Hydraul. Res.*, 48(1), 44–56.

Rodi, W. (1993). *Turbulence models and their applications in hydraulics*, IAHR Monograph, 3rd Ed., Balkema, Rotterdam, The Netherlands.

Rouse, H. (1946). *Elementary mechanics of fluids*, John Wiley and Sons, New York.

Sandover, J. A., and Zienkiewicz, O. C. (1957). "Experiments on surge waves." *J. Water Power*, 9(11), 418–424.

Sundquist, M. J., and Papadakis, C. N. (1983). "Surging in combined free surface-pressurized systems." *J. Transportation Eng.*, 109(2), 232–245.

Vasconcelos, J. G., and Wright, S. J. (2008). "Rapid flow startup in filled horizontal pipelines." *J. Hydraul. Eng.*, 134(7), 984–992.

Wilkinson, D. L. (1982). "Motion of air cavities in long horizontal ducts." *J. Fluid. Mech.*, 118, 109–122.

Yen, B. C, and Pansic, N., (1980). *Surcharge of sewer systems*, WRE Research Report No. 149, Department of Civil Engineering, University of Illinois at Urbana-Champaign.

Zukoski, E. E. (1966). "Influence of viscosity, surface tension, and inclination angle on motion of long bubbles in closed tubes." *J. Fluid Mech.*, 25, 821–840.

Chapter 3

The motion of confined cavity in an inclined duct

3.1 Introduction

Hydraulic transients from free surface flow to pressurized flow and vice versa (mixed flow) can be observed in many hydraulic systems such as hydropower plants, drainage systems, qanat tunnels, storm sewers, and irrigation pipes. Entrapped air cavities can be generated in these systems and may increase the pressure and crack the pipe.

Finite cavity initiation (gulping) during emptying of water through a duct was investigated by Baines and Wilkinson (1986) and Baines (1991). Baines (1991) conducted experiments by using an inclined square duct of 0.1 m in height and 4 m in length. When the downstream gate was opened, an air cavity was generated and moved. He mounted a weir with heights of 0.5 H (H is the height of the square duct) and 0.75 H at the outlet to observe the confined air cavity motion. Figure 3.1 shows the definition sketch of confined air cavity generation in his experiments. It should be noted that for the generation of a finite cavity, the weir height should be sufficiently high. The shape and motion of a confined cavity depends on the Froude number of flow, depth of flow, pipe slope, pipe roughness, longitudinal cross-section area of the cavity, and buoyancy acceleration (Volkart, 1978; Baines and Wilkinson, 1986).

Many researchers have dealt with the entrapped air pockets experimentally and numerically (Pothof and Clemens, 2010; Pozos et al., 2010; Zhou et al., 2011a; Liu and Yang, 2013). Hosoda et al. (2014) and Bashiri-Atrabi et al. (2015) conducted the

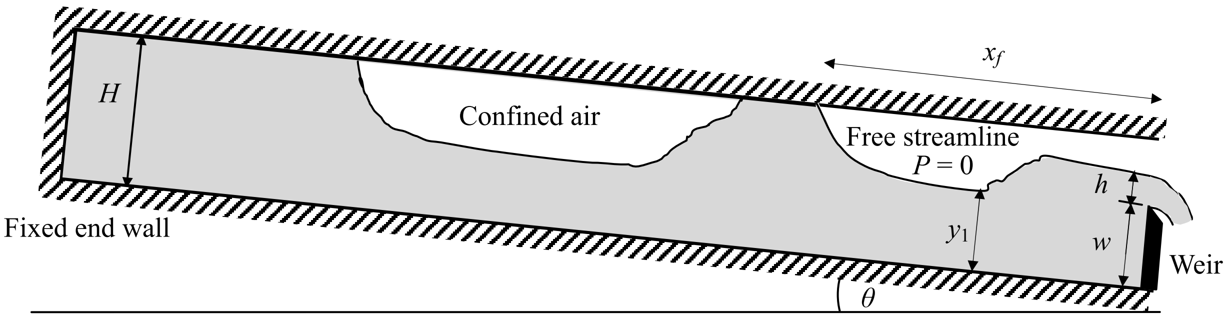

Figure 3.1: Definition sketch of entrapped air cavity.

numerical simulation of an air cavity advancing into a straight duct. Zhou et al. (2011a) investigated pressure variations in a filled pipeline with an entrapped air pocket and indicated that the rigid water model cannot easily predict the pressure when the fraction of the air pocket is small.

Zhou et al. (2011b) applied a Volume of Fluid (VOF) model to simulate the movement of an air pocket and pressure surge in a water filling pipe. They summarized that because of the simplicity and computational efficiency, 2D VOF is more convenient to use for simulation of this flow. Liu and Yang (2013) carried out an experiment in which they studied the transportation of air pockets in a pressurized pipe. They found that the characteristics of the air pocket transport depend on the pipe slope, flow velocity, pipe diameter, pipe roughness and air pocket volume.

In this paper, a Boussinesq equation is used to simulate the confined air cavity surface profile in an inclined duct. The proposed model consists of one-dimensional continuity and momentum equations for open channel flow and pressurized flow, and a momentum equation at the interface of both flows. Although this model was already applied to non-entrapped cavities by Bashiri-Atrabi et al. (2015), this current study aims to assess the performance of the model for entrapped cavities. The sensitivity of Boyle’s law and pressure drop in front of the cavity on the entrapped cavity shape is also discussed here. The accuracy of the model is analyzed with comparisons to the experimental results of Baines (1991).

3.2 Governing Equations

3.2.1 Open channel flow

The one-dimensional form of the continuity and momentum (including the vertical acceleration terms) equations for open channel flow can be written as (Mohapatra and Chaudhry, 2004; Bashiri-Atrabi et al., 2014)

$$\frac{\partial A}{\partial t}+\frac{\partial Q}{\partial x}=0 \tag{3.1}$$

$$\begin{aligned}&\frac{\partial Q}{\partial t}+\frac{\partial uQ}{\partial x}+gA\cos\theta\frac{\partial h}{\partial x}+\frac{\partial}{\partial x}\left(\frac{1}{3}h^2u^2\frac{\partial^2 A}{\partial x^2}+\frac{2}{3}h^2u\frac{\partial^2 A}{\partial t\partial x}+\frac{1}{3}h^2\frac{\partial^2 A}{\partial t^2}\right)\\&+\frac{\partial}{\partial x}\left(\frac{1}{3}h^2\frac{\partial u}{\partial t}\frac{\partial A}{\partial x}-\frac{1}{3}hu^2\frac{\partial h}{\partial x}\frac{\partial A}{\partial x}-\frac{1}{3}hu\frac{\partial h}{\partial x}\frac{\partial A}{\partial t}\right)=gA\left(\sin\theta-\frac{\tau_{bx}}{\rho gR}\right)+\frac{\partial(-\overline{u'^2}A)}{\partial x}\end{aligned} \tag{3.2}$$

where A = the cross-sectional area; Q = the discharge; x = the streamwise distance; t = the time; u = the depth-averaged velocity; h = the flow depth; g = the gravitational acceleration (g = 9.81 ms^{-2}); θ = the bottom slope of the duct; τ_{bx} = the wall shear stress; R = the hydraulic radius; ρ = the density of fluid; and $\overline{u'^2}$ = the depth-averaged Reynolds stress tensor.

The shear stress in Equation (3.2), is calculated by Manning's formula

$$\frac{\tau_{bx}}{\rho}=\frac{gn^2u|u|}{h^{1/3}} \tag{3.3}$$

where n = the Manning roughness coefficient.

3.2.2 Pressurized flow

The continuity and momentum equations for pressurized flow can be written as (Yen and Pansic, 1980)

$$\frac{\partial Q}{\partial x}=0 \tag{3.4}$$

$$\frac{\partial Q}{\partial t}+\frac{\partial uQ}{\partial x}+gA\frac{\partial}{\partial x}\left(\frac{P_H}{\rho g}+H\cos\theta\right)=gA\left(\sin\theta-\frac{\tau_{bx}}{\rho gR}\right)+\frac{\partial(-\overline{u'^2}A)}{\partial x} \tag{3.5}$$

where P_H = the pressure at the top of duct; and H = the duct height. For a duct having constant cross-section and following fully throughout its length, $\frac{\partial u}{\partial x}$ is small and can be neglected.

The momentum equation at the interface is derived by integrating Equations (3.2) and (3.6) from $x_{i\text{-}1/2}$ to $x_{i+1/2}$ as follows (Bashiri-Atrabi et al., 2014).

$$\begin{aligned}&\frac{\partial Q}{\partial t}\Delta x+\left(uQ\right)_{x_{i+1/2}}-\left(uQ\right)_{x_{i-1/2}}+gA\left\{h_{i+1/2}-\left(\frac{P_D}{\rho g}+H\right)_{i-1/2}\right\}=\\&gA_{x_i}\Delta x\left(\sin\theta-\frac{\tau_{bx}}{\rho gR}\right)_{x_i}+\left(-\overline{u'^2}A\right)_{x_{i+1/2}}-\left(-\overline{u'^2}A\right)_{x_{i-1/2}}\end{aligned} \tag{3.6}$$

3.2.3 Confined air cavity

The governing equation for air pressure changing inside the confined air cavity is derived from Boyle's law, which states that when real gases are compressed at a constant temperature, the relationship between the pressure and volume is as follows

$$P_aV_a^{\gamma}=P_0V_0^{\gamma} \tag{3.7}$$

where P_a = the air pressure of the confined cavity; V_a = the air volume of the confined cavity; P_0 = the atmospheric pressure; V_0 = the air volume just before cavity is confined; and γ = the polytropic exponent (γ = 1.4).

$$P_a=P_0+\Delta P_a \tag{3.8}$$

where ΔP_a = the difference between confined air pressure and atmospheric pressure. The change of air pressure inside the confined cavity is evaluated by

$$\Delta P_a = P_0\left(\left(\frac{V_0}{V_a}\right)^{\gamma} - 1\right) \tag{3.9}$$

The following term is added into the momentum equation of open channel flow to take into account the air pressure changes inside the entrapped air

$$-\frac{\partial}{\partial x}\left(\frac{\Delta P_a}{\rho}A\right) + \frac{\Delta P_a}{\rho}B_s\frac{\partial h}{\partial x} \tag{3.10}$$

where B_s = the water surface width.

3.2.4 Pressure drop

The influence of pressure drop on air cavity front shape was examined in a non-confined cavity in a rectangular duct. As Bashiri-Atrabi et al. (2015) showed, it is necessary to consider the appropriate pressure drop using the following equations

$$\frac{P_D}{\rho g} = H - \frac{c^2}{2g} - h_s - \frac{\delta}{\rho g r} \tag{3.20}$$

$$c = \kappa\frac{Q_1 - Q_2}{A_a}; \quad (\kappa = 1.0) \tag{3.21}$$

where h_s = the stagnation point displacement; δ = the surface tension; r = the radius of curvature of the air-water interface at the stagnation point; c = the cavity celerity; A_a = the air area above the water; and κ = the coefficient of pressure drop (κ = 1).

3.3 Solution Method

Numerical simulation with the basic equations is done under the conditions of laboratory experiments carried by Baines (1991).

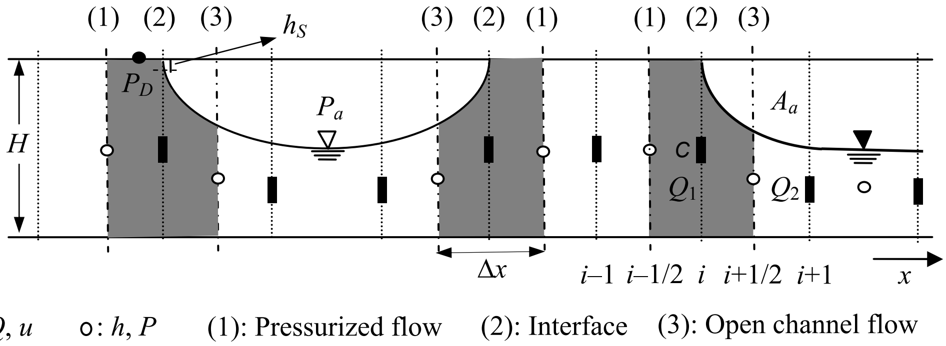

Figure 3.2: Definition sketch of the hydraulic variable along the x-axis with staggered grid system.

The initial and boundary conditions of calculations are (At t = 0.0):

- Initial condition: $Q = 0$, $h = H$
- Boundary condition (upstream and downstream ends): $Q = 0$, $h = H$

For $t > 0.0$, the values of q are calculated at the downstream boundary condition by the following equation (Rouse, 1946)

$$q = 0.666 C_d \sqrt{2g} h_w^{1.5} \tag{3.22}$$

$$C_d = 0.611 + 0.075 \frac{h_w}{w} \tag{3.23}$$

where q = the unit discharge; h_w = the water surface elevation above the weir; w = the weir height; and C_d = the discharge coefficient.

A finite volume numerical formulation is used to solve the governing conservation of mass and motion equations. As shown in Figure 3.2, a staggered grid system was used for simulations. A method of flood inundation in flood plains was used for the free surface flow by time integration of Equations (3.1) and (3.2) (Hosoda et al., 1993). For pressurized flow, Equations (3.5) and (3.6) were used by the HSMAC iteration method (Hirt and Cook, 1972). The Harten TVD scheme developed by Harten (1983) has been used to deal with the proposed model in this study. For further information about the numerical model, please refer to Bashiri-Atrabi et al. (2015). Basic parameters in this simulation are: $H = 0.1$ m, $L = 4$ m, $w = 0.5\ H$, $\dfrac{\delta}{\rho g r} = 0.0023$ m, $h_s = 0.0015$ m, g = 9.8 (ms^{-2}), $n = 0.01$ m$^{-1/3}$s, $\Delta t = 0.001$ s, and $\Delta x = 0.02$ m.

3.4 Results

For evaluation of air pressure effects on the water surface profile, we used the same model that we explained in the section 2.2. We used the experimental condition of Baines (1991) and same parameters for the models with and without air pressure. The influence of pressure drop on non-confined air cavity water surface profile is shown in Figure 3.3. The result shows that the simulated water surface profile using pressure drop ($\kappa = 1$) is in good agreement with the experimental data of Baines (1991). In his experiment, the weir height was 50% of the duct height and $\theta = 2^\circ$.

To evaluate the model, calculated a temporal variation of cavity front location is plotted to compare with the experimental data of Baines (1991) in Figure 3.4 ($w = 0.5\ H$, $\theta = 1$). Furthermore, comparisons of simulated results with experimental data for depth at the toe of jump and depth at weir are shown in Figure 3.5.

To verification of the model for a confined cavity, the experimental conditions of Baines (1991) are used to simulate the entrapped air cavity water surface profile (Figure 3.6(a)). Figure 3.6(b) gives a comparison between the computed entrapped air cavity water surface profile when air pressure is, and is not, included.

The comparison indicates that the volume of the cavity without considering Boyle's law is more than when Boyle's law is factored in. Simulation results show that after a few seconds the entrapped cavity seals without taking not account Boyle's law. As Figure 3.6(c) shows, considering pressure drop in front of the entrapped air is necessary.

Figure 3.7 shows calculated results for the experiments by Baines (1991) with a 2°

slope and $w = 0.5\ H$. The time interval between Figures 3.7(a) and 3.7(b) is 0.33 s. The results indicate that the model can reproduce the shape and movement of a confined air cavity effectively.

As Figures 3.8(a) and 3.8(b) show, temporal volume and pressure variations in a simulation when considering Boyle's law is evident, and the effect of that law is to cause the confined cavity to conserve its volume and prevent it from vanishing rapidly.

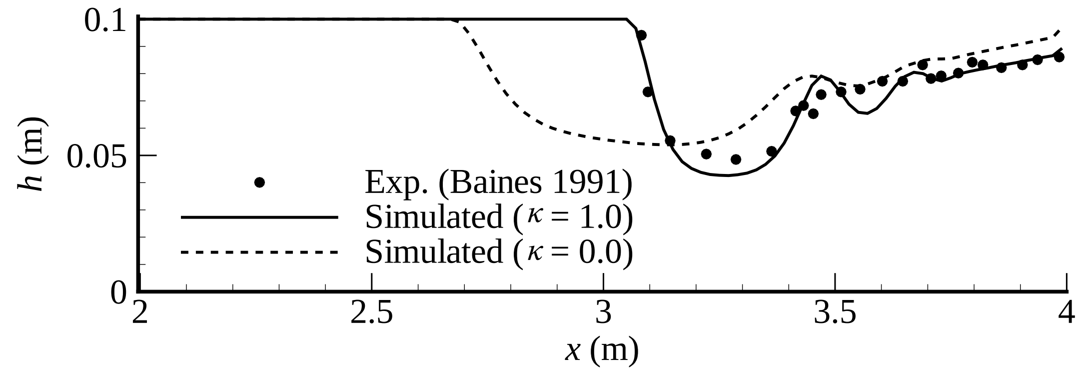

Figure 3.3: Water surface profile using pressure drop ($\kappa = 1.0$) and without using pressure drop ($\kappa = 0.0$).

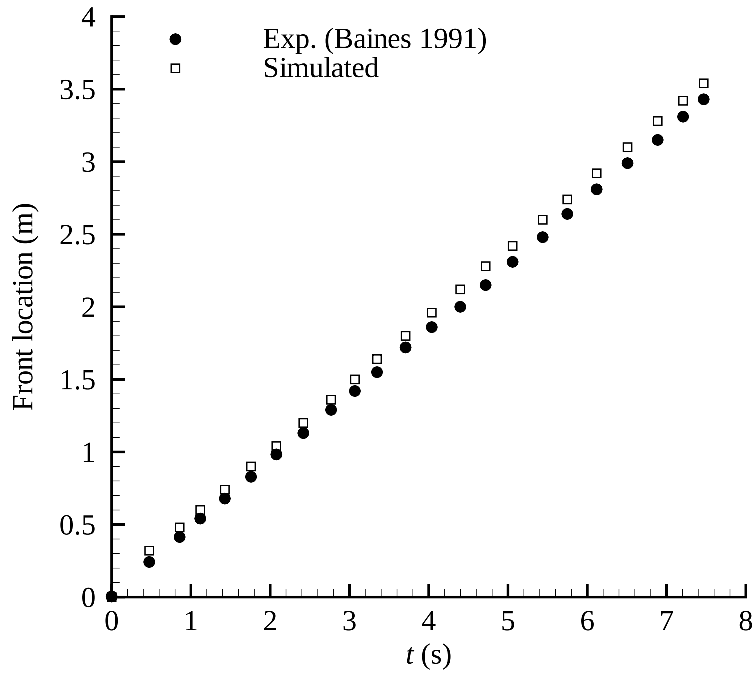

Figure 3.4: Comparison of calculated cavity front position with experiments of Baines (1991) with $\theta = 1^\circ$ and $w = 0.5\ H$.

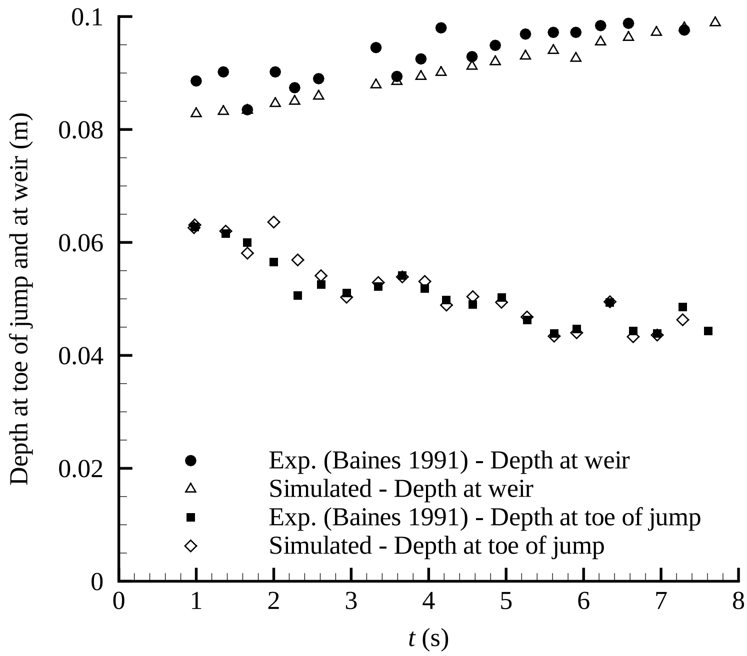

Figure 3.5: Comparison of calculated depth at the toe of jump and weir with experiments of Baines (1991) with $\theta = 1^\circ$ and $w = 0.5\ H$.

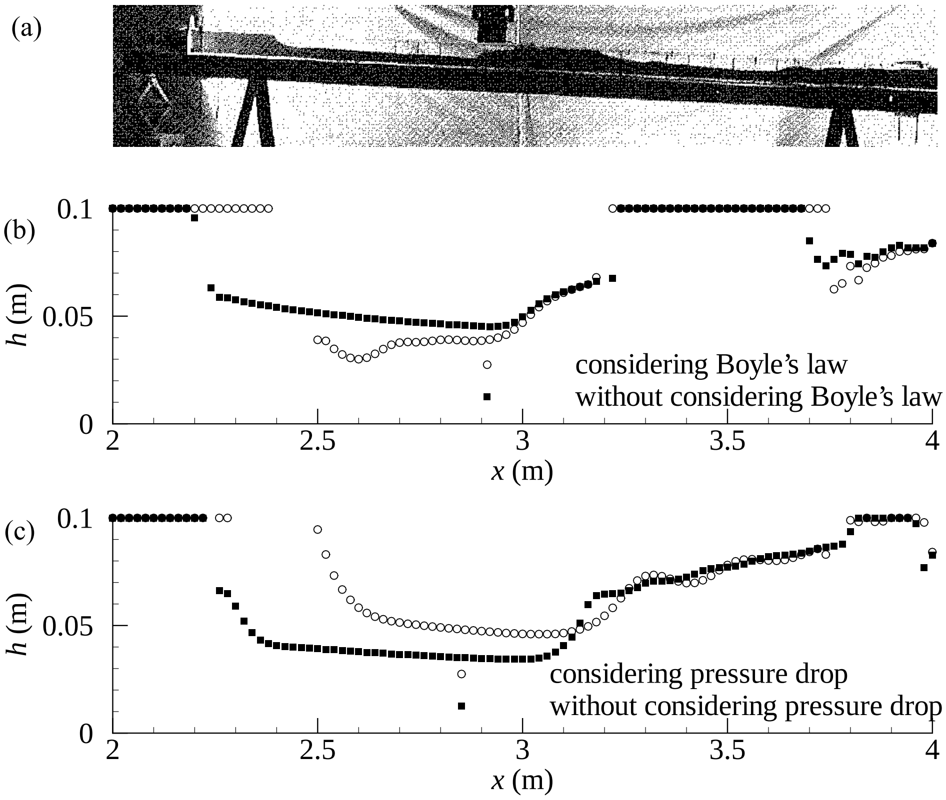

Figure 3.6: Comparison of confined air cavity water surface profile (a) confined air cavity (Baines 1991), (b) considering air pressure change and without considering it, and (c) considering pressure drop in front of entrapped air and without considering it.

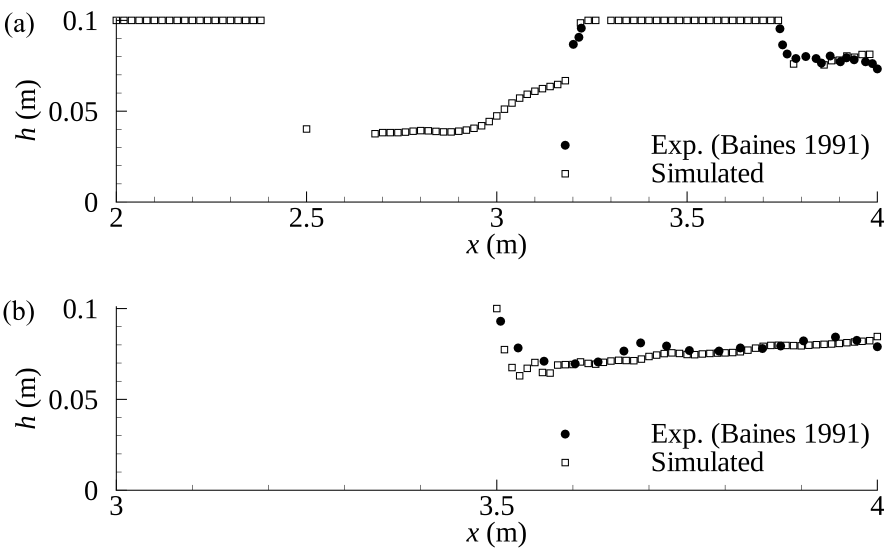

Figure 3.7: Initiation of confined air cavity ($\theta = 2°$, $w = 0.5\ H$).

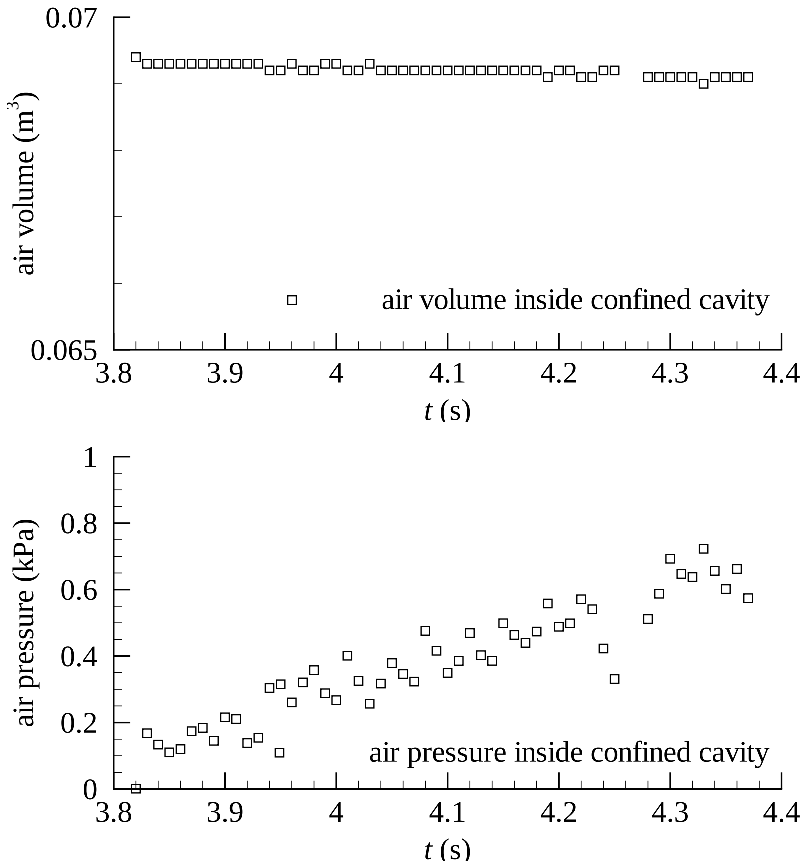

Figure 3.8: Temporal variation of air volume, and air pressure inside a confined cavity.

3.5 Summary

In this chapter, a 1D model was proposed to simulate the water surface profile inside a confined air cavity initiated in emptying inclined pipe with an installed weir at the open end. As the numerical results by Bashiri-Atrabi et al. (2015) showed, this model can be used for air cavities moving in ducts. The disadvantage of this model is that it cannot reproduce the confined cavity water surface profile properly. A solution is to use Boyle's law to take into account the temporal air pressure change inside the cavity. This model has been validated by experimental data. The numerical simulation results revealed the effect of the pressure drop and air pressure on the entrapped air cavity during the pipeline emptying. In summary, the key conclusions are:

1. Comparisons of numerical results with experimental data showed that this model can use for simulation of an entrapped cavity in a rectangular duct.
2. To simulate the confined air, it is necessary to consider the pressure drop in front of the confined air cavity, otherwise the confined air cavity vanishes rapidly.
3. While emptying duct, the confined air cavity can be modeled through Boyle's law.

3.6 References

Baines, W. D. (1991). "Air cavities as gravity currents on slope." *J. Hydraul. Eng.*, 117(12), 1600–1615.

Baines, W. D., and Wilkinson, D. L. (1986). "The motion of large air bubbles in ducts of moderate slope." *J. Hydraul. Res.*, 25(3), 313–327.

Bashiri-Atrabi, H., Hosoda, T., and Tada, A. (2015). "Simulation of air cavity advancing into a straight duct." *J. Hydraul. Eng.*, 141(1), 04014068.

Harten, A. (1983). "High resolution schemes for hyperbolic conservation laws." *J. Comp. Physics*, 49(3), 357–393.

Hirt, C. W., and Cook, J. L. (1972). "Calculating three-dimensional flows around structures and over rough terrain." *J. Comput. Physics*, 10(2), 324–340.

Hosoda, T., Inoue, K., and Tada, A. (1993). "Hydraulic transient with propagation of interface between open-channel free surface flow and pressurized pipe flow." *Proc. the 5th International Symposium on Computational Fluid Dynamics*, JSCFD, Sendai, Japan, 291–296.

Hosoda, T., Bashiri-Atrabi, H., and Tada, A. (2014). "Application of Boussinesq equation to air cavity intrusion into a water-filled conduit." *J. Japan Society of Civil Engineers*, JSCE, Ser. B1 (Hydraulic Engineering) 70(4), I_763–I_768 (in Japanese).

Liu, T., and Yang, J. (2013). "Experimental studies of air pocket movement in a pressurized spillway conduit." *J. Hydraul. Res.*, 51(3), 265–272.

Mohapatra, P. K., and Chaudhry, M. H. (2004). "Numerical solution of Boussinesq equation to simulate dam-break flows." *J. Hydraul. Eng.*, 130(2), 156–159.

Pothof, I., and Clemens, F. (2010). "On elongated air pockets in downward sloping pipes." *J. Hydraul. Res.*, 48(4), 499–503.

Pozos, O., Gonzalez, C. A., Giesecke, J., Marx, W., and Rodal, E. A. (2010). "Air entrapped in gravity pipeline systems." *J. Hydraul. Res.*, 48(3), 338–347.

Rouse, H. (1946). Elementary mechanics of fluids, John Wiley and Sons, New York.

Volkart, P. (1978). Partially filled steep pipe flow under air entrainment. Report No. 30, Institute of Hydraulic Engineering, Hydrology, and Glaciology, Technical University of Zurich, Switzerland.

Yen, B. C., and Pansic, N. (1980). "Surcharge of sewer systems." WRC Research Report No. 149, Department of Civil Engineering, University of Illinois at Urbana-Champaign.

Zhou, L., Liu, D. Y., Karney, B., and Zhang, Q. (2011a). "Influence of entrapped air pockets on hydraulic transients in water pipelines." *J. Hydraul. Eng.*, 137(12), 1686–1692.

Zhou, L., Liu, D. Y., and Ou, C. Q. (2011b). "Simulation of flow transients in a water filling pipe containing entrapped air pocket with VOF model." *Eng. Appl. Comput. Fluid Mech.*, 5(1), 127–140.

Chapter 4

Experimental and numerical analysis of air cavity intrusion in circular pipes

4.1 Introduction

During the extreme rainfall events, flow in sewer systems may change from free surface flow to pressurized flow or vice versa. Flows in pipes are called mixed flow, when some parts of flows are free surface flow, and others are pressurized flows. This transient flow between free surface and pressurized types can be observed in various systems such as hydropower plants and underground sewer networks. There are various types of flow conditions in transition flow. One of these types is depressurization, that produces a shocking surface, i.e., depressurization can produce a negative surge, that moves toward the pressurized zone (Cardle et al., 1989). Emptying a full pipe of water can cause a transient flow from pressurized-free surface flow.

The air cavity, which is discussed in this study, is due to sudden opening of one end of a filled pipe. The earlier studies of such kind of flow have been implemented by Zukoskei (1966), Cola (1967), and Benjamin (1968). Laboratory experiments conducted since the 1960s have improved the understanding of this kind of air cavity intrusion into circular pipes. These studies include those of Cola (1967), Benjamin (1968), Cardle et al. (1989), Alves et al. (1993), Hager (1999), Trajkovic et al. (1999), Vasconcelos and Wright (2008), and Bousso and Fuamba (2014).

Many numerical and experimental studies have been performed for this type of flow. Benjamin (1968) investigated the properties of gravity currents and cavity velocity in case of horizontal circular pipe. Later, Alves et al. (1993) extended Benjamin's simple approach to the horizontal and inclined circular pipes and tried to find an approximate approach for the solution of water surface profile equation. Zukoskei (1966) conducted an experimental study in circular pipes and investigated the influence of surface tension, viscosity, and pipe angle on motion of the bubbles. His experiments were carried out with various pipe diameters with different fluids. He mentioned that as the surface tension increases the propagation rate decreases. Wilkinson (1982) and Baines (1991) conducted Benjamin flow in a square cross-section duct. Wilkinson's experiments were carried out on the horizontal slope, and he investigated the variant types of flow caused by using different heights of a weir at one end. Baines (1991) showed that under the inclined slopes and using sufficient height of weir, confined air cavity generates. He also explained different types of the Benjamin flow in a square duct. Cardle et al. (1989) carried out laboratory experiments to investigate the mechanism of transition between free surface flow and pressurized flow in a circular pipe. In their study, different species of transition between pressurization and depressurization were examined. Hosoda et al. (1993) investigated the propagation of two-dimensional (2D) interfaces between open channel free surface flow and pressurized pipe flow numerically. Bashiri-Atrabi et al. (2015) proposed the hydrostatic and the Boussinesq models for rectangular ducts. In their study it was pointed out that the solitary wave equation is applicable to reproduce the air cavity water surface profile.

Several models are developed to simulate the transient flows in circular pipes. Zhou et al. (2011) employed a method of characteristics (MOC) to investigate the pressure variations associated with a filling pipeline. Fuamba (2002) also proposed the MOC model and explicitly tracked the pressurization front. Vasconcelos and Wright (2008) observed the Benjamin's cavity in their experiments and predicted the location of air-water interface with two-component pressure approach (TPA) model. Leon et al. (2010) simulated the free surface and pressurized flows using a FV model based on a two-equation model. The modified 1D Saint-Venant equations have been used for the free surface flow and the classical 1D compressible water hammer equations were used to simulate the pressurized flow. McCorquodale and Hamam (1983) and Li and McCorquodale (1999) developed a rigid water column model to simulate the mixed flow. The Preissmann model has been used for simulation of transient flow in the sewer by Cunge and Wegner (1964), Wiggert (1972), Jun (1985), Ghidaoui et al. (2005), and Leon et al. (2006). The main disadvantage of this approximation model is, its inability to simulate sub-atmospheric pressure and resulting dynamic wave phenomena in pressurized flow (Fuamba, 2002; Leon et al., 2010).

The main aims of this study are:

1. Investigation of air cavity intrusion into horizontal and inclined circular pipes and observation of various types of cavities caused by the mode of generation through experiments
2. Numerical modeling of air cavity front and water surface profile by using a hydrostatic pressure model
3. Derivation of the Boussinesq equations for circular cross section when the water depth is higher than the pipe radius
4. Modeling of air cavity water surface profile using the Boussinesq model
5. Comparing the numerical and experimental results

4.2 Description of the Experiments

4.2.1 Experimental setup

The experimental setup consisted of an acrylic pipeline laid horizontally on inclined slopes with length of L = 3 m and diameter of D = 0.05 m at the river system engineering and management laboratory at the Kyoto University (Figure 4.1). A closed pipe at one end was filled with water, and a gate was provided at another end. In all cases, the gate was opened suddenly, and some sharp-crested weirs were used with the heights of w = 0.0, 0.5 D, and 0.7 D at the entrance. The effects of weirs across the entrance were studied to define the flow regimes and the shape of the cavity. Two cameras (High-resolution Sony camera HDR-PJ760 with 29 frames/s) were used to record the shape of the air cavity. The cameras were located at L = 1 m and L = 2 m to track the air intrusion into a circular pipe.

4.2.2 Analysis of experiments

In all of the experiments, as the flow started to move through the pipe a moving cavity front was produced. The specification of flow depended on the mode of generation in downstream. Gravity currents can be classified by the mode of generation (height of weir) as shown in Figure 4.2. In the first case (a), a gate was opened suddenly and in the absence of any weir at the entrance the flow in the downstream region is almost uniform. In the second case (b), the flow of water from the pipe was impeded by a weir that was located at the open end of the pipe.

The height of the weir in this experiment was 50% of the pipe diameter. The presence of the weir caused propagation of an undular bore in the pipe. According to Wilkinson's (1982) explanation for the square duct, in the case of circular pipe, we observed three regions of the flow. The first region was seen quite near to the air cavity. In this region, the level of the air-water interface varied rapidly, but at a distance of the leading edge of the pipe, the interface reached to a uniform level. In the third region, which is behind the bore, flow was nearly uniform, and there was no wave. Finally, in the third case (c) the height of the weir was 70% of the pipe diameter. Due to the increment of the weir height, the depth of water in downstream of bore increased, and the bore front became turbulent. Therefore, three flow regimes that observed in experiments were steady, unsteady and steady dissipative regimes (Wilkinson, 1982). A schematic description of the physical model for the cavity velocity in horizontal pipes is given in Figure 4.3. Following Benjamin (1968) and moving with air cavity, continuity, momentum and Bernoulli equations can be written for a circular cross-section pipe.

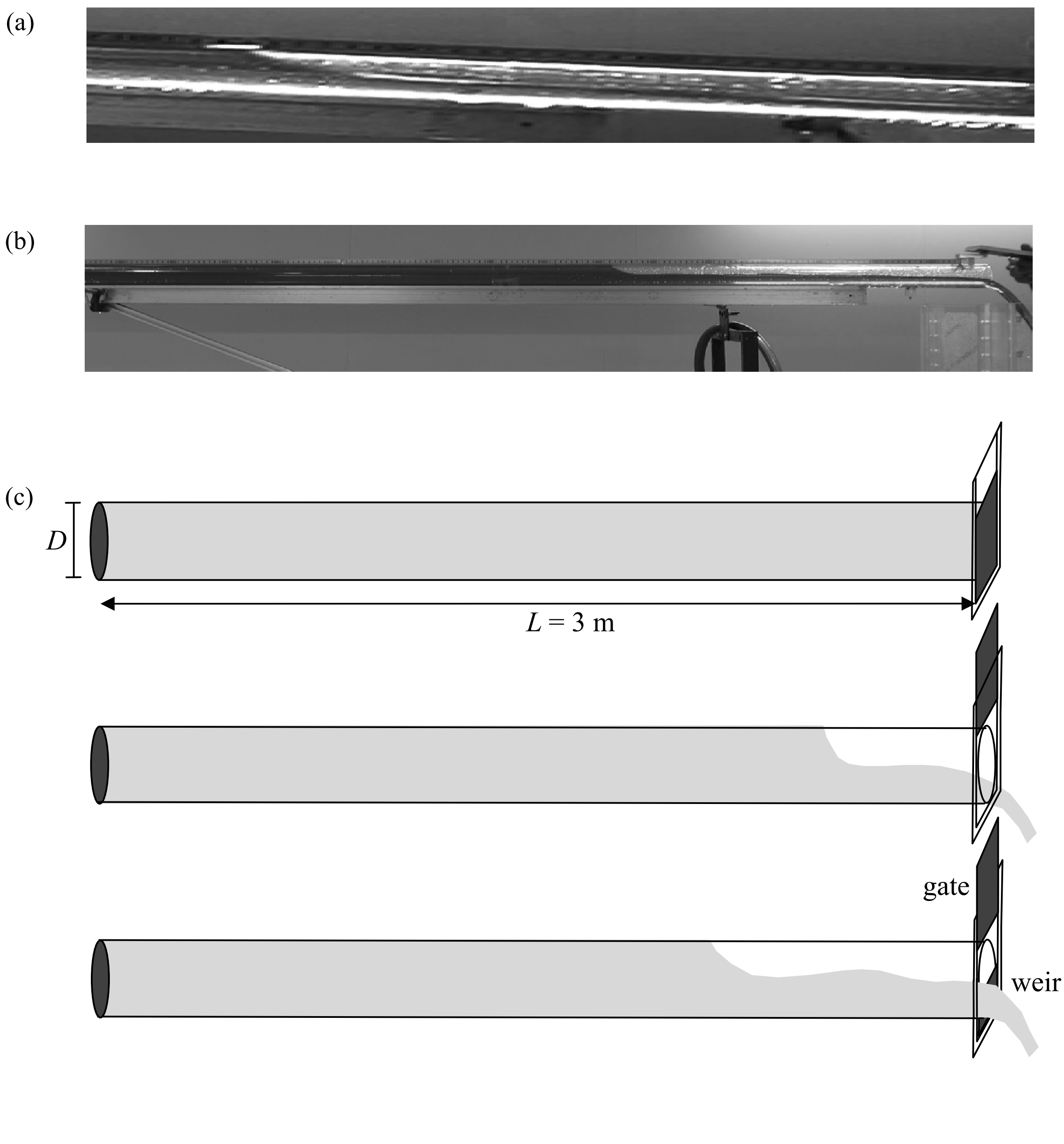

Figure 4.1: Experimental setup: (a) horizontal; (b) inclined; (c) schematic illustration of air cavity advancing into a circular pipe.

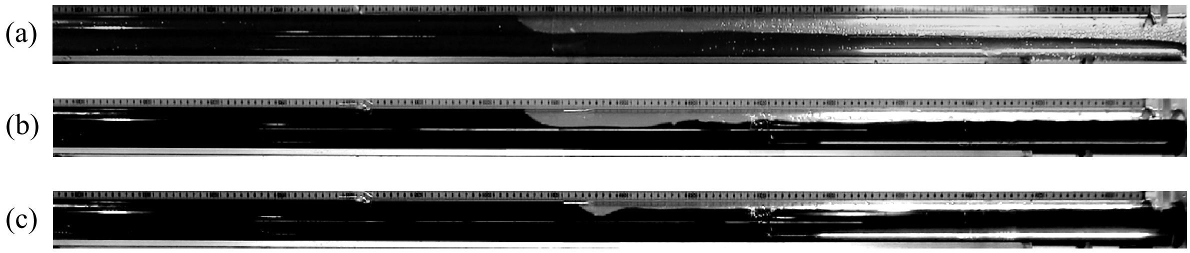

Figure 4.2: Gravity currents in a horizontal circular pipe (t = 2.866 s): (a) h_w = 0; (b) h_w = 0.5 D; (c) h_w = 0.7 D.

A frame that moves with cavity velocity in a steady flow having a free boundary that, explained for case (a), is used to predict this velocity. The continuity equation for this case is

$$A_0 u_0 = A_1 u_1 \tag{4.1}$$

where A_0 = the area of the flow in upstream; A_1 = the area of the flow in downstream; u_0 = the velocity of the cavity; and u_1 = the mean velocity relative to axes moving with the front of the cavity. It is necessary to mention that subscripts 0, 1, and 2 refer to regions of uniform flow upstream of the front, downstream of the front, and downstream region of the bore, respectively (Figure 4.3). The cross-section of the pipe is circular; with radius r and the free surface in downstream has an angle at the axis. Hence its breadth and the cross-sectional area of the flow are given by Equations (4.2) and (4.3), respectively.

$$b = 2r\sin\alpha \tag{4.2}$$

$$A_1 = \left(\pi - \alpha_1 + \frac{1}{2}\sin 2\alpha_1\right)r^2 = \pi r^2(1-\xi_1) \tag{4.3}$$

$$\xi_1 = \frac{\alpha_1 - \frac{1}{2}\sin 2\alpha_1}{\pi} \tag{4.4}$$

where b = the breadth of the flow far downstream; r = the pipe radius; α = the wetted angle; and ζ_1 = dimensionless parameter that is the function of depth of fluid at point 1.

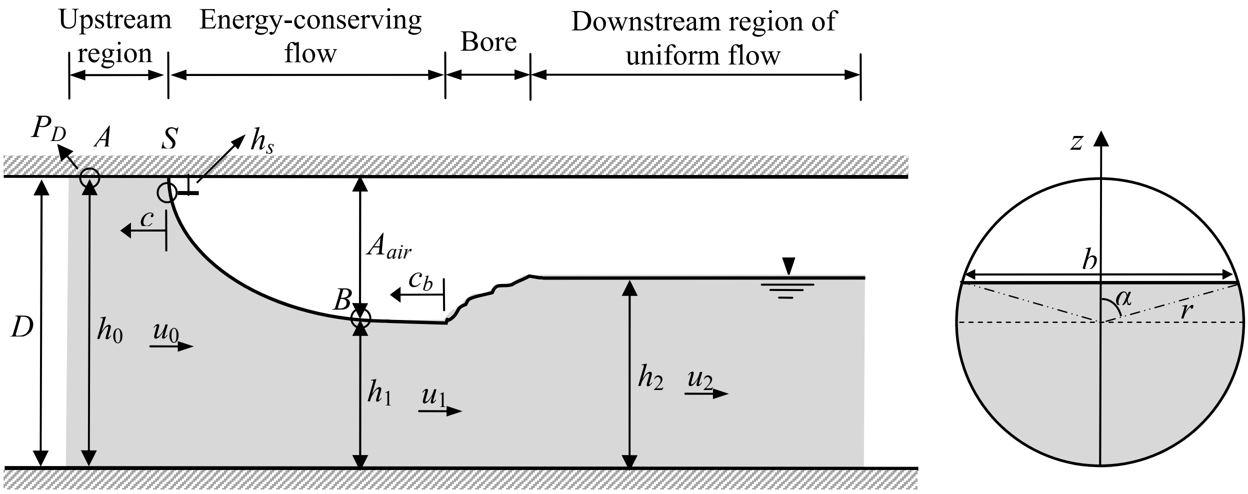

Figure 4.3: Schematic description of the Benjamin flow in a horizontal pipe.

Here, the equation of continuity takes the form

$$\frac{u_0}{u_1} = \frac{A_1}{\pi r^2} = 1 - \xi_1 \tag{4.5}$$

The Bernoulli's theorem is applied at the stagnation point S and points 0 and 1.

$$\frac{u_0^2}{2g} + \frac{P_A}{\rho g} + D = \frac{P_S}{\rho g} + D - h_S = \frac{u_1^2}{2g} + \frac{P_B}{\rho g} + h_1 \tag{4.6}$$

where g = the gravity acceleration; P_A = the pressure at the point of A; P_S = the pressure at the stagnation point S; P_B = the pressure at the point of B; D = the pipe diameter; h_S = the depth of flow at the stagnation point; and h_1 = the depth of flow at the point of B.

The surface tension increases the pressure in the air cavity so that

$$P_B = P_S + \frac{\delta}{r'} \tag{4.7}$$

where δ = the surface tension; and r' = the radius of curvature of the interface at the stagnation point. By assuming that the motion is steady, and the pressure is hydrostatic, the momentum balance between points 0 and 1 yields

$$\rho u_0^2 A_0 + P_A A_0 + \rho g \pi r^3 = \rho u_1^2 A_1 + P_B A_0 + \rho g r\left(A_1 \cos\alpha_1 + \frac{2}{3} r^2 \sin^3 \alpha_1 \right) \quad (4.8)$$

The total pressure force in downstream, where the pressure is hydrostatic, is given by

$$\int_0^{h_1} (h_1 - z) b_1 dz = r\left(A_1 \cos\alpha_1 + \frac{2}{3} r^2 \sin^3 \alpha_1 \right) \quad (4.9)$$

From Equations (4.6) and (4.7) we obtain the desired relationship

$$P_B = P_A + \frac{\rho u_0^2}{2} + \rho g h_S + \frac{\sigma}{r'} \quad (4.10)$$

After eliminate $P_B - P_A$ from Equations (4.6) and (4.8) and some reduction, two equations obtained

$$\mathsf{F}_0^2 + 2H_S + \frac{\Sigma}{2R'} = 2\mathsf{F}_0^2 + 1 - \frac{2\mathsf{F}_0^2}{(1-\xi_1)} - (1-\xi_1)\cos\alpha_1 - \frac{2}{3\pi}\sin^3\alpha_1 \quad (4.11)$$

$$2H_S + \frac{\Sigma}{2R'} = 2 - \mathsf{F}_0^2\left(\frac{1}{(1-\xi_1)^2} \right) - 2H_1 \quad (4.12)$$

The dimensionless parameters used in Equations (4.11) and (4.12) are given by

$$\mathsf{F}_0 = \frac{u_0}{\sqrt{gD}}; \quad H_1 = \frac{h_1}{D}; \quad R' = \frac{r'}{D}; \quad H_S = \frac{h_S}{D}; \quad \Sigma = \frac{4\sigma}{\rho g D^2} \quad (4.13)$$

Here F_0 = the cavity Froude number; H_1 = the depth ratio of the frontal region; R' = the normalized radius of curvature at the stagnation point; H_S = the normalized stagnation point displacement; and Σ = the surface tension parameter.

Benjamin (1968) obtained the only physically acceptable root for $\alpha_1 = 82.78^\circ$, for which $\zeta_1 = 0.42$, $H_1 = 0.563$, and $\mathsf{F}_0 = 0.542$. Note that his solution is obtained for the horizontal case and neglecting the surface tension.

Following Wilkinson (1982), in case of circular cross-section continuity and momentum equations at points 1 and 2 on either side of the bore are given by

$$A_1 u_1 = A_2 u_2 \tag{4.14}$$

$$\rho u_1^2 A_1 + \rho g r\left(A_1 \cos\alpha_1 + \frac{2}{3} r^2 \sin^3\alpha_1\right) = \rho u_2^2 A_2 + \rho g r\left(A_2 \cos\alpha_1 + \frac{2}{3} r^2 \sin^3\alpha_2\right) \tag{4.15}$$

A simpler form of Equation (4.14) can be obtained by

$$\frac{u_1}{u_2} = \frac{A_2}{A_1} = \frac{\pi - \alpha_2 + \frac{1}{2}\sin 2\alpha_2}{\pi - \alpha_1 + \frac{1}{2}\sin 2\alpha_1} = \frac{1-\xi_2}{1-\xi_1} \tag{4.16}$$

The combination of Equations (4.14) and (4.16) yields

$$\frac{u_1^2}{gh_1} = \frac{\left[(1-\xi_2)\cos\alpha_2 + \frac{2}{3\pi}\left(\sin^3\alpha_2 - \sin^3\alpha_1\right) - (1-\xi_1)\cos\alpha_1\right]}{\left[(1-\xi_1) - \frac{(1-\xi_1)^2}{(1-\xi_2)}\right]}\left(\frac{r}{h_1}\right) \tag{4.17}$$

After some simplifying, the celerity of the bore is governed by the relationship

$$\mathsf{F}_b = \sqrt{0.5}\left\{\left[(1-\xi_2)\cos\alpha_2 - (1-\xi_1)\cos\alpha_1 + \frac{2}{3\pi}\left(\sin^3\alpha_2 - \sin^3\alpha_1\right)\right] \Big/ \left((1-\xi_1) - \frac{(1-\xi_1)^2}{(1-\xi_2)}\right)\right\}^{0.5} - 0.54 \tag{4.18}$$

Similar to derivation of equations for points 1 and 2, below equation can be derived for points 0 and 2

$$\mathsf{F}_0 = \left((2-2H_2)(1-\xi_2)^2\right)^{0.5} \tag{4.19}$$

where H_2 = the depth ratio of the downstream region; and ζ_2 = the dimensionless parameter, which is a function of depth of fluid at point 2.

Experimental values of the normalized celerities of the cavity and the bore (F and F_b respectively) are plotted against the downstream depth H_1 in Figure 4.4. The curves between $0.563 < H_1 < 0.8$ correspond to Equations (4.12) and (4.18) for the cavity, and the bore respectively, with $H_S = 0$ and $\Sigma/R' = 0$. As Figure 4.4 shows, the variation of the normalized depth with normalized length in theoretical solution is in good agreement with the experimental data.

Alves et al. (1993) used an approximate approach for the solution of air cavity profile in the case of steady flow. The profile chosen in their study was an elliptical profile. In their study, they mentioned that for the horizontal case and neglecting surface tension Benjamin's original solution was obtained, i.e., $H_1 = 0.563$. Figure 4.5 shows comparison of a solution by Alves et al. (1993) with our experimental data. The water depth (h) which was normalized by the diameter of the pipe (D) is plotted against the normalized length in the horizontal case (Figure 4.5).

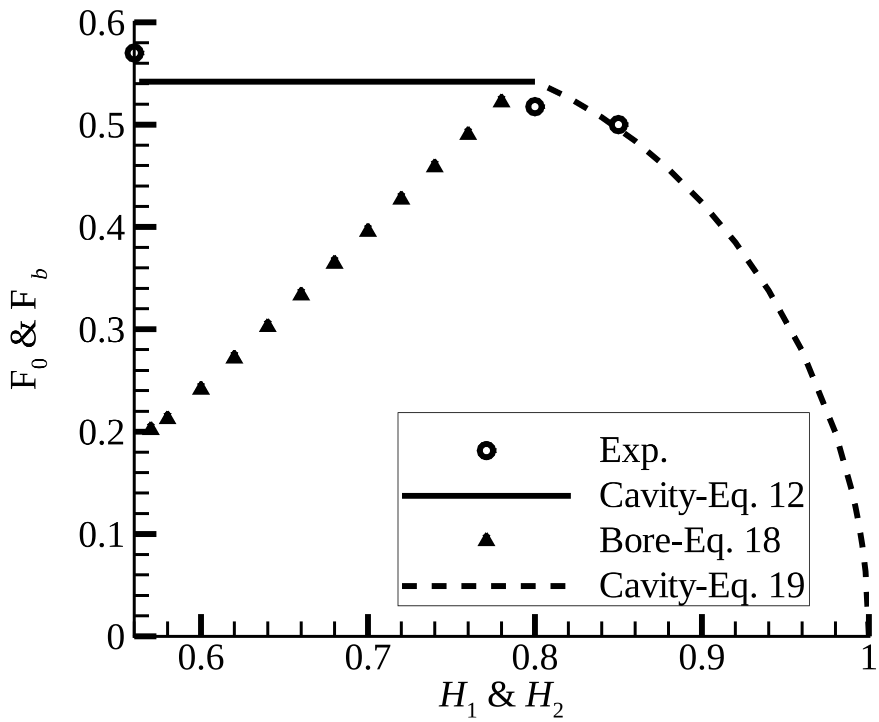

Figure 4.4: Relation between interface velocity and downstream depth.

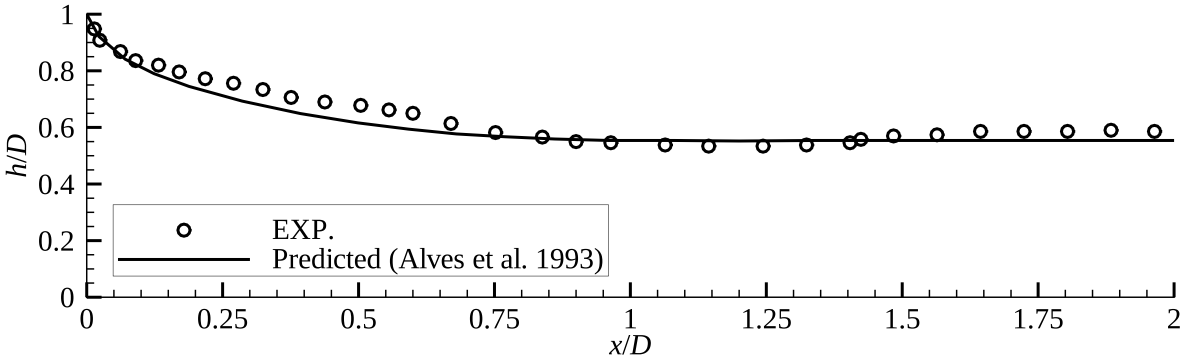

Figure 4.5: Comparison between theoretical cavity water surface profile with the experimental data in a horizontal pipe.

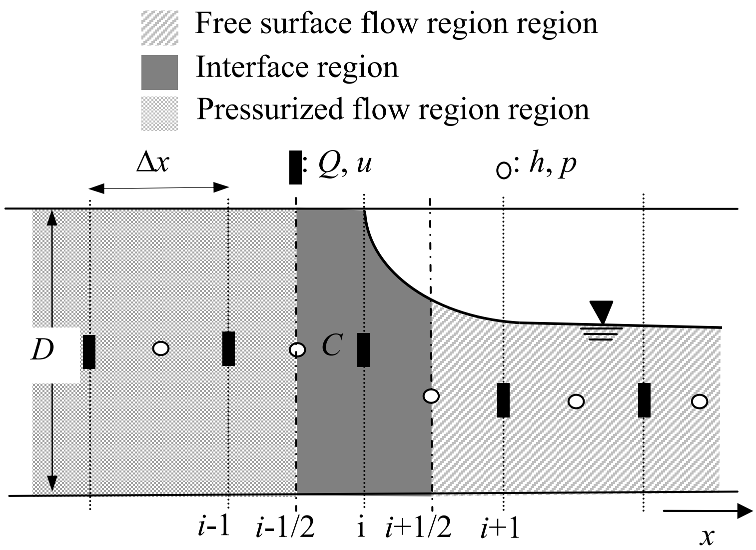

Figure 4.6: Classification of flows and staggered grid system.

4.3 Governing Equations

4.3.1 Hydrostatic model

A numerical model was developed to simulate the experimental data. The basic equations used to simulate the water surface profile were composed of one-dimensional continuity and momentum equations in the free surface and the pressurized flow, and the momentum equation of an interface between the both flows. Figure 4.6 shows the flow area that is divided into three parts: open channel flow; pressurized pipe flow; and the interface of both flows.

The fundamental equations consist of Saint-Venant equations:

- The continuity and momentum equations in free surface open channel flow

$$\frac{\partial A}{\partial t}+\frac{\partial Q}{\partial x}=0 \tag{4.20}$$

$$\frac{\partial Q}{\partial t}+\frac{\partial uQ}{\partial x}+gA\cos\theta\frac{\partial h}{\partial x}=gA\left(\sin\theta-\frac{\tau_{bx}}{\rho gR}\right)+\frac{\partial(-\overline{u'^2}A)}{\partial x} \tag{4.21}$$

Equation (4.21) indicates the momentum equations with the assumption of hydrostatic pressure.

- The continuity and momentum equations in pressurized pipe flow

$$\frac{\partial Q}{\partial x}=0 \tag{4.22}$$

$$\frac{\partial Q}{\partial t}+\frac{\partial uQ}{\partial x}+gA\frac{\partial}{\partial x}\left(\frac{P_D}{\rho g}+D\cos\theta\right)=gA\left(\sin\theta-\frac{\tau_{bx}}{\rho gR}\right)+\frac{\partial(-\overline{u'^2}A)}{\partial x} \tag{4.23}$$

where A = the cross-sectional area; t = the time; Q = the discharge; x = the spatial coordinate; u = the depth-averaged velocity; θ = the bottom slope of the pipe; h = the flow depth; τ_{bx} = the wall shear stress vector; ρ = the mass density of fluid; R = the hydraulic radius; $\overline{u'^2}$ = the turbulence intensity; P_D = the pressure at the top of the pipe; and D = the pipe diameter.

The wall shear stress is evaluated by Manning's formula as follows:

$$\frac{\tau_{bx}}{\rho}=\frac{gn^2u|u|}{h^{1/3}} \tag{4.24}$$

In this study, Manning roughness coefficient n = 0.01 $\mathrm{m}^{-1/3}\mathrm{s}$. The momentum equation at the interface C in Figure 4.6 is derived as Equation (4.25) by the integrating of Equations (4.21) and (4.23) from $x_{i-1/2}$ to $x_{i+1/2}$.

$$\frac{\partial Q}{\partial t}\Delta x+(uQ)_{x_{i+1/2}}-(uQ)_{x_{i-1/2}}+gA_{x_i}\left\{h_{i+1/2}-\left(\frac{P_D}{\rho g}+D\right)_{i-1/2}\right\}=$$
$$gA_{x_i}\Delta x\left(\sin\theta-\frac{\tau_{bx}}{\rho gR}\right)_{x_i}+\left(-\overline{u'^2}A\right)_{x_{i+1/2}}-\left(-\overline{u'^2}A\right)_{x_{i-1/2}} \tag{4.25}$$

The eddy diffusivity term is evaluated by an empirical formula with the depth-averaged zero equation model that is proposed by Hosoda et al. (1993)

$$\frac{\partial\left(-\overline{u'^2}A\right)}{\partial x}=\frac{\partial}{\partial x}\left(AD_h\frac{\partial u}{\partial x}\right);\quad D_h=\beta h|u|;\quad \beta=0.05 \tag{4.26}$$

where D_h = the eddy viscosity; and β = constant coefficient of eddy viscosity that is defined by comparison of observation data and theoretical formula (= 0.05).

4.3.2 Boussinesq model

Since the shallow water equations (SWE) cannot predict the water surface undulations, because of hydrostatic assumption, the Boussinesq equation is derived to consider the vertical acceleration effects on the water surface in the circular cross-section pipes. The earliest depth-averaged model that included weakly dispersive effects was derived by Boussinesq (1871). Lin (2008) explained different types of Boussinesq equations and their applications in details. Derivation of Boussinesq equation for the unsteady flows in an open channel with a circular cross-section, when the depth is lower than the radius, is described by Hosoda et al. (1997). To reproduce the undular bore in free surface flow inside a circular pipe, the depth-averaged SWE is derived with the effect of vertical acceleration for the case that the water depth is higher than the radius. The derivation of Boussinesq equation was carried out under the assumption of non-uniform depth in a transverse direction. Referring to the Cartesian coordinate system and the definition of symbols as shown in Figure 4.7, the derivation procedure is as follow:

The depth-averaged continuity equation is expressed by

$$\begin{cases} \dfrac{\partial h}{\partial t} + \dfrac{\partial hu}{\partial x} + \dfrac{\partial hv}{\partial y} = 0 & \text{if} \quad 0 \le y \le l \\ \dfrac{\partial hu}{\partial x} + \dfrac{\partial hv}{\partial y} = 0 & \text{if} \quad l \le y \le r \end{cases} \tag{4.27}$$

where h = local depth; u = velocity in x-direction; and v = velocity in y-direction.

Assuming the uniformity of velocity distribution in the z-direction, the velocity in y-direction can be obtained by integrating of the continuity equation from 0 to y.

$$\begin{cases} v = -\dfrac{1}{h}\left(\displaystyle\int_0^y \dfrac{\partial h}{\partial t} dy + \int_0^y \dfrac{\partial hu}{\partial x} dy \right) & \text{if} \quad y < l \\ v = -\dfrac{1}{h}\left(\displaystyle\int_0^l \dfrac{\partial h}{\partial t} dy + \int_0^y \dfrac{\partial hu}{\partial x} dy \right) & \text{if} \quad y \ge l \end{cases} \tag{4.28}$$

Substituting Equation (4.28) into the continuity equation and integrating from z to z_s in the z-direction, and after some manipulations with the Leibnize rule, the velocity in the z-direction (w) can be obtained by Equation (4.29).

$$\begin{cases} w = -\dfrac{z - z_b}{h}\left(\dfrac{\partial h}{\partial t} + u \dfrac{\partial h}{\partial x} \right) + \dfrac{z_s - z}{h^2} \dfrac{\partial h}{\partial y} \left(\displaystyle\int_0^y \dfrac{\partial h}{\partial t} dy + \int_0^y \dfrac{\partial hu}{\partial x} dy \right) & \text{if} \quad y < l \\ w = \dfrac{z - z_u}{h} u \dfrac{\partial h}{\partial x} + \left(\dfrac{z_b - z}{h^2} \dfrac{\partial z_u}{\partial y} - \dfrac{z_u - z}{h^2} \dfrac{\partial z_b}{\partial y} \right) \left\{ \displaystyle\int_0^l \dfrac{\partial h}{\partial t} dy + \int_0^y \dfrac{\partial hu}{\partial x} dy \right\} & \text{if} \quad y \ge l \end{cases} \tag{4.29}$$

Substituting Equation (4.29) into the equation of motion in the z-direction, Equation (4.30), and integrating from z to z_s in z-direction and neglecting some terms, the pressure distribution with consideration of vertical acceleration can be expressed by

$$\frac{\partial w}{\partial t} + u \frac{\partial w}{\partial x} + v \frac{\partial w}{\partial y} + w \frac{\partial w}{\partial z} = g \cos\theta - \frac{1}{\rho} \frac{\partial p}{\partial z} \tag{4.30}$$

$$\begin{cases} \dfrac{p}{\rho} = g(z_s - z)\cos\theta + \left[\left\{ -\dfrac{(z_s - z)(h + z - z_b)}{2h^2} \dfrac{\partial z_u}{\partial y} - \dfrac{(z_s - z)^2}{2h^2} \dfrac{\partial z_b}{\partial y} \right\}\Bigg|_{y=l} + \displaystyle\int_l^y \dfrac{1}{h} dy \right] \dfrac{\partial^2 z_s}{\partial t^2} l & y \ge l \\ \dfrac{p}{\rho} = g(z_s - z)\cos\theta + \left\{ \dfrac{h^2 - (z - z_b)^2}{2h} - \dfrac{(z_s - z)^2}{2h^2} \dfrac{\partial z_b}{\partial y} y \right\} \dfrac{\partial^2 z_s}{\partial t^2} & y < l \end{cases}$$

(4.31)

The cross-sectional integrals of pressure for $h < r$ and $h > r$ are calculated by integrating of Equations (4.31(a)) and (4.31(b)) over a circular cross-section as follow, respectively

$$\int_A \frac{p}{\rho} dA = \int_{-b}^{b}\int_{z_b}^{z_s} \frac{p}{\rho} dzdy = -gh_G A\cos\theta$$
$$+\frac{1}{3}(2z_s^2 b - 2z_s f_1 + f_2)\times F_1 - \frac{1}{12}(2z_s^2 b - 2z_s f_1 + f_2)\times F_2 \tag{4.32a}$$

$$\int_A \frac{p}{\rho} dA = gh_G A\cos\theta + \left[\frac{1}{3}(2z_s{}^2 l - 2z_s f_1 + f_2) + \frac{1}{12}(2z_{bl}{}^2 l - 4z_s z_{bl} l + 2z_s f_1 - f_2)\right]\frac{\partial^2 z_s}{\partial t^2}$$
$$+\left[\frac{1}{h_l{}^2}\frac{\partial z_u}{\partial y}\bigg|_{y=l}\left\{\frac{1}{3}Q_3 - z_{bl}Q_2 - z_s(h_l - z_{bl})Q_1 + P_3 + P_2 - 2z_{bl}P_1\right\}\right.$$
$$\left.+\frac{1}{h_l^2}\frac{\partial z_b}{\partial y}\bigg|_{y=l}\left\{-\frac{1}{3}Q_3 + z_s Q_2 - z_s{}^2 Q_1 - P_3 - P_2 + 2z_s P_1\right\} + 2\int_l^R Q(y)hdy\right]\frac{\partial^2 z_s}{\partial t^2} l$$
(4.32b)

Since $\frac{\partial^2 z_s}{\partial t^2}$, which is main effective term for rapidly varied unsteady flows, is included just in F_1 and F_2 in Equation (4.32a), we considered only these terms in Equation (4.32a) by following equations:

$$F_1 = \frac{\partial^2 z_s}{\partial t^2} + 2u\frac{\partial^2 z_s}{\partial t \partial x} + u^2\frac{\partial^2 z_s}{\partial x^2} + \frac{\partial u}{\partial t}\frac{\partial z_s}{\partial x} + u\frac{\partial u}{\partial x}\frac{\partial z_s}{\partial x} \tag{4.33}$$

$$F_2 = \frac{\partial^2 z_s}{\partial t^2} + \frac{\partial^2 z_s u}{\partial t \partial x} + u\frac{\partial^2 z_s}{\partial t \partial x} + u\frac{\partial^2 z_s u}{\partial x} - \frac{\partial u}{\partial x}\frac{\partial z_s}{\partial t} - \frac{\partial u}{\partial x}\frac{\partial z_s u}{\partial x} \tag{4.34}$$

For simplicity, only the $\frac{\partial^2 z_s}{\partial t^2}$ is considered to evaluate F_1 and F_2 using the following equation.

$$F_1 = F_2 = \frac{\partial^2 z_s}{\partial t^2} = -\frac{\partial}{\partial t}\left(\frac{1}{2b}\frac{\partial Q}{\partial x}\right) \tag{4.35}$$

Q_3, Q_2, Q_1, $\int_l^R Q(y)hdy$, P_3, P_2, and P_1 are following as:

$$Q_3 = \int_l^R h^3 dy = \int_\phi^{\pi/2}(2R\cos\theta)^3 R\cos\theta d\theta = \frac{R^4}{4}(6\pi - \sin 4\phi - 8\sin 2\phi - 12\phi) \tag{4.36}$$

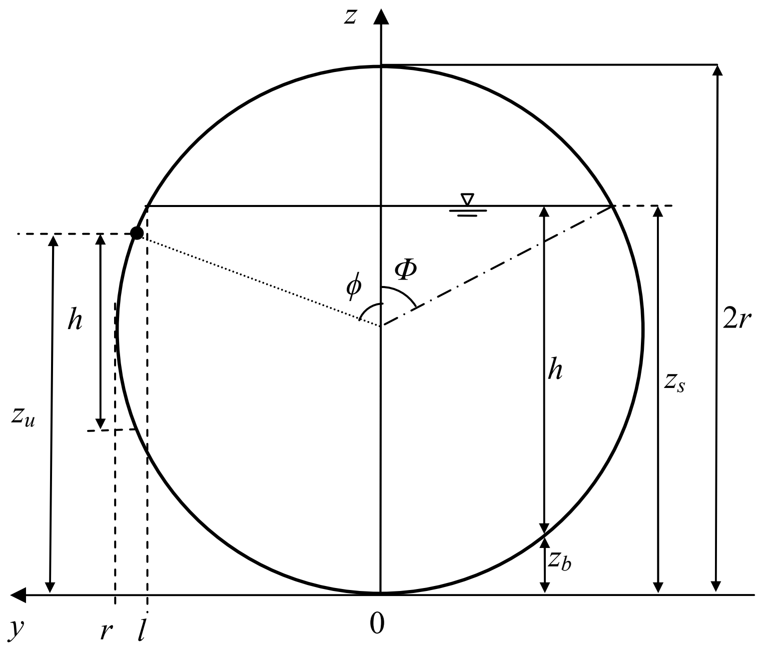

Figure 4.7: Variables definition for Boussinesq equation ($h > r$).

$$Q_2 = \int_l^R h^2 dy = 4R^3 \int_\phi^{\pi/2} \cos^3 \theta d\theta = \frac{R^3}{3}(8 - \sin 3\phi - 9\sin\phi) \tag{4.37}$$

$$Q_1 = \int_l^R h dy = 2R^2 \int_l^R \cos^2 \theta d\theta = \frac{R^2}{2}(\pi - \sin 2\phi - 2\phi) \tag{4.38}$$

$$\int_l^R Q(y) h dy = \int_\phi^{\pi/2} \frac{1}{4}(\pi - 2\phi) 2R\cos\theta . R\cos\theta d\theta = \frac{R^2}{8}(\pi - 2\phi)^2 - \frac{R^2}{8}(\pi - 2\phi)\sin 2\phi \tag{4.39}$$

$$\begin{aligned} P_3 &= \int_l^R z_b h^3 dy = \int_\phi^{\pi/2} R(1-\cos\theta)(2R\cos\theta)^2 R\cos\theta d\theta \\ &= \frac{R^4}{24}(64 - 18\pi + 36\phi + 3\sin 4\phi - 8\sin 3\phi + 24\sin 2\phi - 72\sin\phi) \end{aligned} \tag{4.40}$$

$$\begin{aligned} P_2 &= \int_l^R {z_b}^2 h dy = \int_\phi^{\pi/2} \left\{R(1-\cos\theta)\right\}^2 .2R\cos\theta . R\cos\theta d\theta \\ &= \frac{R^4}{48}(-128 + 42\pi - 84\phi - 34\sin 4\phi + 16\sin 3\phi - 48\sin 2\phi + 144\sin\phi) \end{aligned} \tag{4.41}$$

$$P_1 = \int_l^R z_b h dy = \int_\phi^{\pi/2} R(1-\cos\theta).2R\cos\theta.R\cos\theta d\theta$$
$$= \frac{R^3}{6}(3\pi - 6\phi - 8 + \sin 3\phi - 3\sin 2\phi + 9\sin\phi) \tag{4.42}$$

We can add the cross-sectional integrals of pressure, Equations (4.32a) and (4.32b), into the left hand side of 1D momentum equation of open channel flow, Equation (4.21), given by Equation (4.43).

$$\frac{\partial Q}{\partial t} + \frac{\partial uQ}{\partial x} + gA\cos\theta\frac{\partial h}{\partial x} + \frac{\partial}{\partial x}\int_A \frac{p}{\rho}dA = gA\left(\sin\theta - \frac{\tau_{bx}}{\rho gR}\right) + \frac{\partial(-\overline{u'^2}A)}{\partial x} \tag{4.43}$$

Other parts of simulation procedure are same as the hydrostatic model.

4.4 Numerical Method

The method of flood invasion analysis in flood plains was used for the discretisation and the time integral of Equations (4.20) and (4.21) in the free surface region (Iwasa and Inoue, 1982). The finite difference representation of flood flow equations using the staggered difference scheme are (Figure 4.7):

Continuity equation

$$\frac{A_{i+1/2}^{n+1} - A_{i+1/2}^{n}}{\Delta t} + \frac{Q_{i+1}^{n} - Q_{i}^{n}}{\Delta x} = 0 \tag{4.44}$$

Momentum equation

$$\frac{Q_i^{n+1} - Q_i^n}{\Delta t} + \frac{u_{i+1/2}^n Q_{i+a}^n - u_{i-1/2}^n Q_{i-1+b}^n}{\Delta x} + gA_i^n\frac{h_{i+1/2}^n - h_{i-1/2}^n}{\Delta x} = -\left(gA\frac{\tau_{bx}}{\rho gR}\right)_i^n \tag{4.45}$$

in which

$$a = \begin{cases} 1 & \text{if} \quad u_{i+1/2}^n \le 0 \\ 0 & \text{if} \quad u_{i+1/2}^n > 0 \end{cases}; \quad b = \begin{cases} 1 & \text{if} \quad u_{i-1/2}^n \le 0 \\ 0 & \text{if} \quad u_{i-1/2}^n > 0 \end{cases}; \quad u_{i+1/2}^n = \frac{u_{i+1}^n + u_i^n}{2} \tag{4.46}$$

where superscripts n and n+1 denote current and next time step, respectively.

4.4.1 HSMAC method

The highly simplified mark-and-cell (HSMAC) method was adopted for the pressurized region to calculate the velocity and pressure simultaneously with an iterative procedure (Hirt and Cook, 1972). In the pressurized region calculation with the HSMAC method, pressure and velocity are updated, and the divergence of total mass will vanish. In each cell (i) the value of velocity divergence D' is calculated by

$$D = (1/\mathrm{d}x)(u_{i+1} - u_i) \tag{4.47}$$

If the value of D' is less than some small value of ε, it is not necessary to change the cell velocity; otherwise the pressure at the staggered position is changed to

$$p_D^* = P_D^n + \delta p^* \tag{4.48}$$

$$\delta p^* = -\beta D', \quad \beta = \beta_0 / 2\Delta t(1/\Delta x^2) \tag{4.49}$$

where β_0 = the relaxation factor that should be $\beta_0 < 2$ for iteration stability. In general, the best value of β_0 for better convergence can be determined by experimentation. This procedure should be repeated until $D' < \varepsilon$ and when the iteration has converged we can calculate the new velocity by continuity equation, and this completes the calculations for one time step.

4.4.2 Harten and QUICK TVD

The finite volume method with the Harten TVD (Harten, 1983) and quadratic upstream interpolation for convective kinematics (QUICK) (Leonard, 1979) schemes for the convective inertia term were used as the numerical method. The convective term was advanced using the forward Euler method and second-order Adams-Bashforth scheme (Roache, 1972). Harten (1983) considered a 3-point first order accurate Lax-Wendorff scheme in conservation form with a numerical flux of the form

$$f_{i+1/2} = \frac{1}{2}[f_i + f_{i+1}] + \frac{\Delta x}{2\Delta t}[g_i + g_{i+1} - G(\upsilon_{i+1} + \upsilon_{i+1/2})\alpha_{i+1/2}] \tag{4.50}$$

To satisfy the Equation (4.50), Equations (4.51)-(4.58) are defined by

$$f_i = (Q \cdot u)_i \tag{4.51}$$

$$\alpha_{i+1/2} = Q_{i+1} - Q_i \tag{4.52}$$

$$\begin{cases} \upsilon_{i+1/2} = \dfrac{\Delta t}{\Delta x} \cdot \dfrac{f_{i+1} - f_i}{Q_{i+1} - Q_i} & \text{if} \quad (Q_{i+1} - Q_i \neq 0) \\ \upsilon_{i+1/2} = \dfrac{\Delta t}{\Delta x} \cdot u_i & \text{if} \quad (Q_{i+1} - Q_i = 0) \end{cases} \tag{4.53}$$

$$\begin{cases} \gamma_{i+1/2} = \dfrac{g_{i+1} - g_i}{\alpha_{i+1/2}} & \text{if} \quad (\alpha_{i+1/2} \neq 0) \\ \gamma_{i+1/2} = 0 & \text{if} \quad (\alpha_{i+1/2} = 0) \end{cases} \tag{4.54}$$

Using the notation

$$g_i = S \cdot \max\left[0, \min(\left|\bar{g}_{i+1/2}\right|, S \cdot \bar{g}_{i-1/2})\right] \tag{4.55}$$

where

$$\bar{g}_{i+1/2} = \frac{1}{2}\left[G(\upsilon_{i+1/2}) - (\upsilon_{i+1/2})^2\right]\alpha_{i+1/2} \tag{4.56}$$

$$S = \operatorname{sgn}(\bar{g}_{i+1/2}) \tag{4.57}$$

where $G(x)$ is some function of Equation (4.58), which is referred to as the coefficient of numerical viscosity.

$$\begin{cases} G(x) = \dfrac{x^2}{4\varepsilon} + \varepsilon & \text{if} \quad |x| \leq 2\varepsilon \\ G(x) = |x| & \text{if} \quad |x| > 2\varepsilon \quad (\varepsilon = 0.1) \end{cases} \tag{4.58}$$

4.4.3 Pressure drop at stagnation point

The pressure at the stagnation point, which is shown in Figure 4.3, can be evaluated by following equations (Wilkinson, 1982; Atrabi et al., 2015)

$$\frac{P_s}{\rho g} = D - \frac{c^2}{2g} \tag{4.59}$$

$$c = \kappa \frac{Q_0 - Q_1}{A_a}; \qquad (\kappa = 2 - 3) \tag{4.60}$$

where c = the cavity celerity; A_a = the air area above the water; and κ = a coefficient that is related to pipe diameter and flow properties.

4.4.4 Stability

The explicit or forward Euler Method with first order accuracy, in which all fluxes and sources are evaluated using known values at t_n was used for the time integration as follow (Ferziger and Peric, 1999)

$$\int_{t_n}^{t_{n+1}} \frac{df}{dt} \mathrm{d}t = \phi^{n+1} - \phi^n = \int_{t_n}^{t_{n+1}} f(t, \phi(t)) dt \tag{4.61}$$

$$\phi^{n+1} = \phi^n + f(t_n, \phi^n) \Delta t \tag{4.62}$$

The advantages of explicit methods are: usually easy to program and use little computer memory. The famous dimensionless parameter that is called Courant number, Equation (4.63), is considered to satisfy the stability of the scheme.

$$C_n = \frac{u \Delta t}{\Delta x} < 1 \qquad \text{or} \qquad \Delta t < \frac{\Delta x}{u} \tag{4.63}$$

It is important to choose the time step and grid size sufficiently small to satisfy the stability.

4.5 Evaluation of Model

In this section, the efficiency of the model is tested using experimental conditions that were explained earlier. To evaluate the model we considered two series of experiments:

first, experiments without weir at the downstream opening end (horizontal and inclined); and another series of experiments with a weir at the end (horizontal). The observed and calculated water surface profiles of both cases are compared with hydrostatic pressure and Boussinesq models in this section.

4.5.1 Free overfall (no weir)

The initial and boundary conditions for the simulation of this kind of cavity advancing are same as experimental conditions that were explained in the previous section. The horizontal or inclined pipe was full of water initially and after removing the downstream gate the air interred to the pipe and cavity generated. The computations are performed using n = 0.01 $m^{-1/3}s$, Δt = 0.0005 s, and Δx = 0.01 m.

We considered two conditions to simulate the flow at the downstream boundary: zero gradient; and critical condition. In zero gradient model the flux at the downstream was supposed to be equal to the flux at one cell before that. Also, for critical condition model we used the critical discharge as follows (Jain, 2001)

$$\frac{\alpha Q_c^2}{g\cos\theta} = \frac{A_c^3}{B_c} \tag{4.64}$$

where c denotes the critical; B = the surface width; α = 1; and cos θ = 1 for horizontal case.

To evaluate the numerical schemes we have compared Harten TVD with a second-order Adams-Bashforth scheme and the forward Euler method, and QUICK with a second-order Adams-Bashforth scheme and the forward Euler method. As Figure 4.8 showed Harten TVD with forward Euler method was more suitable for simulation the experimental data.

Figure 4.9 shows that a critical condition can reproduce better results for downstream depth compare to the zero gradient condition in the case without weir. Also, water surface profile near the cavity front can be simulated well using the Boussinesq model. The results showed that the only difference between the critical condition and zero gradient condition is the downstream depth, and the front positions are similar in both models. Figure 4.10 shows the temporal variation of a front position of the air cavity that were simulated by hydrostatic and Bossinesq models.

According to Figure 4.10, in the case of $h_w = 0$, the Boussinesq front positions are in better agreement with the experimental observations. Also, Figure 4.11 shows the simulation results for air cavity advancing into an inclined pipe. Based on the results, for inclined pipe also the Boussinesq model can reproduce the better water surface profile. Evaluation of the model for conserving the mass is shown in Figure 4.12 (h_w = 0.0, $\theta = 0.0$).

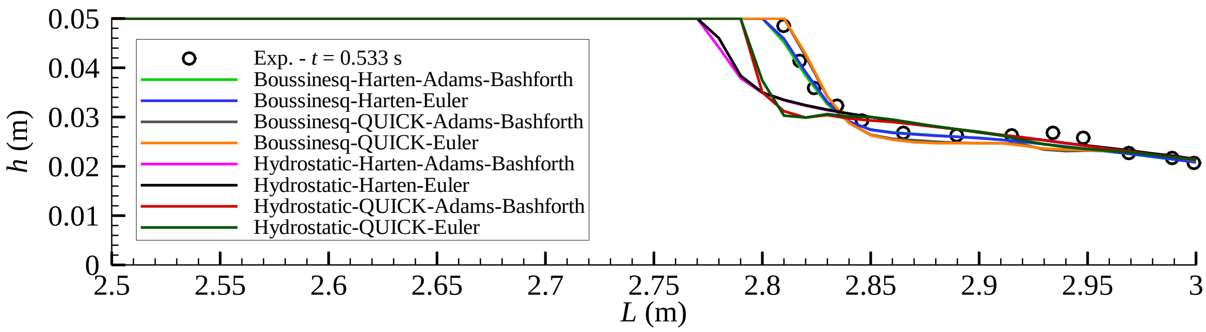

Figure 4.8: Comparison between hydrostatic, Boussinesq, Harten, QUICK, Euler, and Adams-Bashforth models ($h_w = 0.0$, $\theta = 0$˚).

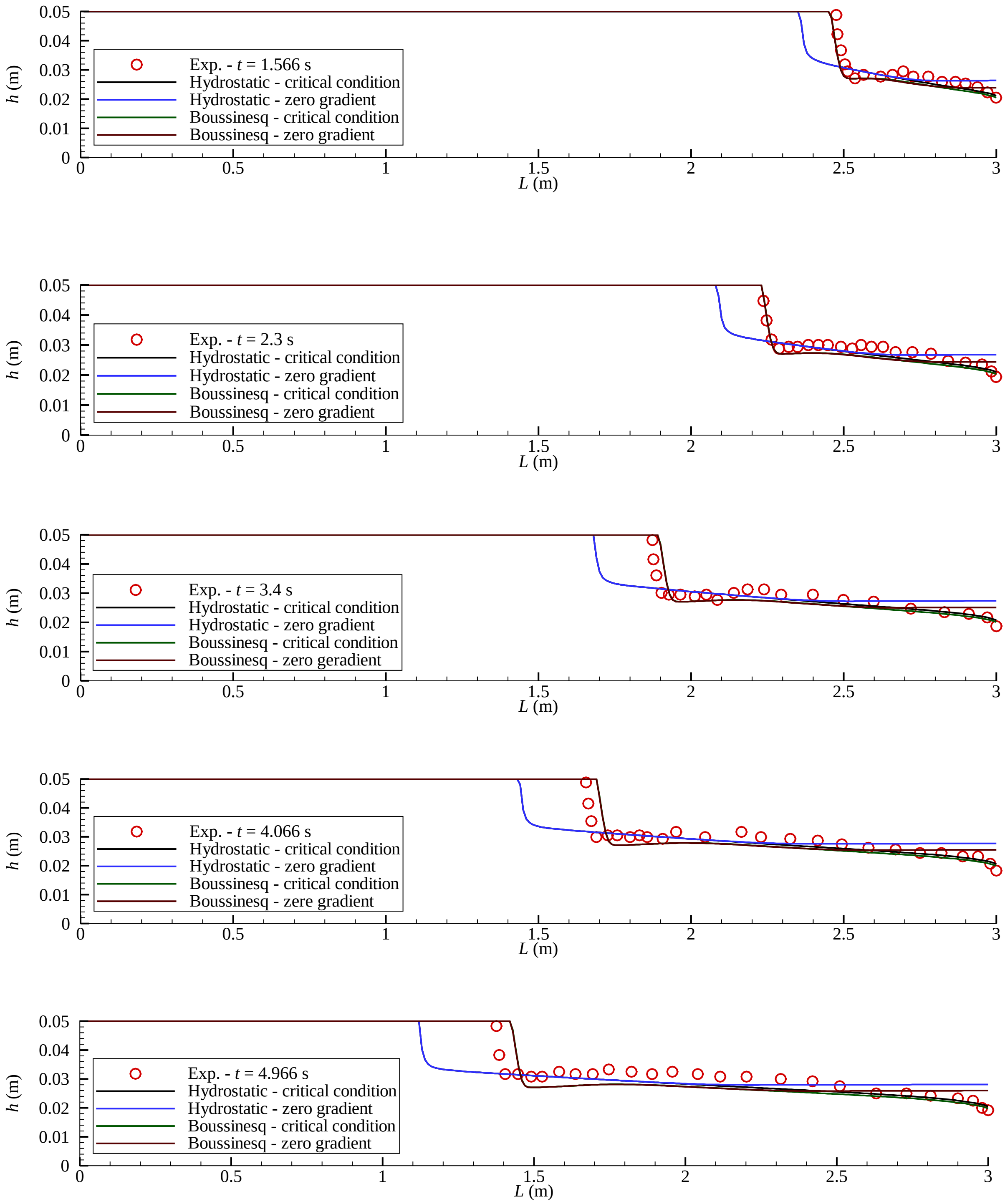

Figure 4.9: Simulation of cavity surface profile and end depth using hydrostatic and Boussinesq models ($h_w = 0.0$, $\theta = 0^{\circ}$).

4.5.2 Controlled buoyancy flux

In this case, a weir is located at the downstream end and when the gate is opened a controlled buoyancy flux is fed into the pipe. The aim of using the weir was generating the undular bore in the circular pipe and for this purpose we used two different height of weir ($h_w = 0.5\ D$ and $h_w = 0.7\ D$). We used the weir equation for calculation of discharge after weir by following equation (Fuamba, 2002)

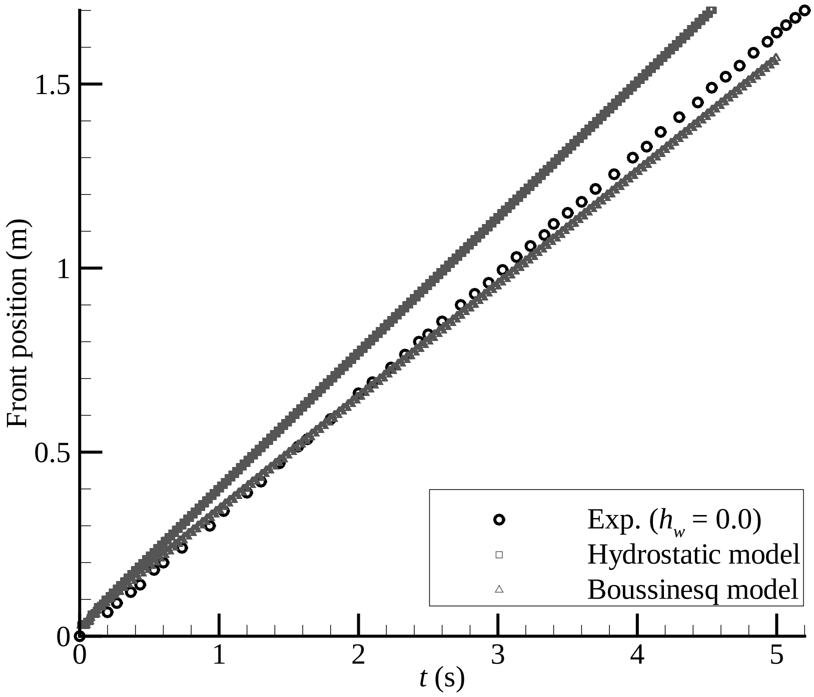

Figure 4.10: Temporal variation of air cavity front position ($h_w = 0.0$, $\theta = 0^{\circ}$).

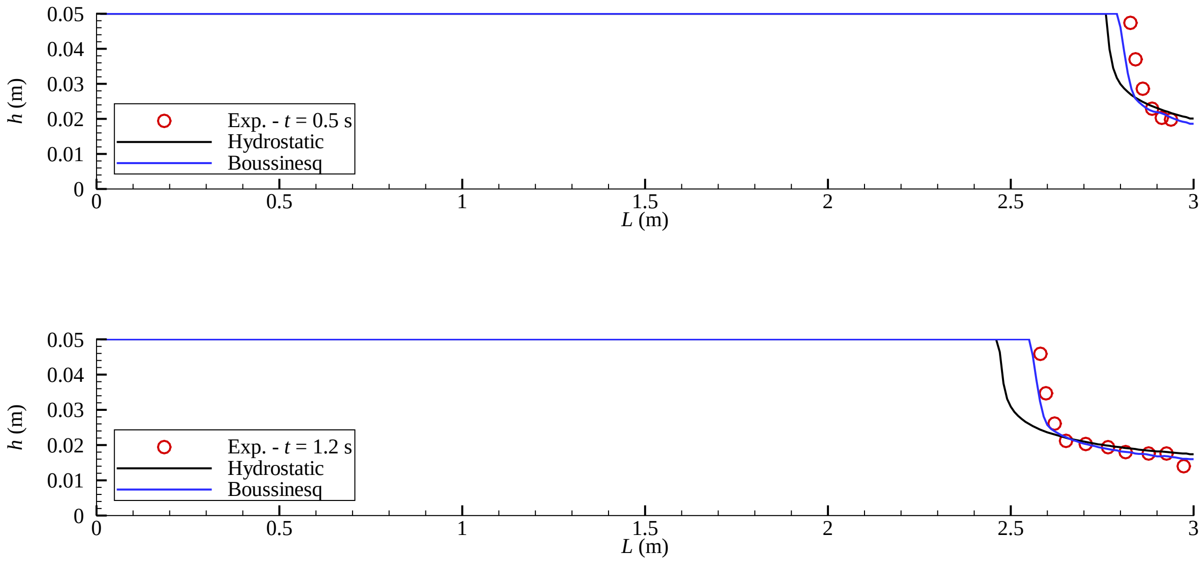

Figure 4.11: Simulation of air cavity advancing in an inclined pipe (h_w = 0.0, θ = 8˚).

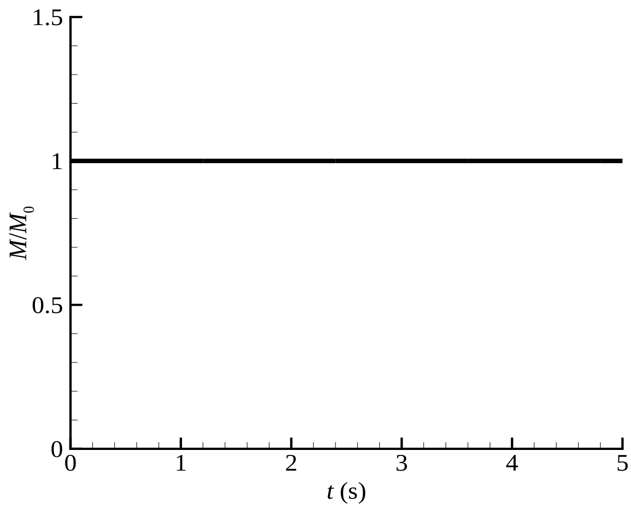

Figure 4.12: Mass traces of numerical model (h_w = 0.0, θ = 0˚).

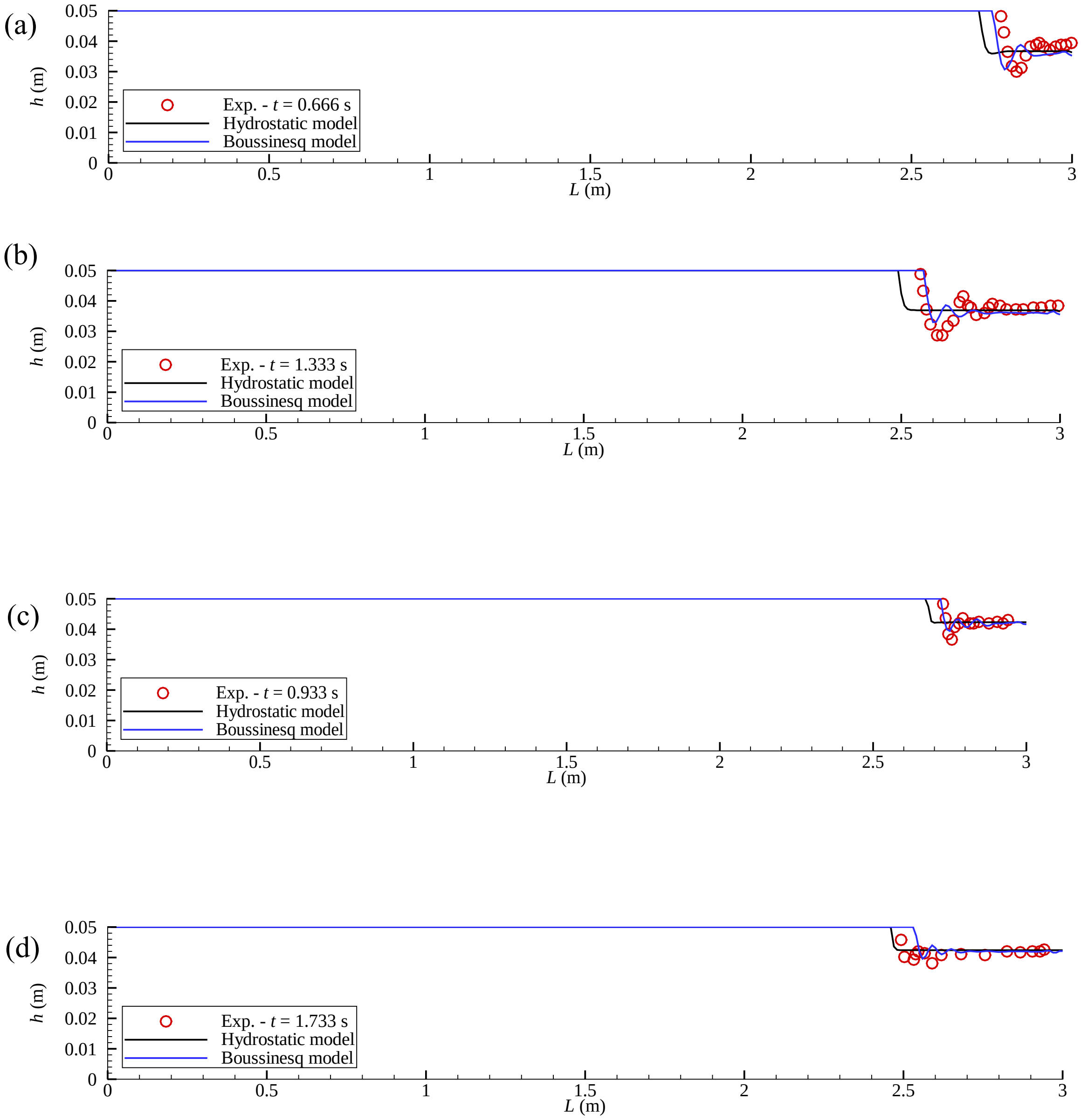

Figure 4.13: Comparison of cavity surface profile using hydrostatic and Boussinesq models: (a and b) $h_w = 0.5\ D$ and $\theta = 0^\circ$; (c and d) $h_w = 0.7\ D$ and $\theta = 0^\circ$.

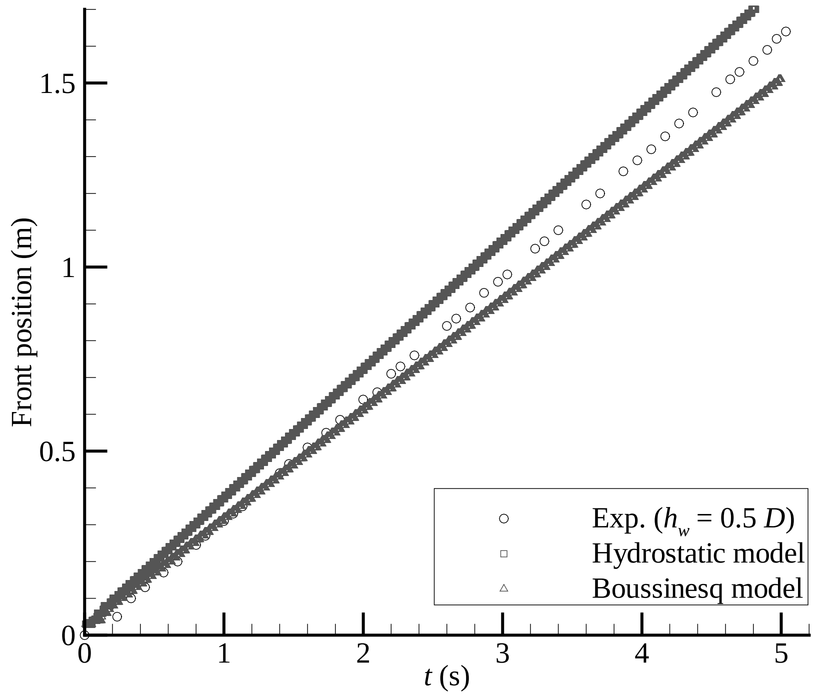

Figure 4.14: Temporal variation of air cavity front position (h_w = 0.5 D, θ = 0°).

$$Q_{out} = c_d \sqrt{2g(z_1 - h_w)}(z_1 - h_w)B_w \tag{4.65}$$

where Q_{out} = the outflow discharge; c_d = the discharge coefficient (= 0.48); z_1 = the downstream water depth; h_w = the weir height; and B_w = the weir width.

Figures 4.13(a-b) and 4.13(c-d) show the numerical simulation of water surface profile of cavity using the hydrostatic and the Boussinesq models with h_w = 0.5 D and h_w = 0.7 D, respectively. According to the results the derived Boussinesq equation could simulate the undular bore inside the circular pipe properly. Also, cavity front positions were simulated better with the Boussinesq model (Figure 4.14).

4.6 Summary

In this chapter, a numerical and experimental analysis of Benjamin's Bubble for horizontal and inclined circular pipes was presented. We have done a series of experiments with different heights of a weir at the downstream end. The numerical models for simulation of this phenomenon were based on hydrostatic assumption and Boussinesq momentum equation that was derived for the circular cross-section. The numerical algorithm used for this study was composed of 1D depth-averaged continuity and momentum equations in free surface open channel flow, pressurized flow, and the interface between them. Following are the conclusions drawn from this study:

1. Comparisons of the results that obtained by using the hydrostatic and Boussinesq momentum equations with the observed data, showed that the computed results were affected significantly by Boussinesq terms.
2. Experimental results showed that using a sufficient height of weir at the downstream end can cause the generation of undular bore.
3. In all cases, Boussinesq model could reproduce the better water surface profile, cavity front position, and cavity front shape.
4. In contrast to the rectangular duct, the hydrostatic model could reproduce a reasonable cavity front shape for a circular pipe.

Although many methods have been developed for the air-water flow in pipes, the current method is relatively easy for programming and gives good results. Extending the model for entrapped air in pipes and pipe-tank systems should be taken into account in the further research.

4.7 References

Alves, I. N., Shoham, O., and Taitel, Y. (1993). "Drift velocity of elongated bubbles in inclined pipes." *Chem. Eng. Sci.*, 48(17), 3063–3070.

Baines, W. D. (1991). "Air cavities as gravity currents on slope." *J. Hydraul. Eng.*, 117(12), 1600–1615.

Bashiri-Atrabi, H., Hosoda, T., and Tada, A. (2015). "Simulation of air cavity advancing into a straight duct." *J. Hydraul. Eng.*, 141(1), 04014068.

Benjamin, T. B. (1968). "Gravity currents and related phenomena." *J. Fluid Mech.*, 31(2), 209–248.

Boussinesq, J. V. (1871). "Theorie de l'intumescence appelée onde solitaire ou de translation se propageant dans un canal rectangulaire." *Comptes-Rendus de l'Académie des Sciences*, Paris, 72, 755–759 (in French).

Bousso, S., and Fuamba, M. (2014). "Numerical and experimental analysis of the pressurized wave front in a circular pipe." *J. Hydraul. Eng.*, 140(3), 300–312.

Cardle, J. A., Song, C. C. S., and Yuan, M. (1989). "Measures of mixed transient flows." *J. Hydraul. Eng.*, 115(2), 169–182.

Cola, R. (1967). "Esame teorico e sperimantale dei fenomeno ondosi di vuotamento di una condotta a sezione circolare." Atti dell'Istituto Veneto di Scienze, Lettere ed Arti 125, 257–294 (in French).

Cunge, J. A., and Wegner, M. (1964). "Numerical integration of Barre de Saint-Venant's flow equations by means of implicit scheme of finite differences." *Houille Blanche*, 19(1), 33–39.

Ferziger, J. and Peric, M. (1999). *Computational method for fluid dynamics*, Springer, New York.

Fuamba, M. (2002). "Contribution on transient flow modelling in storm sewers." *J. Hydraul. Res.*, 40(6), 685–693.

Ghidaoui, M. S., Ming, Z., McInnis, D. A., and Axworthy, D. H. (2005). "A review of water hammer theory and practice." *Appl. Mech. Rev.*, 58(1), 49–76.

Hager, W. H. (1999). "Cavity outflow from a nearly horizontal pipe." *Int. J. Multiphase Flow*, 25, 349–364.

Harten, A. (1983). "High resolution schemes for hyperbolic conservation laws." *J. Comput. Phys.*, 49, 357–393.

Hirt, C. W., and Cook, J. L. (1972). “Calculating three-dimensional flows around structures and over rough terrain”, *J. Comput. Phys.*, 10, 324–340.

Hosoda, T., Inoue, K., and Tada, A. (1993). “Hydraulic transient with propagation of interface between open-channel free surface flow and pressurized pipe flow.” *Proc. 5th Int. Symp. on Computational Fluid Dynamics*, JSCFD, Sendai, Japan, 1, 291–296.

Hosoda, T., Iwata, M., Muramoto, Y., and Furuhachi, T. (1997). “Hydraulic analysis of undular bore in open channels with circular cross section.” *J. Hydraul. Eng.*, JSCE, 41, 645–615 (in Japanese).

Iwasa, Y., and Inoue, K. (1982). “Mathematical simulations of channel and overland flood flows in view of flood disaster engineering.” *J. Natural Disaster Science*, 4(1), 1–30.

Jain, S. C. (2001). *Open channel flow*, Wiley, New York.

Jun, B. H. (1985). “Dynamic wave simulation of unsteady open channel and surcharge flows in sewer networks.” Ph.D. Thesis, University of Illinois at Urbana-Champaign, Ann Arbor, Michigan.

León, A. S., Ghidaoui, M. S., Schmidt, A. R., and Garcia, M. H. (2006). “Godunov-type solutions for transient flows in sewers.” *J. Hydraul. Eng.*, 132(8), 800–813.

León, A. S., Ghidaoui, M. S., Schmidt, A. R., and Garcia, M. H. (2010). “A robust two-equation model for transient mixed flows.” *J. Hydraul. Res.*, 48(1), 44–56.

Leonard, B. P. (1979). “A stable and accurate convective modelling procedure based on quadratic upstream interpolation.” *Comp. Methods in Appl. Mech. Eng.*, 19(1), 59–98.

Li, J., and McCorquodale, A. (1999). “Modeling mixed flow in storm sewers.” *J. Hydraul. Eng.*, 125(11), 1170–1180.

Lin, P. (2008). *Numerical modelling of water waves*, Taylor & Francis, London.

McCorquodale, J. A., and Hamam, M. A. (1983). “Modelling surcharged flow in swers.”

Proc. Int. Symp. on Urban Hydrol. and Sediment Control, University of Kentucky, Lexington, Ky., 331–338.

Roache, P. J. (1972). *Computational fluid dynamics,* Hermosa, Albuquerque, N. M.

Trajkovic, B., Ivetic, M., and Calomino, F. (1999). "Investigation of transition from free surface to pressurized flow in a circular pipe." *Wat. Sci. Tech.*, 39(9), 105–112.

Vasconcelos, J. G., and Wright, S. J. (2008). "Rapid flow startup in filled horizontal pipelines." *J. Hydraul. Eng.*, 134(7), 984–992.

Wiggert, D. C. (1972). "Transient flow in free-surface, pressurized systems." *J. Hydraul. Div.*, 98(1), 11–27.

Wilkinson, D. L. (1982). "Motion of air cavities in long horizontal ducts." *J. Fluid. Mech.*, 118, 109–122.

Zhou, L., Liu, D., Karney, B., and Zhang, Q. (2011). "Influence of entrapped air pockets on hydraulic transients in water pipelines." *J. Hydraul. Eng.*, 137(12), 1686–1692.

Zukoski, E. E. (1966). "Influence of viscosity, surface tension, and inclination angle on motion of long bubbles in closed tubes." *J. Fluid Mech.*, 25(4), 821–840.

Chapter 5

Three-dimensional simulation of transient mixed flows with depressurizing wavefront in a duct

5.1 Introduction

Transient flows from free surface to pressurized, or vice versa are called mixed flows and have wide applications in wastewater systems, storm sewers, hydropower plants, and underground waterways. Due to its wide range of application from agriculture to industry, it has been an interesting topic for researchers in a wide range of science for many years.

The movement of a long cavity in rectangular ducts has been studied experimentally and theoretically during the last few decades. Benjamin (1968) investigated the air cavity intrusion into a rectangular duct, caused by sudden opening of a gate at a downstream end theoretically, and after him this kind of bubble is known as Benjamin bubble. Later works, investigated the cavity shape and front velocity experimentally (Wilkinson, 1982; Hosoda et al., 1994). Regarding their findings, three types of flow can be initiated after opening the gate:

1. Energy-conserving flow, in which the flow regime is steady, and the air-water interface is located almost at the half of the duct height.
2. The flow with an unsteady regime, which consists of two parts; one is the energy-conserving region in which the length is continuously increasing, and

another is undular bore region.

3. The steady flow in which the depth beneath the cavity exceeds 0.78% of the duct height.

Baines and Wilkinson (1986) and Baines (1991) investigated the motion of large air cavities in inclined ducts experimentally and theoretically and dealt with the frontal speed and shape. Gardner and Crow (1970) examined the influence of surface tension on the bubble velocity with the assumption of the radius of curvature of the two-phase interface near the upper wall does not change with channel depth.

There are many numerical methods for simulation of the Benjamin bubble and two-phase flow in rectangular ducts or circular pipes. These models are classified based on the solution strategy, air effect, and a number of equations (Bousso et al., 2013). Bashiri-Atrabi et al. (2015b) conducted a numerical simulation for Benjamin bubble in a rectangular duct. Their results indicate that non-hydrostatic model (with higher order terms in Boussinesq equation) could better simulate the air cavity surface profile compared with the hydrostatic one. They also showed that the solitary wave equation (Iwasa, 1955) could reproduce the cavity front shape and tested their model with some experimental data. In contrast to the Boussinesq equation with higher order terms, one that is introduced by Peregrine (1985) can be used more for unsteady cases.

In the case of circular pipes, Bashiri-Atrabi et al. (2015a) conducted some experiments on horizontal and inclined slopes to observe different types of Benjamin Bubble based on the mode of generation. They derived a Boussinesq equation for circular pipes to reproduce the undular bore generated caused by a sharp-creased weir at an open end of the pipe. Their model consists of 1D shallow water equations, and they proposed a pressure drop approach at air-water interface near the stagnation point. Although, hydrostatic model in the horizontal case and without using a weir at the end showed reasonably good results compared with the experimental data, implementation of the Boussinesq model is necessary for other cases, especially for the generation of undular bore. Karney and Mclnnis (1992) implemented an explicit method based on the method of characteristics (MOC), as an efficient and simple way to calculate the transient flow in pipe networks. Hager (1999) considered the cavity shape, end depth ratio, and the jet trajectories from a circular pipe. Ramdin and Henkes (2012) used computational fluid dynamics (CFD) model to simulate the Benjamin bubble and the Taylor bubble and compared their results with the existing experimental and numerical data. Birman et al. (2007a; 2007b) conducted a 2D Navier-Stokes simulation to investigate the Benjamin bubble in a rectangular channel. Rapid advances in computer technologies persuade the researchers to use more complex CFD models.

This paper presents a 3D model to simulate Benjamin bubble in a horizontal rectangular duct. The spatial discretization of the model is based on the staggered grid system and FVM. The Euler scheme with second-order accuracy in time is used for time integration. A 3D Reynolds-averaged equation with nonlinear URANS turbulence models and standard k-ε model is used to model two-phase flow in rectangular ducts. A Hybrid central upwind scheme is applied to the k-ε equations (Spalding, 1972). The CIP-CSL2 scheme is employed to convection term in the momentum equation and advection equation of the density function (Yabe et al., 2001).

To avoiding numerical diffusion in the calculations of the advection equation of the density function, we used the STAA method (Ikebata and Xiao, 2002). SOLA iterative algorithm is used for solving the pressure in each time step (Hirt et al., 1975). The computations are carried out under the conditions of the laboratory experiments and compared with a 1D model, which presented by Bashiri-Atrabi et al. (2015b). For more evaluation of 3D model and investigation of 2D Benjamin bubble, we conducted some new experiments.

5.2 Governing Equations

5.2.1 Basic equations

The 3D, basic conservation laws of mass and momentum based on URANS model for incompressible unsteady flows are as follow:

the continuity equation

$$\frac{\partial U_i}{\partial x_i} = 0 \tag{5.1}$$

and the momentum equation

$$\frac{\partial U_i}{\partial t} + \frac{\partial U_i U_j}{\partial x_j} = g_i - \frac{1}{\rho}\frac{\partial p}{\partial x_i} + \frac{\partial}{\partial x_j}\left(\nu \frac{\partial U_i}{\partial x_j} - \overline{u_i u_j} \right) \tag{5.2}$$

where t = the time; x_i = the spatial coordinate; U_i = the Reynolds-averaged velocity; g = the gravitational acceleration; ρ = the water density; p = the averaged pressure; ν = the molecular viscosity; and $-u_i u_j$ = the Reynolds stress. The proposed 3D FVM model applied the staggered grid system according to Figure 5.1.

5.2.2 Turbulence model

The most widely applied model for modeling the turbulent flows in the industry is Reynolds-averaged Navier-Stokes (RANS) (Cheng et al., 2003). The RANS equations are time-averaged equations of motion in fluids. The RANS models require less CPU time and memory compared with some other methods such as large-eddy simulation (LES) and direct numerical simulation (DNS) (Kimura et al., 2009). The unsteady Reynolds-averaged Navier-Stokes (URANS) is one of the complex versions of RANS and is widely used to compute open channel flows. The practical importance of the URANS in hydraulics can be seen in many studies. Features of different types of URANS model and their applications are described in many papers (Spalart, 2000; Sagaut, 2006; Argyropoulos and Markatos, 2014). Jefferson-Loveday et al. (Jefferson-Loveday, 2013) used a URANS model for a simple cavity flow and realistic labyrinth seal geometry. The k-ε model is one of the famous turbulence models, which is applicable to turbulent flows. There are some modifications of k-ε model, which have proposed by Patel et al. (1985) and Wilcox (1998).

The Reynolds stress tensor is given by Yoshizawa (1984) and Kimura and Hosoda

(2003)

$$-\overline{u_i u_j} = v_t S_{ij} - \frac{2}{3} k \delta_{ij} - \frac{k}{\varepsilon} v_t \sum_{\beta=1}^{3} C_\beta \left(S_{\beta ij} - \frac{1}{3} S_{\beta\alpha\alpha} \delta_{ij} \right) \tag{5.3}$$

In which

$$S_{1ij} = \frac{\partial U_i}{\partial x_r} \frac{\partial U_j}{\partial x_r} \tag{5.4}$$

$$S_{2ij} = \frac{1}{2} \left(\frac{\partial U_r}{\partial x_i} \frac{\partial U_j}{\partial x_r} + \frac{\partial U_r}{\partial x_j} \frac{\partial U_i}{\partial x_r} \right) \tag{5.5}$$

$$S_{3ij} = \frac{\partial U_r}{\partial x_i} \frac{\partial U_r}{\partial x_j} \tag{5.6}$$

The eddy viscosity coefficient v_t and other related coefficients are expressed as

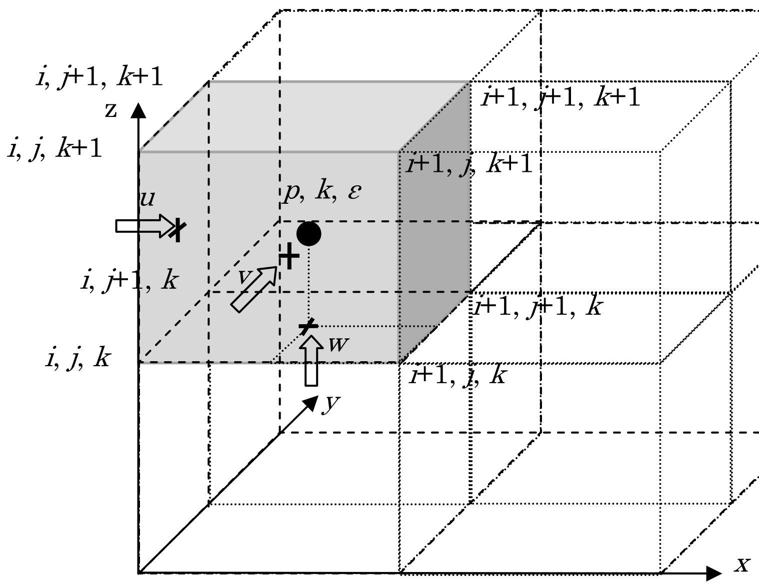

Figure 5.1: Staggered grid system and allocation of hydraulic variables.

$$\nu_t = C_\mu \frac{k^2}{\varepsilon} \tag{5.7}$$

$$C_\mu = \frac{C_{\mu 0}\left(1 + c_{nS}S^2 + c_{n\Omega}\Omega^2\right)}{1 + c_{dS}S^2 + c_{dS\Omega}S\Omega + c_{dS1}S^4 + c_{d\Omega 1}\Omega^4 + c_{dS\Omega 1}S^2\Omega^2} \tag{5.8}$$

$$C_\beta = C_{\beta 0}\frac{1}{1 + m_{dS}S^2 + m_{d\Omega}\Omega^2} \tag{5.9}$$

The ν_t is calculated using strain parameter S and rotation parameter Ω as follows

$$S_{ij} = \frac{\partial U_i}{\partial x_j} + \frac{\partial U_j}{\partial x_i} \tag{5.10}$$

$$\Omega_{ij} = \frac{\partial U_i}{\partial x_j} - \frac{\partial U_j}{\partial x_i} \tag{5.11}$$

$$S = \frac{k}{\varepsilon}\sqrt{\frac{1}{2}S_{ij}S_{ij}} \tag{5.12}$$

$$\Omega = \frac{k}{\varepsilon}\sqrt{\frac{1}{2}\Omega_{ij}\Omega_{ij}} \tag{5.13}$$

where S_{ij} = the strain tensor; Ω_{ij} = the rotation tensor; S = the strain parameter; Ω = the rotation parameter; k = the average turbulent energy; ε = the averaged rate of dissipation of turbulent kinetic energy; and $C_{\mu 0}$, c_{nS}, c_{dS}, c_{dS1}, $c_{n\Omega}$, $c_{d\Omega 1}$, $c_{dS\Omega}$, $c_{dS\Omega 1}$, m_{dS}, and $m_{d\Omega}$ = the model constants. The modeled kinetic energy k and its rate of dissipation ε, which are appeared in Equation (5.3) are given by

$$\frac{\partial k}{\partial t} + \frac{\partial kU_j}{\partial x_j} = -\overline{u_i u_j}\frac{\partial U_i}{\partial x_j} - \varepsilon + \frac{\partial}{\partial x_j}\left\{\left(\frac{\nu_t}{\sigma_k} + \nu\right)\frac{\partial k}{\partial x_j}\right\} \tag{5.14}$$

$$\frac{\partial \varepsilon}{\partial t} + \frac{\partial \varepsilon U_j}{\partial x_j} = -C_{\varepsilon 1}\overline{u_i u_j}\frac{\partial U_i}{\partial x_j} - C_{\varepsilon 2}\frac{\varepsilon^2}{k} + \frac{\partial}{\partial x_j}\left\{\left(\frac{\nu_t}{\sigma_\varepsilon} + \nu\right)\frac{\partial \varepsilon}{\partial x_j}\right\} \tag{5.15}$$

where σ_k, σ_ε, $C_{\varepsilon 1}$, and $C_{\varepsilon 2}$ are the k and ε transport equations coefficients that have been determined by Rodi (1980) (1.0, 1.3, 1.44, and 1.92, respectively).

5.3 Computational Method

5.3.1 Surface tracking (VOF method)

The VOF and level set methods are well known for the numerical simulation of the time-dependent viscous incompressible flow of multiple fluids. Moe (1993) applied a 2D VOF transient model for prediction of bubble propagation in the horizontal and inclined channels. Tomiyama et al. (Tomiyama et al., 1993) numerically modeled a 2D single bubble motion in a stagnant liquid using the VOF method. They confirmed that in their study, the VOF method could get suitable predictions of Eotvos and Morton numbers effects.

The volume-of-fluid method uses a function whose value is 1 for any cell filled with fluid and 0 by air. Tracking the free surface of water flow is governed by the density function method.

$$\phi = \begin{cases} 1 & \text{water cell} \\ 0 & \text{air cell} \end{cases} \tag{5.16}$$

The behavior of free surface can be expressed by calculating the advection equation of ϕ as follow

$$\frac{\partial \phi}{\partial t} + \nabla \cdot U\phi = 0 \tag{5.17}$$

The density function (ϕ) is used to define the physical properties of water and air such as density and viscosity by below equations

$$\rho = \rho_{air}\left(1-\phi\right) + \rho_{water}\phi \tag{5.18}$$

$$\mu = \mu_{air}\left(1-\phi\right) + \mu_{water}\phi \tag{5.19}$$

where ρ_{air} = the air density; ρ_{watet} = the water density; μ_{air} = the air viscosity; and μ_{water} =

the water density. In general, the VOF method is a simple and low-cost method to track the fluid boundaries in 2D or 3D models.

5.3.2 Surface tracking by artificial anti-diffusion (STAA)

The STAA method was used in the calculation of the advection equation of the density function to avoid the numerical diffusion (Moe, 1993). The STAA scheme does not require the interface reconstruction and is simple to use. In addition, in the STAA method, advection of the density function by a CIP scheme can yield a conservative mass of the density function and an accurate interface velocity (Xiao, 2004; Ikebata et al., 2011). STAA reduces the numerical diffusion at an interface between water and air after the calculation of VOF function. The approach is based on two steps; first constructing a level set function (*G*) and second correction of VOF function regarding to *G*. The initial value of *G* is expressed by

$$G_0(x) = \alpha(\phi - 0.5) \tag{5.20}$$

$$G_{n+1}(x) = G_n(x+\delta) + \mathrm{sig}G_n(x)|\delta| \tag{5.21}$$

where x = the location; α = the constant coefficient; and δ = the small vector toward the gas-liquid interface direction. For more information about STAA method, please refer to Ikebata et al. (2011).

5.3.3 Cubic interpolated particle (CIP)

The cubic interpolated particle (constrained interpolation profile) (CIP) method is a semi-Lagrangian numerical solver, which is a practical technique in a wide range engineering fields (Gotoh et al., 2013). Takewaki et al. (1985) presented the classical CIP method to solve the hyperbolic type equations. Later, improved CIP methods, CIP-CSL, were proposed to find a way to apply CIP method on the integrated value of f.

In this chapter, the constrained interpolation profile-conservative semi-Lagrangian scheme with second-order polynomial function (CIP-CSL2) scheme is applied to conserve the convection term in the momentum equation and the advection equation of the density function (Yabe et al., 2001). To understand the fundamental framework of CIP-CSL2 approach, 1D advection equation for a variable $f(x,t)$ is considered here. The integrated form of conservation law of transported quantity f is expressed by

$$\frac{\partial D}{\partial t} + u\frac{\partial D}{\partial x} = 0 \tag{5.22}$$

where u = the characteristic speed; D = integrated quantity ($D = \int f dx$); and f = the transported quantity. By differentiating Equation (5.22) with respects to x, a conservative form is

$$\frac{\partial D'}{\partial t} + \frac{\partial uD'}{\partial x} = 0 \tag{5.23}$$

where D' = the derivative form of f, ($D' = f$). The integral form of Equation (5.22) over a space-time control volume is expressed as

$$D_i(\mathrm{x}) = \int_{x_i}^{x} f(\mathrm{x}')dx' \tag{5.24}$$

Approximation of above profile is conducted using a cubic polynomial formula

$$D_i(\mathrm{x}) = c_{1i}(x - x_i)^3 + c_{2i}(x - x_i)^2 + f_i^n(x - x_i) \tag{5.25}$$

where c_{1i} and c_{2i} are constants to be determined. Differentiating of Equation (5.25) with respect to x yields

$$f(\mathrm{x}) = \frac{\partial D_i(\mathrm{x})}{\partial x} = 3c_{1i}(x - x_i)^2 + 2c_{2i}(x - x_i) + f_i^n \tag{5.26}$$

According to Equation (5.24) we have

$$D_i(x_i) = 0, \quad D_i(x_{iup}) = -\mathrm{sgn}(u_i)\rho_{icell}^n \tag{5.27}$$

Here,

$$iup = \begin{cases} i-1 & \text{if } u_i^n \geq 0, \\ i+1 & \text{if } u_i^n < 0, \end{cases} \qquad \mathrm{sgn}(u_i^n) = \begin{cases} +1 & \text{if } u_i^n \geq 0, \\ -1 & \text{if } u_i^n < 0, \end{cases} \tag{5.28}$$

where x_{iup} = the upwind cell; ρ^n_{icell} = the upwind total mass; and $\mathrm{icell} = i = \mathrm{sgn}(u_i)/2$. Since $\partial D / \partial x = f$, then

$$\frac{\partial D_i(\mathrm{x}_i)}{\partial x} = f_i^n, \qquad \frac{\partial D_i(\mathrm{x}_{iup})}{\partial x} = f_{iup}^n \tag{5.29}$$

The constant coefficients in Equation (5.25) are defined by

$$c_{1i} = \frac{f_i^n + f_{\mathrm{iup}}^n}{\Delta x_i^2} + \frac{2\,\mathrm{sgn}(u_i)\rho^n_{\mathrm{icell}}}{\Delta x_i^3} \tag{5.30}$$

and

$$c_{2i} = -\frac{2 f_i^n + f_{\mathrm{iup}}^n}{\Delta x_i} - \frac{3\,\mathrm{sgn}(u_i)\rho^n_{\mathrm{icell}}}{\Delta x_i^2} \tag{5.31}$$

where $\Delta x = x_{iup} - x_i$ is the grid width. The cell-integrated quantity of ρ is given by

$$\rho_i = \int_{x_{i-1}}^{x_i} f(x)dx \tag{5.32}$$

The finite difference form of ρ can be stated as

$$\rho_i^{n+1} = \rho_i^n - \Delta\rho_i + \Delta\rho_{i+1} \tag{5.33}$$

where $\Delta\rho_i$ is the flux at x_i, and the explicit form of that is defined as

$$\Delta\rho_i = \int_{x_i+\xi}^{x_i} f(x')dx = -D_i(x_i + \xi) = -(c_{1i}\xi^3 + c_{2i}\xi^2 + f_i^n \xi) \tag{5.34}$$

where ξ is the upwind displacement ($\xi = -u_i \Delta t$).

5.3.4 Solution algorithm (SOLA)

The pressure field is solved using the simplified version of the basic solution algorithm (SOLA). Hirt et al. (1975) developed the SOLA based on the marker-and-cell (MAC) method to simulate free surface flows. In summary, the main steps of SOLA method are:

1. Approximation of new time step velocity using the initial condition and previous time step values
2. Adjusting the pressure and velocity in each cell, to satisfy the continuity equation
3. Calculation of momentum equation

5.4 Numerical Tests

The 3D model is validated through a numerical model and a series of previous and new experiments; includes 1D depth-averaged Boussinesq model (Bashiri-Atrabi et al., 2015b), 1D Benjamin bubble experimental data (Hosoda et al., 1994), 2D dam-break flow experimental data, and 2D Benjamin bubble experimental data. The main purpose of conducting the 2D Benjamin bubble experiment was observation of an air cavity advancing into the pressurized part.

5.4.1 1D Benjamin bubble (lock exchange)

Hosoda et al. (1994) studied the lock exchange flow in a horizontal rectangular conduit experimentally and numerically. They conducted some experiments in a closed horizontal duct with a vertical barrier in the middle, so-called lock-exchange experiments. A schematic diagram of the lock-exchange experiment is shown in Figure 5.2. The duct was 200 cm long, 5 cm wide and 10 cm deep. The duct was divided into two equal sections, and one vertical gate was installed in the middle of setup. One side was filled with water, and another side was empty. The air-water flow was started by rapidly removing the vertical gate. According to Figures 5.3(b) and 5.3(c), for generating the undular bore, two different tailwater were used. Figure 5.3 shows different types of flow based on different tailwater depth. Three different cases, tailwater = 0-0.7 H, are examined under the experimental condition. In addition, the 3D calculated results are compared with the 1D Boussinesq model (Bashiri-Atrabi et al., 2015b). Figure 5.4 shows water depth magnitude contour plots for k-ε URANS model.

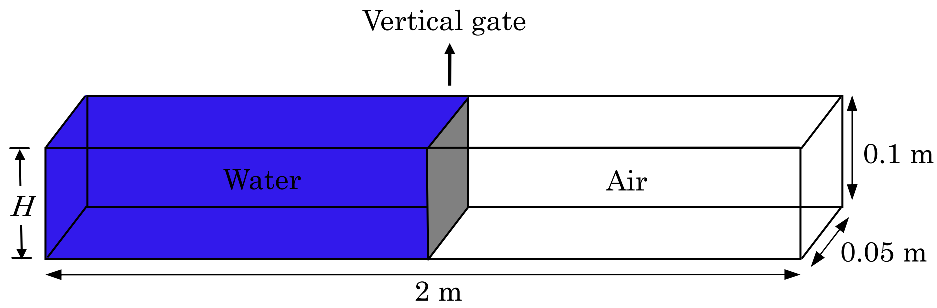

Figure 5.2: Sketch of 1D Benjamin Bubble experiment conducted by Hosoda et al.

This demonstrates clearly the transient pressurized-free surface flow in a rectangular duct. Figures 5.5-5.7 show the comparisons between 3D calculated water surface profile with the experimental data and 1D Boussinesq model. The water surface profiles are reproduced reasonably well in each computational case. Temporal variation of stagnation points in 3D model are compared with the experimental data (Figure 5.8).

The computation variables in simulations are: Manning roughness (n) =0.01 $m^{-1/3}s$, slope = 0, Δt = 0.001 s and Δx = 0.02 m for 1D model, and Δt = 0.0005 s, $\Delta x = \Delta y = \Delta z$ = 0.005 m for 3D URANS model. The volume changes during the simulation using 3D URANS model are shown in Figure 5.9, and are calculated as follows

$$\text{volume changes (\%)} = \frac{\text{present volume} - \text{initial volume}}{\text{initial volume}} \times 100 \tag{5.35}$$

5.4.2 2D Benjamin bubble (pressurized-free surface flow)

In this section, our main goal is characteristics investigation of Benjamin bubble in two directions and verification the proposed 3D URANS model. Experiment simulating 2D Benjamin bubble movement was performed at the River System Engineering and Management Laboratory of the Kyoto University. The setup for this experiment is illustrated in Figure 5.10. A Perspex square tank, of height H = 0.093 m, and length L = 0.75 m was divided into two parts by an L-shape vertical sliding gate, placed at 0.15 m

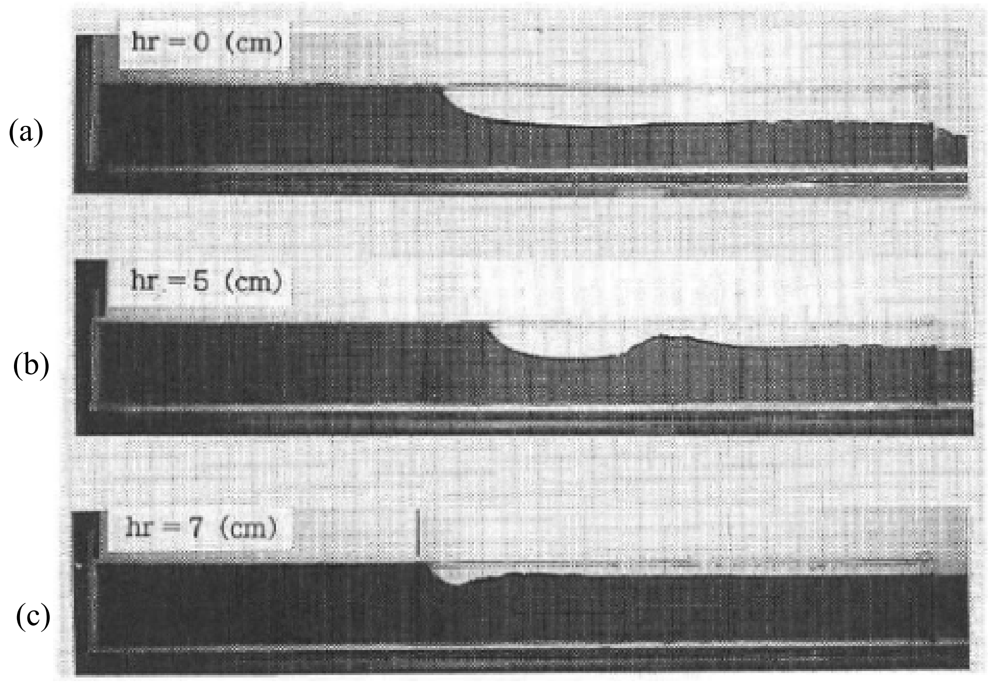

Figure 5.3: Benjamin bubble initiated by opening the downstream end gate (Hosoda et al., 1994) (a) tailwater depth = 0, (b) tailwater depth = 0.5 H, and (c) tailwater depth = 0.7 H.

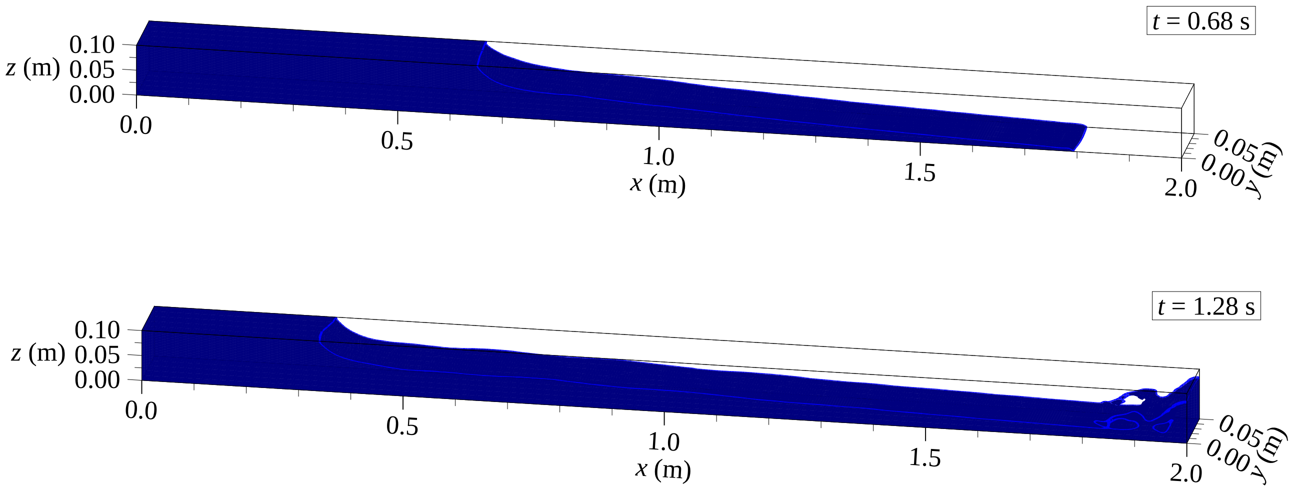

Figure 5.4: 3D URANS simulation results ($h_t = 0$).

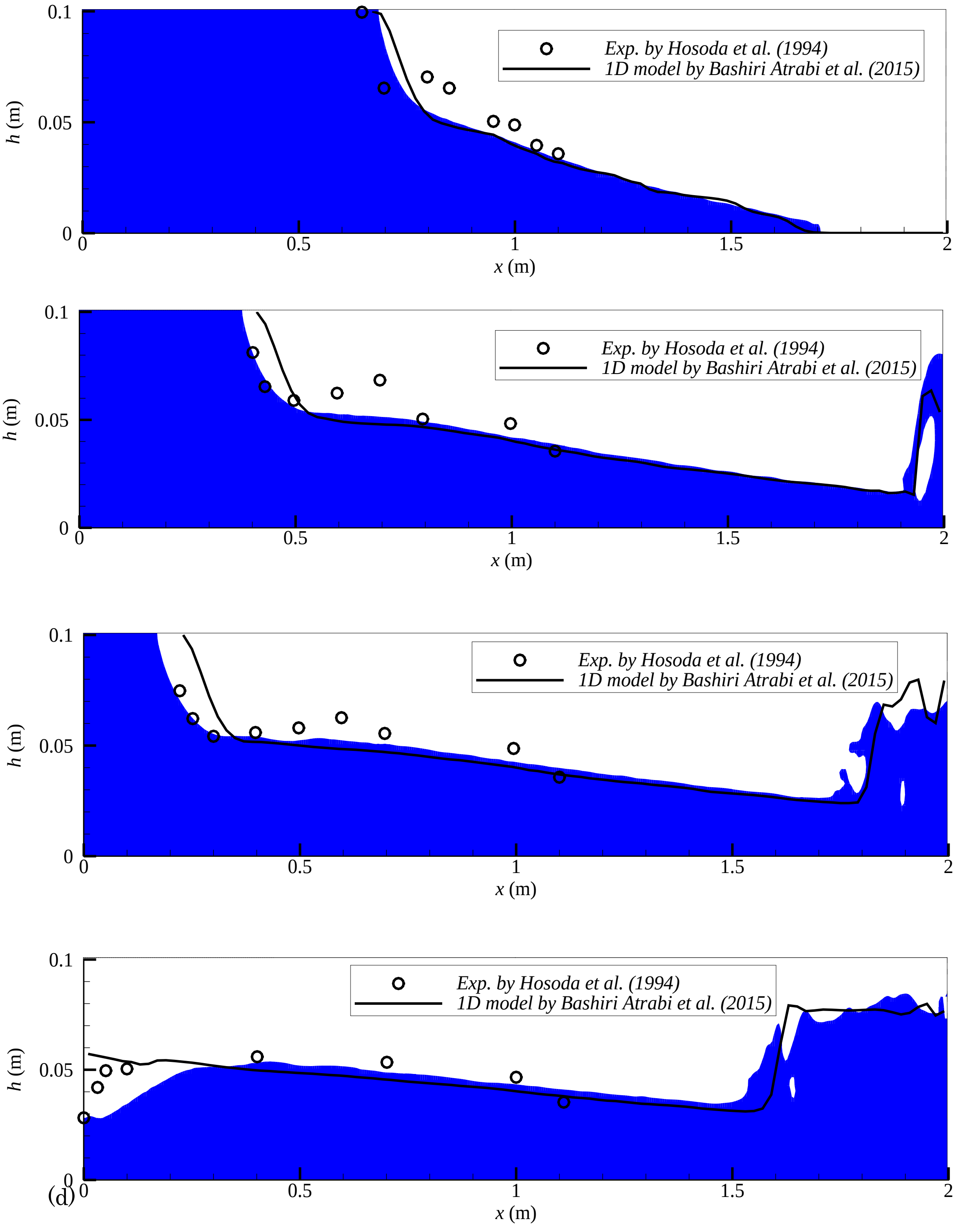

Figure 5.5: Comparison between 3D model, 1D model, and experimental data by Hosoda et al. (1994) ($h_t = 0$).

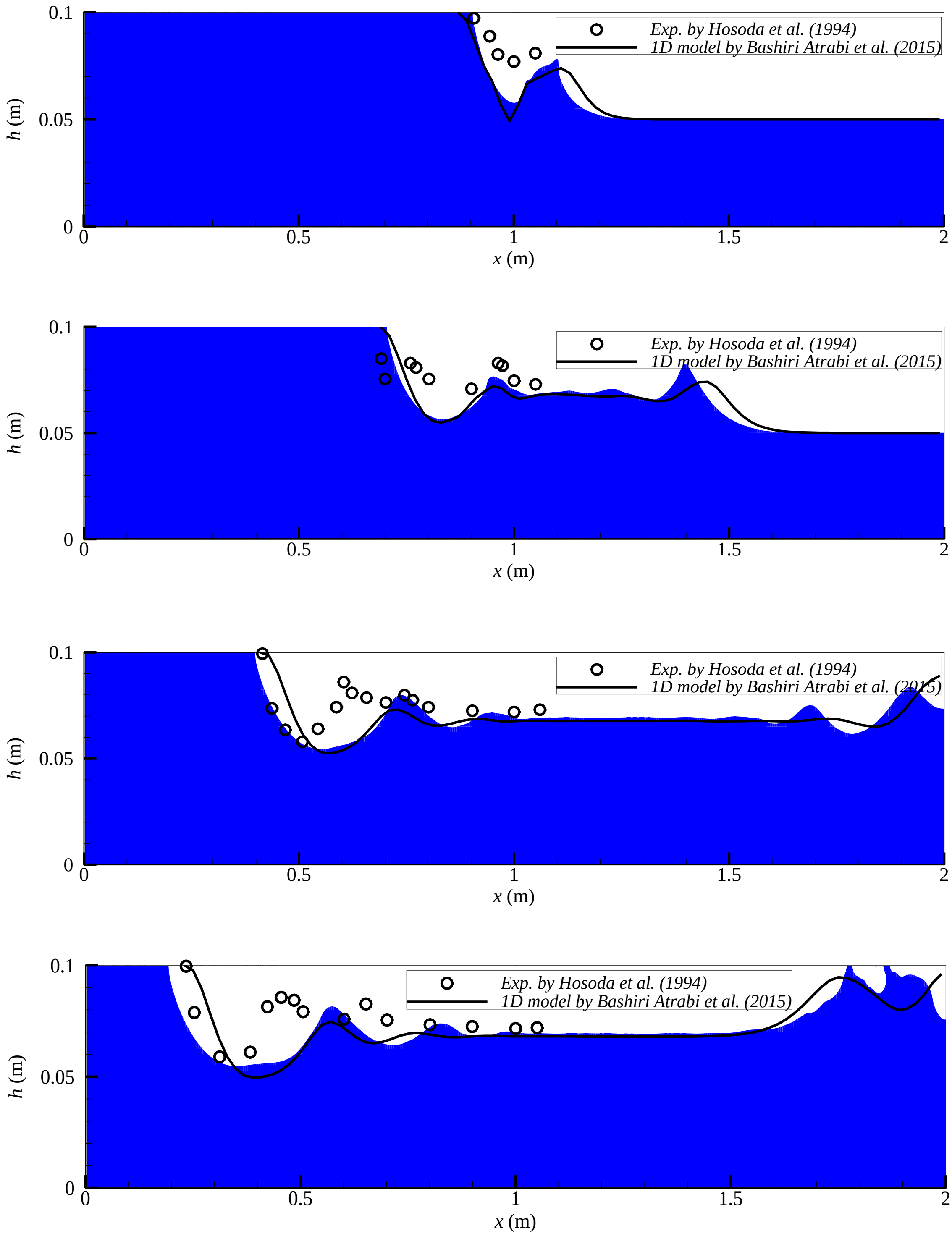

Figure 5.6: Comparison between 3D model, 1D model, and experimental data by. Hosoda et al. (1994) ($h_t = 0.5H$).

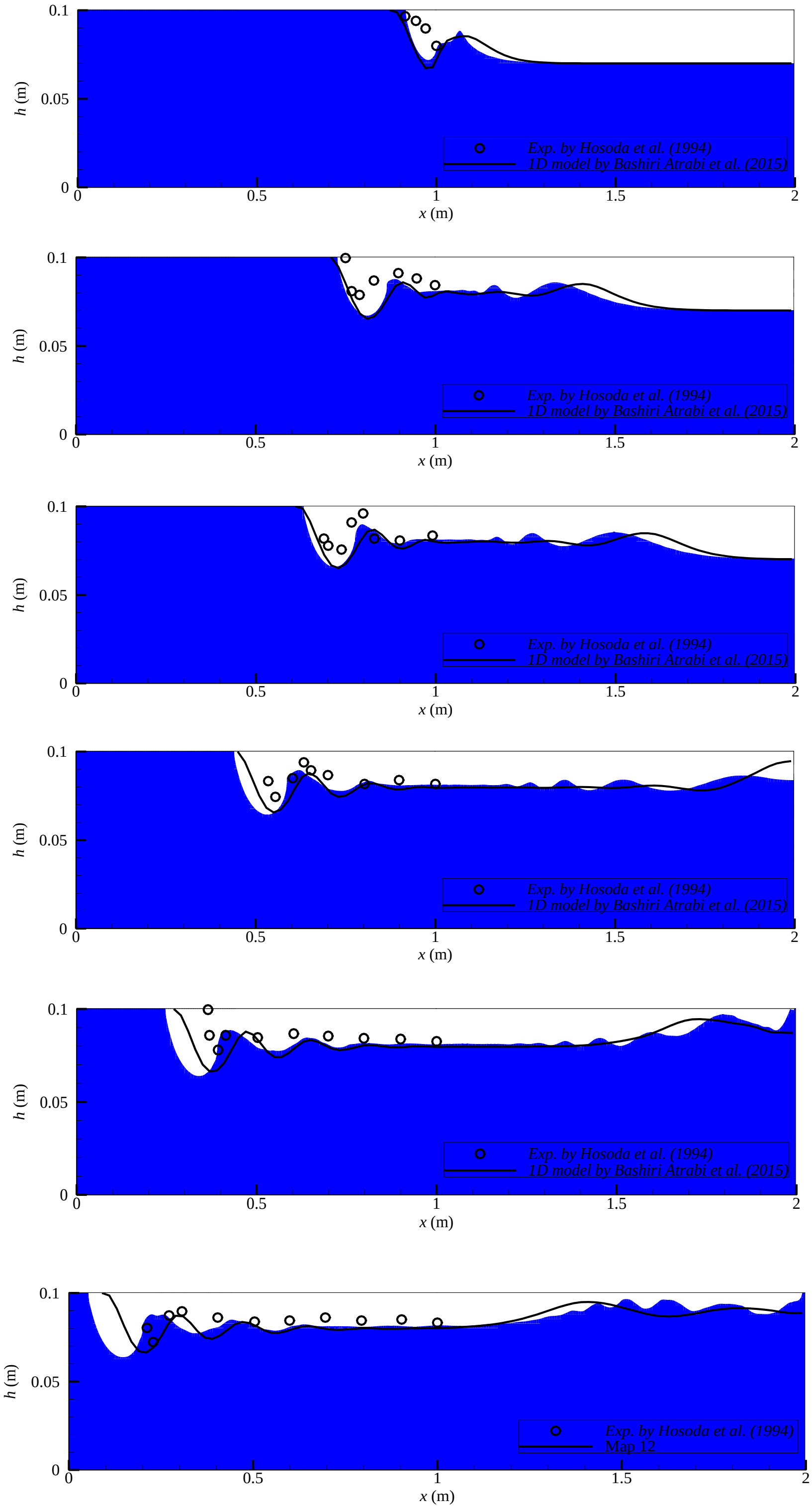

Figure 5.7: Comparison between 3D model, 1D model, and experimental data by Hosoda et al. (1994) ($h_t = 0.7\ H$).

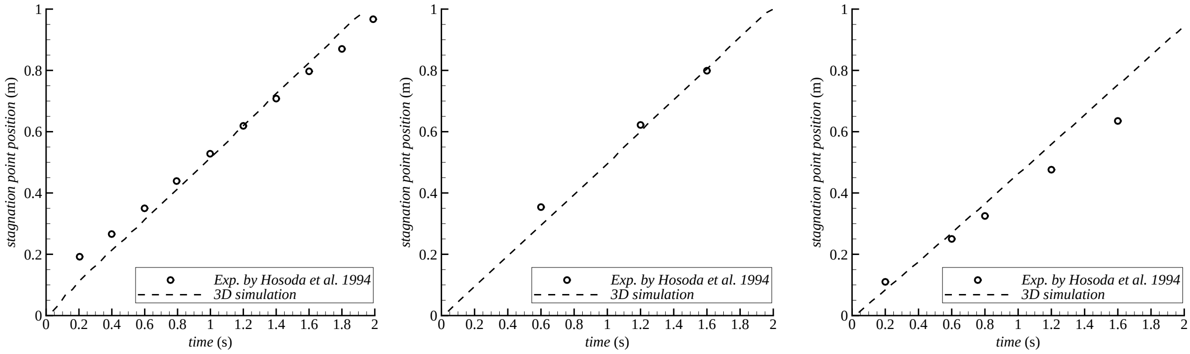

(a) (b) (c)

Figure 5.8: Comparison between calculated stagnation positions and experimental data (a) $h_t = 0$, (b) $h_t = 0.5\ H$, and (c) $h_t = 0.7\ H$.

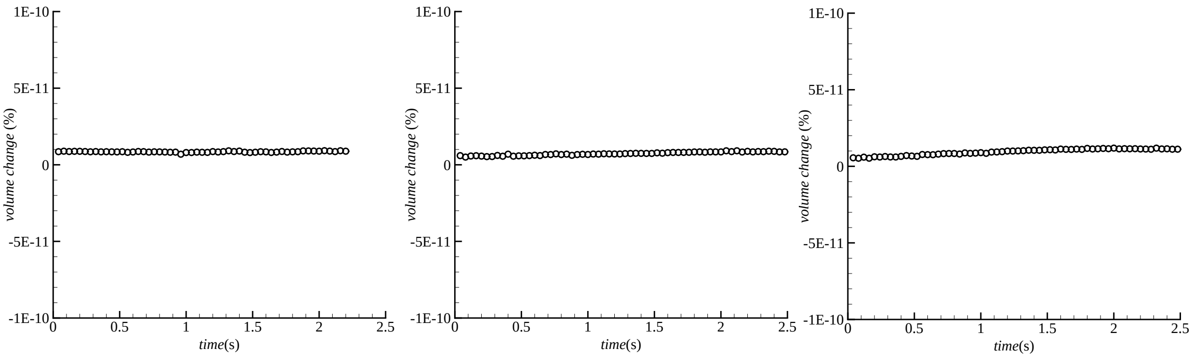

(a) (b) (c)

Figure 5.9: Volume conservation in 3D simulations (a) $h_t = 0$, (b) $h_t = 0.5\ H$, and (c) $h_t = 0.7\ H$.

from the left end of the tank, as shown in the Figure 5.10. The experimental setup was installed on a horizontal slope. The left side of the tank was filled with fresh water to a height of $H = 0.093$ m. Water was dyed with a small amount of red color for the purpose of flow visualization. A rigid plastic sheet, which acted as a roof of the tank (pressurized part), was then put on the left tank. The experiment was performed with gravity currents by releasing the water from the full-depth lock-release experiment. After removing the gate, the air cavity propagated in x-y directions. Three cameras recorded the experiment, one from the top, and two from x-y directions, and video images analyzes were used to extract the cavity front positions and water surface profiles. Figure 5.11 shows numerical results for 2D Benjamin bubble at various times. Pressurized region shape is simulated in Figure 5.1, at t = 0.1 and 0.2 s while the shape is exactly similar to the experimental findings. For more examination, we plotted experimental data at the border of the pressurized part and free surface region and compared them with the numerical results from the top view. As Figure 5.12 shows, numerical results show good agreement with the experimental data in the point of view of pressurized region shape and free surface front at downstream.

For an evaluation of the model, we extracted experimental data from side view photos and compared them with the calculated results, which are seen in Figure 13. According to these results, numerical cavity front position is a little bit faster than experimental data. The reason for this displacement can be surface tension force in experiments.

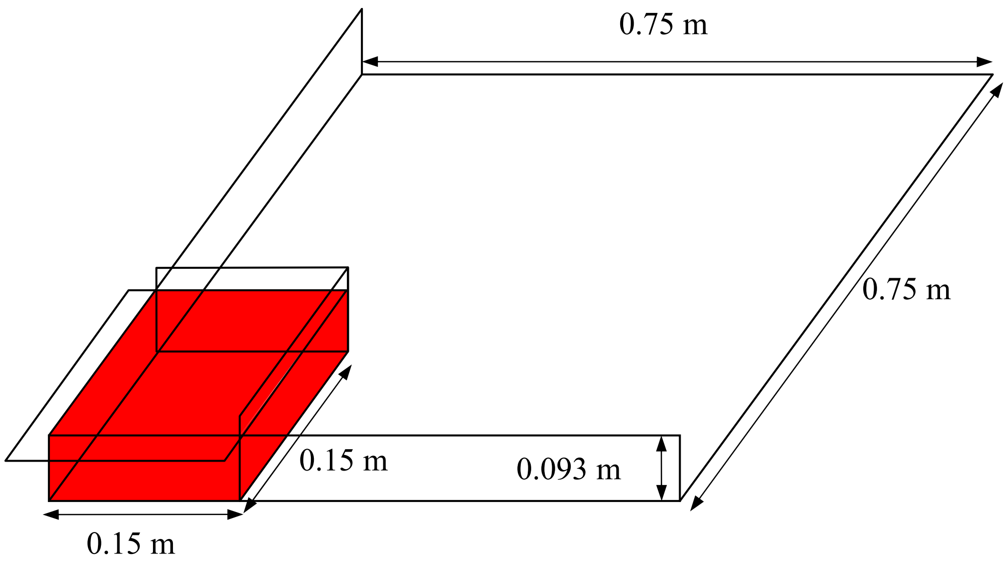

Figure 5.10: Schematic view of the 2D Benjamin bubble experimental setup. A water column is suited to the left.

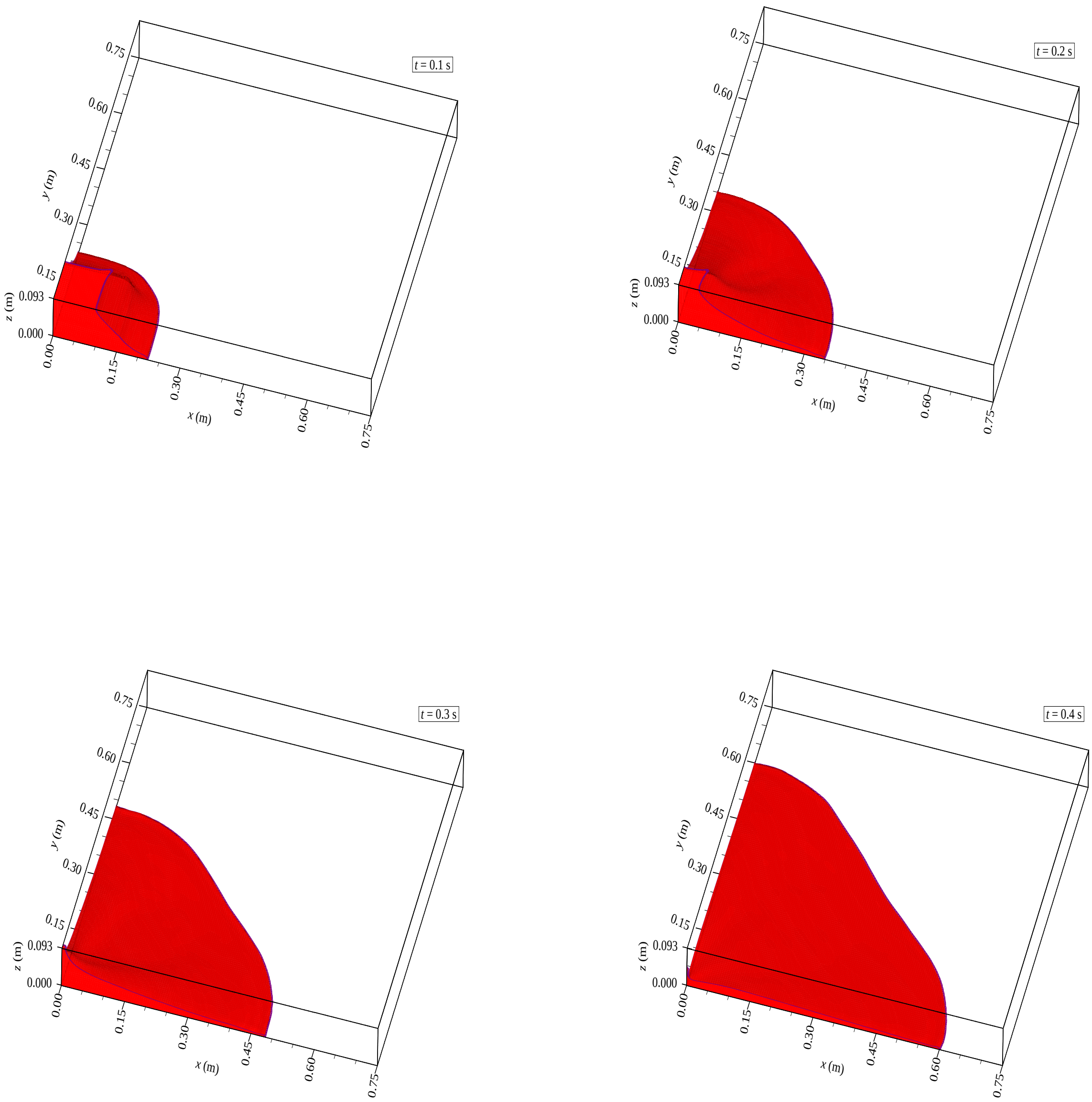

Figure 5.11: 3D URANS simulation of the 2D Benjamin bubble.

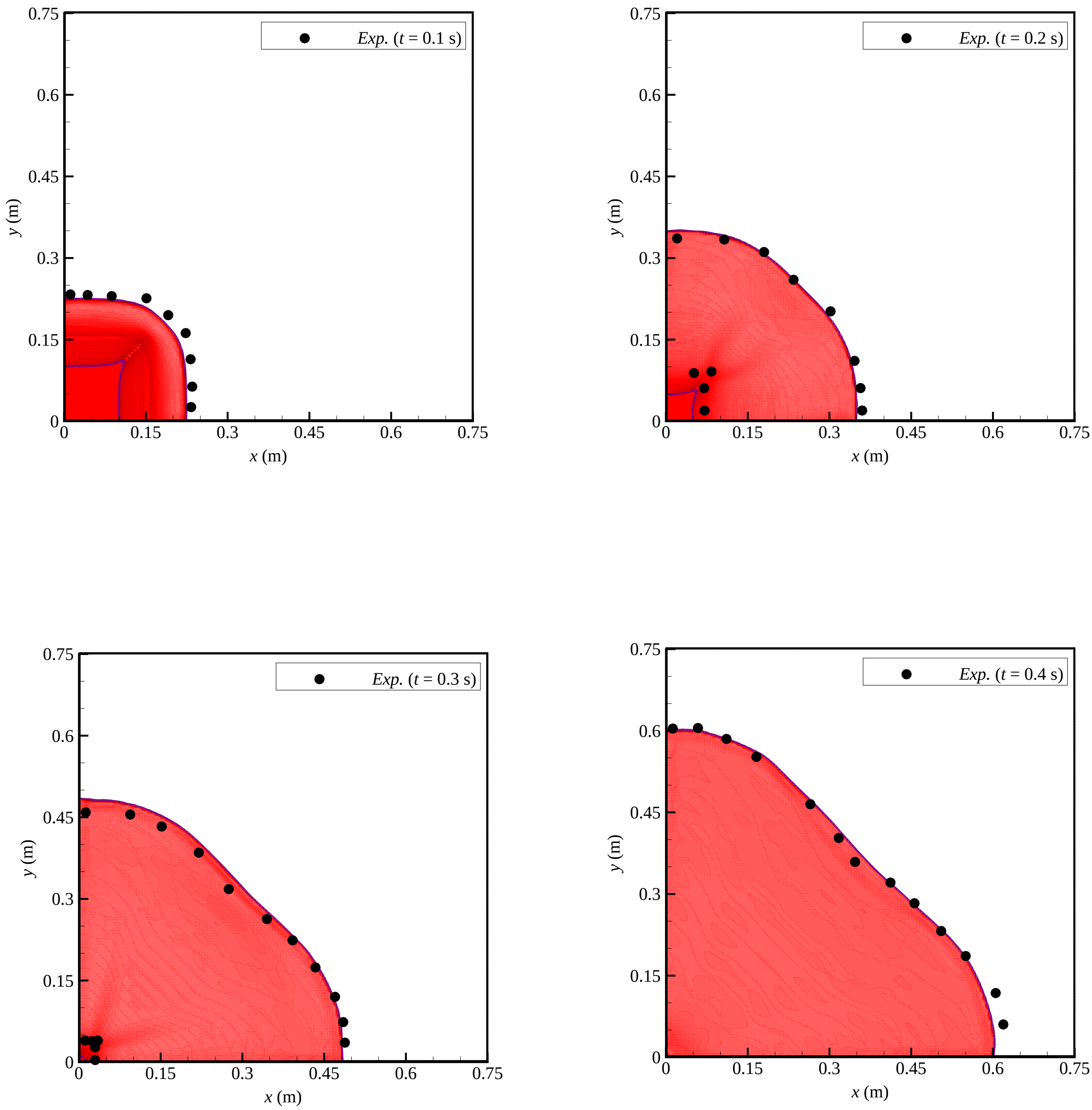

Figure 5.12: Comparison of simulation results with the experimental data (top view).

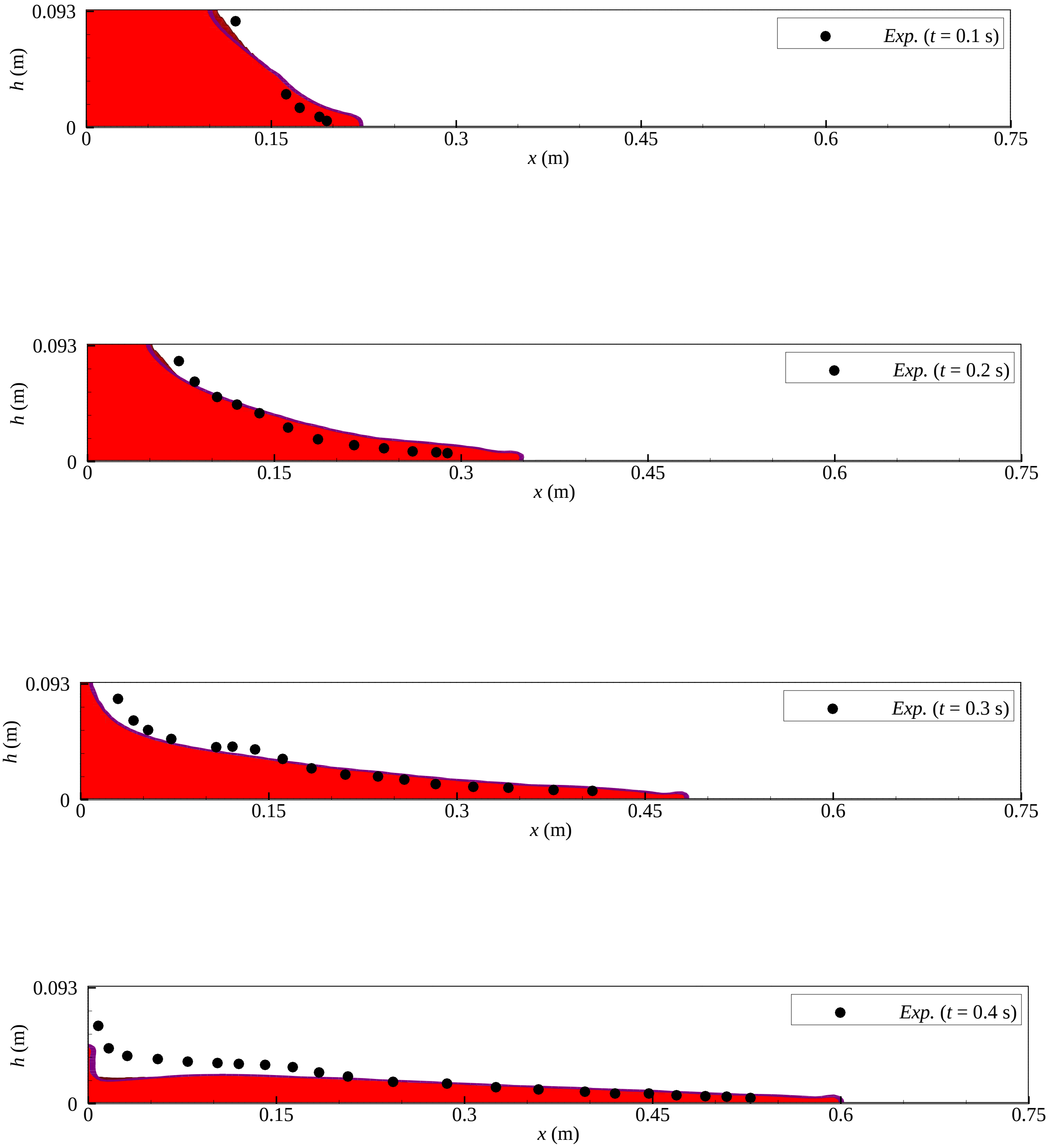

Figure 5.13: Comparison of water surface profiles using the 3D URANS model and the experimental data (side view).

5.4.3 2D dam-break flow

A fully dam-break problem is considered to verify the 3D URANS model and clear the differences between 2D Benjamin problem and full dam-break problem. In contrast to the 2D Benjamin experiment, in this case, we did not use a plate to pressurize the flow at the left side of Figure 5.10. Other conditions of the experiment were exactly similar to the 2D Benjamin experiment. After removing the L-type vertical gate, the different water surface profile was observed. 3D calculation of such kind of problem is shown in Figure 6.14. The numerical variables such as n, Δt, Δx, Δy, and Δz were chosen same as the previous section. According to Figure 5.15, compare to the 2D Benjamin problem, waterfront position is faster in this case. Comparison results, as shown in Figure 5.16, show that the current model simulates water surface profile well from the side view.

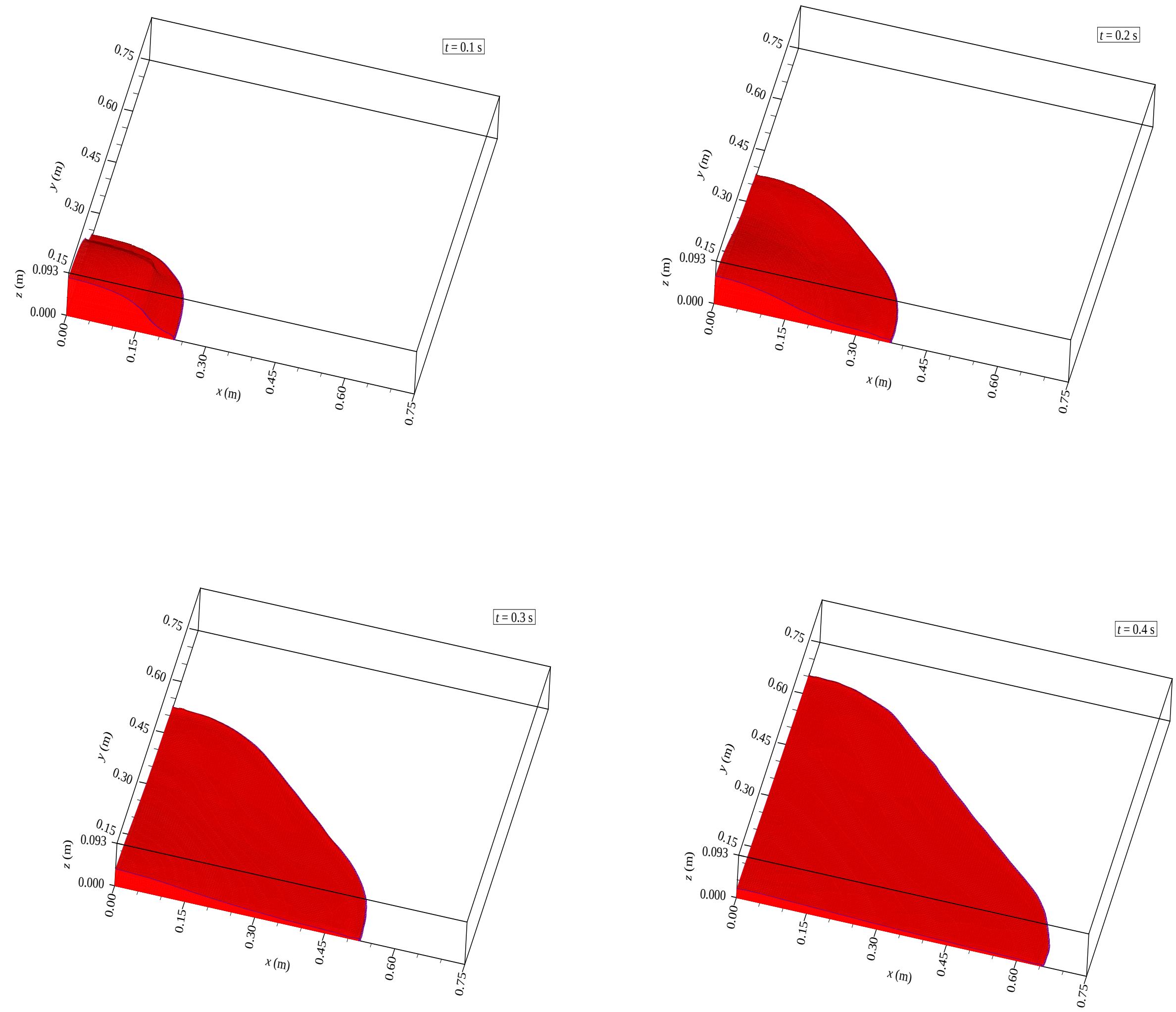

Figure 5.14: 3D URANS simulation of the dam-break flow.

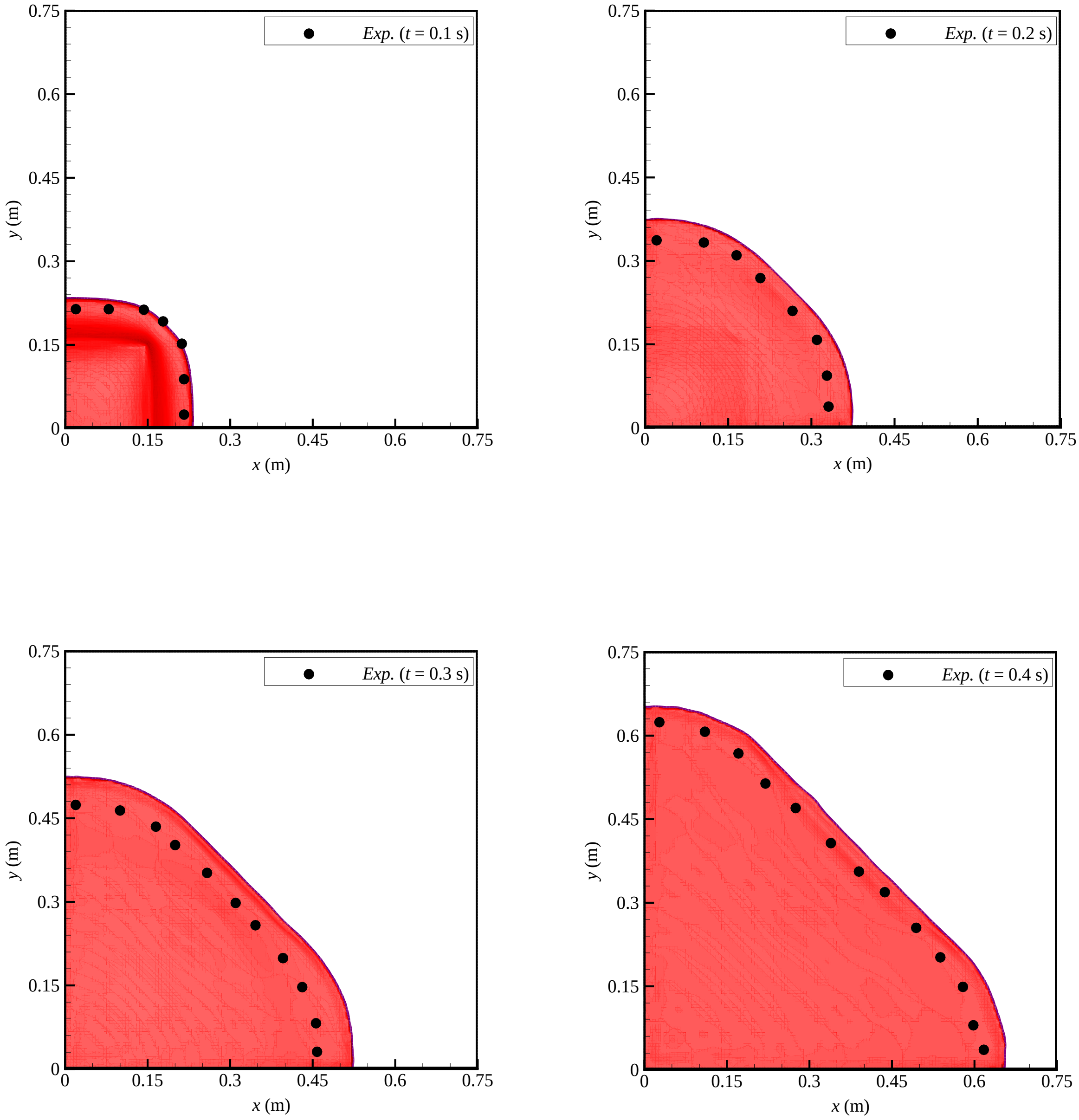

Figure 5.15: Comparison of simulation results with the experimental data (top view).

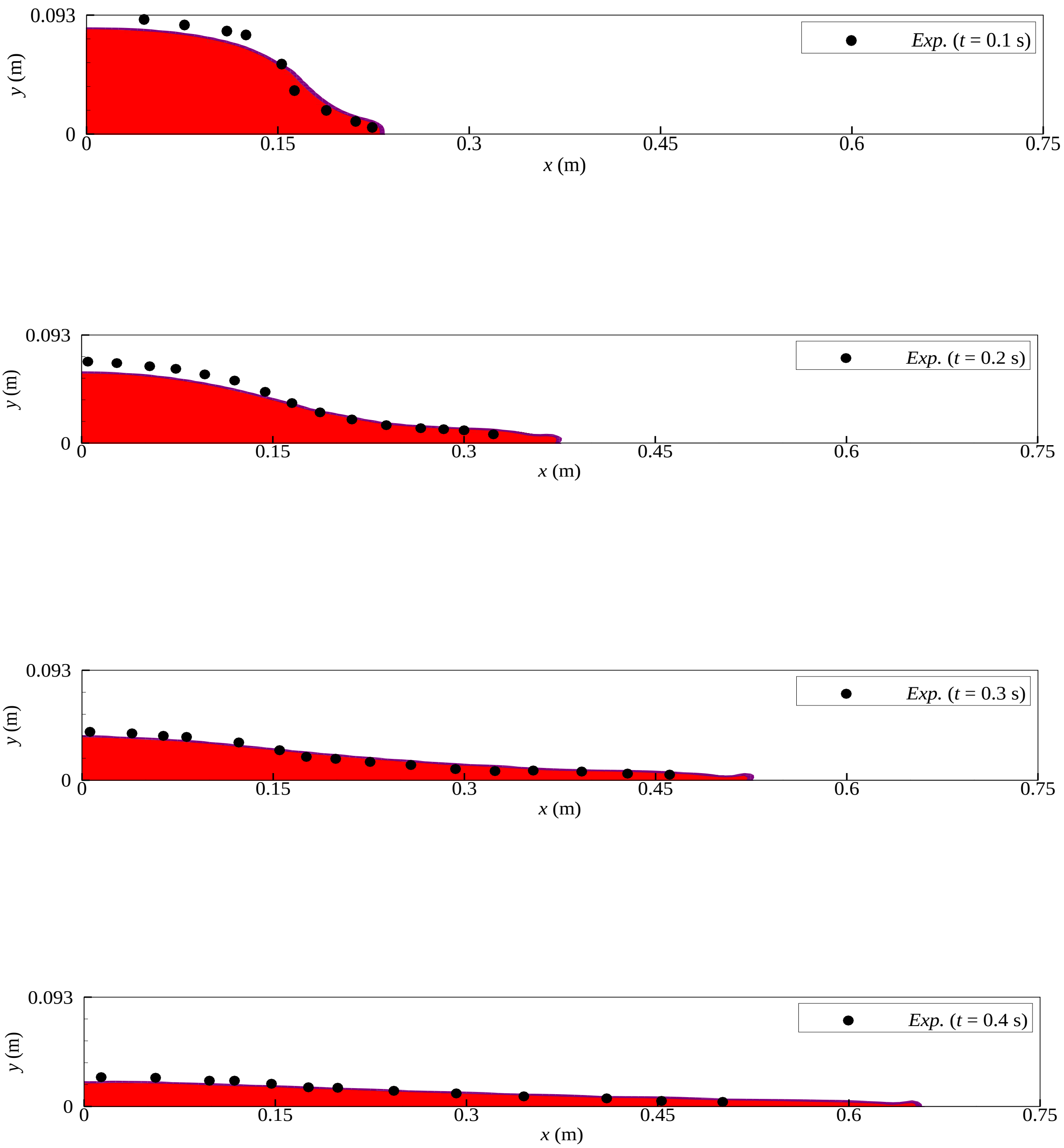

Figure 5.16: Comparison of simulated results with the dam-break experimental data (side view).

5.5 Summary

In this chapter, we have studied the propagation of an air cavity in transient pressurized-free surface flow in a channel of square cross-section experimentally and numerically. We have conducted two series of experiments in which we measured the front positions and water surface profiles. The aim of conducting two set of experiments was observation of Benjamin bubble in two directions and comparison the results with the simple dam-break problem. The fresh water and air were selected as two-phase flow in the experiments. 3D computations with URANS-type turbulence model were developed and verified trough a series of test problems. This model is compared with the non-hydrostatic 1D model. The model utilizes the full staggered grid system and applies the FVM scheme to the continuity and the momentum equations.

The computational results for the problems pointed acceptable accuracy of the 3D URANS model to a wide range of mixed flow problems in a rectangular duct. The positions of interfaces, front positions of free surface flow, and water surface profiles were quite well simulated. Although the 1D Boussinesq model showed good results in the first case, it has limitations in simulating the complex transient flows. For the simulation of 1D Benjamin bubble, the 1D model has superiority in less consumption of time, and economic cost compare to the 3D model.

Finally, it is concluded that the 3D model is more stable and sufficiently accurate. Improvement of the model to simulate the confined cavity will be achieved with compressible fluid assumptions. Future research will focus on the application of the 3D model for confined cavities, more complex geometry, and circular pipes.

5.6 References

Argyropoulos, C. D, and Markatos, N. C. (2014). "Recent advances on the numerical modeling of turbulent flows." *J. Appl. Math. Model.* doi: http://dx.doi.org/10.1016/j.apm.2014.07.001.

Baines, W. D. (1991). "Air cavities as gravity currents on slope." *J. Hydraul. Eng.*, 117(12), 1600–1615.

Baines, W. D., and Wilkinson, D. L. (1986). "The motion of large air bubbles in ducts of moderate slope." *J. Hydraul. Res.*, 25(3), 313–327.

Bashiri-Atrabi, H, Hosoda, T, and Shirai, H. (2015a). "Experimental and numerical analysis of air cavity intrusion in a horizontal circular pipe." *J Japan Soc. Civil Eng.*, 71(4), I_181-I_186.

Bashiri-Atrabi, H, Hosoda, T, and Tada, A. (2015b). "Simulation of air cavity advancing into a straight duct." *J. Hydraul. Eng.*, 141(1), 04014068.

Benjamin, T. B. (1968). "Gravity currents and related phenomena." *J. Fluid Mech.*, 31(2), 209–248.

Birman, V. K., Battandier, B. A., Meiburg, E., and Linden, P. F. (2007). "Lock-exchange flows in sloping channels." *J. Fluid Mech.*, 577, 53–77.

Birman, V. K., Martin, J. E., and Meiburg, E. (2007). "The non-Boussinesq Lock-exchange problem." Part 2. High-resolution simulations, *J. Fluid Mech.*, 537, 125–144.

Bousso, S., Daynou, M., and Fuamba, M. (2013). "Numerical modeling of mixed flows in storm water systems: critical review of literature." *J. Hydraul. Eng.*, 139(4), 385–396.

Cheng, Y., Lien, F. S., Yee, E., and Sinclair, R. (2003). "A comparison of large eddy simulations with a standard k-ε Reynolds-averaged Navier-Stokes model for the prediction of a fully developed turbulent flow over a matrix of cubes." *J. Wind Eng. Indus. Aerody.*, 91(11), 1301–1328.

Gardner, G. C., and Crow, I. G. (1970). "The motion of large bubbles in horizontal channels." *J. Fluid Mech.*, 43(2), 247–255.

Gotoh, H., Okayasu, A., and Watanabe, Y. (2013). *Computational Wave Dynamics*, World Scientific, Singapore.

Hager, W. H. (1999). "Cavity outflow from a nearly horizontal pipe." *Int. J. Mult. Flow*, 25, 349–364.

Hirt, C. W., Nicholas, B. D., and Romero, N. C. (1975). *SOLA: A numerical solution algorithm for transient fluid flows*, Los Alamos Scientific Laboratory report LA-5852.

Hosoda, T., Tada, A., Inoue, K., and Kitahara, M. (1994). "Hydraulic analysis of unsteady flows with propagation of an interface between free surface and pressurized flow." *J. Hydraul. Eng.*, Coastal, and Environmental Engineering, JSCE, Japan, 503(2), 89–97.

Ikebata, A., Muraoka, Y., and Xiao, F. (2011). "Multiphase fluid simulations on a multiple GPGPU PC using unsplit time integration VSIAM3." *Prog. in Nuc. Sci. and Tech.*, 2, 491–497.

Ikebata, A., and Xiao, F. (2002). *Multi fluid simulation with conservative momentum equation solver and front capturing scheme*, Nihon Kikai Gakkai Keisan Rikigaku Koenkai Koen Ronbunshu, 15, 499–450.

Iwasa, Y. (1955). "Analytical considerations on cnoidal and solitary waves." *Memoirs of the Fac. of Eng.*, Kyoto Univ., 17(4), 264–276.

Jefferson-Loveday, R. J. (2013). "High-order detached eddy simulation, zonal LES and URANS of cavity and labyrinth seal flows." *Int. J. Num. Meth. Fluids*, 73, 830–846.

Karney, B. W., and Mclnnis, D. (1992). "Efficient calculation of transient flow in simple pipe networks." *J. Hydraul. Eng.*, 118(7), 1014–1030.

Kimura, I., and Hosoda, T. (2003). "A non-linear k-ε model with realizability for prediction of flow around bluff bodies." *Int. J. Num. Meth. Fluids*, 42, 813–837.

Kimura, I., Ujittewaal, W. S. J., Hosoda, T., and Shahjahan-Ali, M. d. (2009). "URANS computations of shallow grid turbulence." *J. Hydraul. Eng.*, 135(2), 118–131.

Moe, R. (1993). "Transient simulation of 2-3D stratified and intermittent two-phase flows. Part II: application.” *Int. J. Num. Meth. Fluids*, 16, 967–988.

Patel, V. C., Rodi, W., and Scheuerer, G. (1985). “Turbulence models for near-wall and law-Reynolds number flows: a review.” *AIAA J.*, 23, 1308–1319.

Peregrine, D. H. (1985). “Calculations of the development of an undular bore.” *J. Fluid Mech.*, 25(2), 321–330.

Ramdin, M., and Henkes, R. (2012). “Computational fluid dynamics modeling of Benjamin and Taylor bubbles in two-phase flow in pipes.” *J. Fluids Eng.* (ASME), 134:1–8.

Rodi, W. (1980). *Turbulence models and their application in hydraulics–A state-of-the art review*, Delft, the Netherlands: IAHR publication.

Sagaut, P. (2006). *Large eddy simulation for incompressible flows*, Springer: Berlin, Germany, 1–575.

Spalart, P. R. (2000). “Strategies for turbulence modeling and simulations.” *J. Heat Fluid Flow*, 21, 252–263.

Spalding, D. B. (1972). “A novel finite difference formulation for differential expressions involving both first and second derivatives.” *Int. J. Num. Meth. Fluids*, 4, 551–5559.

Takewaki, H., Nishiguchi, A., and Yabe, T. (1985). “Cubic interpolated pseudo-particle method (CIP) for solving hyperbolic-type equations.” *J Comput. Phys.*, 61(2), 261–268.

Tomiyama, A., Zun, I., Sou, A., and Sakaguchi, T. (1993). “Numerical analysis of bubble motion with the VOF method.” *Nuclear Eng. Des.*, 141, 69–82.

Wilcox D. C. (1998). *Turbulence modeling for CFD*. DCW Industries, Inc., California.

Wilkinson, D. L. (1982). “Motion of air cavities in long horizontal ducts.” *J. Fluid. Mech.*, 118, 109–122.

Xiao, F. (2004). “Multi-fluid simulation using CIP finite volume method VSIAM3.” European Congress on Computational Methods in Applied Science and

Engineering.

Yabe, T., Tanaka, R., Nakamura, T., and Xiao, F. (2001). "An exactly conservative semi-Lagrangian scheme (CIP-CSL) in one dimension." Monthly weather review, 129, 332–344.

Yoshizawa, A. (1984). "Statistical analysis of the deviation of the Reynolds stress from its viscosity representation." *Phys*. *Fluids*, 27(6), 1377–1387.

Chapter 6

A two-dimensional model for mixed flows simulation

6.1 Introduction

The transition between pressurized flow and free surface flow is one of the interesting topics in mixed-flow conditions. This kind of flow is relevant in many environmental hydraulics and industrial engineering domains. The primary study of this type of flow was conducted by Benjamin (1968) in a rectangular duct. The so-called Benjamin flow has been studying by many researchers since 1968. He analyzed the flow by energy-conserving theory in one-dimensional (1D) case. Later, Wilkinson (1982) conducted few experiments in a square duct. A sluice gate was installed at one side of a closed horizontal duct in his experiments. In some cases, a sharp crested weir was installed at the outlet. Initially, the duct was full of water and after opening the gate he observed different kinds of flow depended on the height of the weir. This transition flow from pressurized to free surface flow (mixed-flow) can be seen in many hydraulic systems (drainage systems, storm sewer systems, hydropower plants, and pipeline pump stations).

Baines (1991) carried out more experiments compared to Wilkinson (1982). He extended Wilkinson (1982) experiments and conducted in an inclined duct. Based on his observations, he categorized the cavity advancing in a duct into four different kinds (free-overfall, lock exchange, controlled buoyancy flux, and finite volume cavity). Cavity front velocity and shape were discussed in his paper based on Benjamin (1968) theory. Bashiri-Atrabi et al. (2015b) studied Benjamin flow numerically using a 1D model. They proposed a numerical method and simulated different experimental conditions using hydrostatic and Boussinesq models. Their results showed that using a damping function in Boussinesq model can reproduce better results. They also showed that the solitary wave equation is applicable to simulate the cavity front surface profile in a duct properly. Bashiri-Atrabi et al. (2015a) also investigated the propagation of an air cavity into a horizontal circular pipe, experimentally and numerically. They found different types of cavity profile inside the circular pipe and could appropriately simulate them using a Boussinesq model.

Many 2D unsteady free surface flow models have been used by a number of investigators (Fennema et al., 1990; Zhao et al., 1994; Unami et al., 1999; Yoon and Kang, 2004; Sharifi et al., 2015). Fennema et al. (1990) used MacCormack and Gabutti explicit finite-difference schemes for 2D unsteady varied flows. They applied their model for partial dam-break and flood wave propagation problems. Zhao et al. (1994) presented a 2D unsteady flow model based on the finite volume method on the unstructured grid system, and the results showed that their model is applicable for dam-break simulations. Yoon and Kang (2004) employed a second-order upwind finite volume method on unstructured grids for shallow water equations. Unami et al. (1999) developed a numerical model using the finite element and finite volume methods for 2D free surface flow.

In this chapter, we extend the Benjamin flow over a two-dimensional case. We describe an experimental technique and present a numerical method to simulate a 2D Benjamin flow in a square box. A numerical model based on the finite volume method is developed in this study. The model is consists of 2D continuity and momentum equations under hydrostatic pressure. The fundamental continuity and momentum equations for free surface flow, pressurized flow and interface between them are used to simulate the 2D cavity advancing. After tracking interfaces, a 2D pressure drop model is applied. Comparisons between the experiments and numerical simulations are shown in later parts. Results show that current 2D model is suitable for simulation of Benjamin flow, especially at interfaces.

6.2 Experimental Setup

To simulate a 2D mixed-flow type problem, an experimental study was conducted to provide the information of cavity front positions and water surface profile. Experimental tests were conducted on a physical model that can be observed in Figure 6.1. A 75 cm × 75 cm × 9.3 cm plexiglass box was made and a static cubic column of water (15 cm × 15 cm × 9.3 cm) was situated in one corner of the box. To generate the pressurized flow, we used another plexiglass sheet on top of the water column. For better flow visualization purposes the material used for the walls, roof and bottom was plexiglass. To impede the water flow, an L-shape gate was installed at the open end of the pressurized part initially.

The downstream part of the box bottom was initially dry, and experimental setup was installed on a horizontal slope. We observed a full dam-break problem after instantaneous opening of the L-shape gate. Three cameras were used to cover the flow during the experiments (two for the side view and one for top view).

6.3 Numerical Model

In this section, we present the mathematical equations of our model for 2D mixed-flow and give the details of the numerical model.

6.3.1 Basic equations

2D Benjamin flow consists of free surface flow, interface flow, and pressurized flow. Figure 6.2 shows the different regions of flow in 2D Benjamin flow. Fundamental continuity and momentum equations are used to simulate the 2D Benjamin flow under the experimental conditions. The basic equations in this study are as follow:

6.3.1.1 Free surface flow

A Two-dimensional shallow water equations also called St. Venant equations were used for unsteady free surface flow. In this study, the hydrostatic pressure distribution was assumed to derive these equations. Continuity and momentum equations for free surface flows can be derived by

$$\frac{\partial h}{\partial t}+\frac{\partial M}{\partial x}+\frac{\partial N}{\partial y}=0 \tag{6.1}$$

$$\frac{\partial M}{\partial t}+\frac{\partial uM}{\partial x}+\frac{\partial vM}{\partial y}=-gh\frac{\partial h}{\partial x}-\frac{\tau_{bx}}{\rho} \tag{6.2}$$

$$\frac{\partial N}{\partial t}+\frac{\partial uN}{\partial x}+\frac{\partial vN}{\partial y}=-gh\frac{\partial h}{\partial y}-\frac{\tau_{by}}{\rho} \tag{6.3}$$

where h = the flow depth; u = the flow velocity in the x-direction; v = the flow velocity in the y-direction; M and N = discharge flux vectors which are defined as $M = uh$ and $N = vh$; g = the acceleration due to gravity; ρ = the water density; t = the time; and τ_{bx} and τ_{by} = wall shear stress vectors in x and y-direction, respectively.

$$\tau_{bx}=\frac{\rho g n^2 u\sqrt{u^2+v^2}}{h^{1/3}} \tag{6.4}$$

$$\tau_{by}=\frac{\rho g n^2 v\sqrt{u^2+v^2}}{h^{1/3}} \tag{6.5}$$

where n is the Manning roughness coefficients.

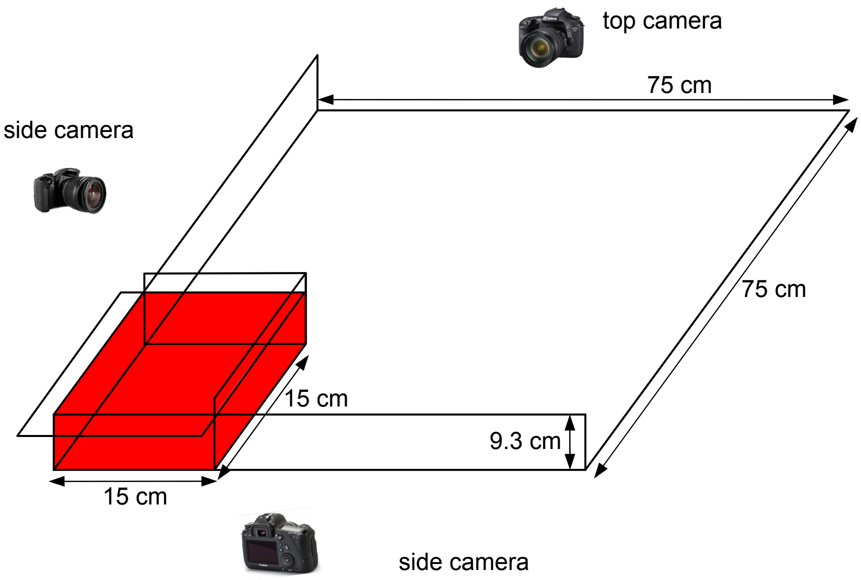

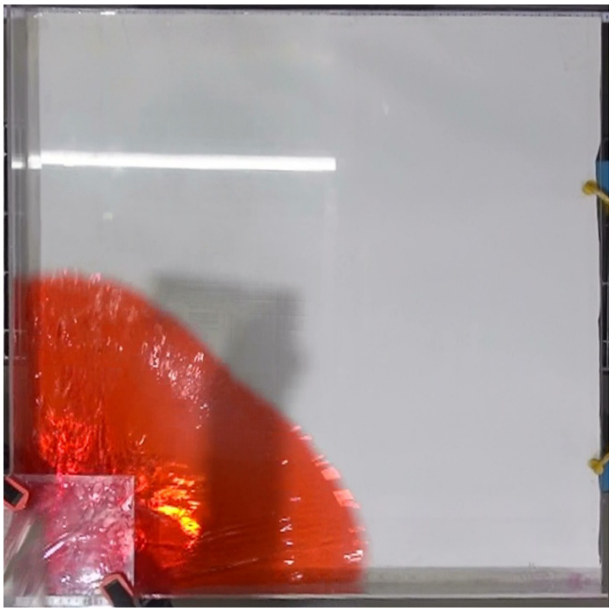

top view

side view

Figure 6.1: Experimental model of 2D Benjamin flow.

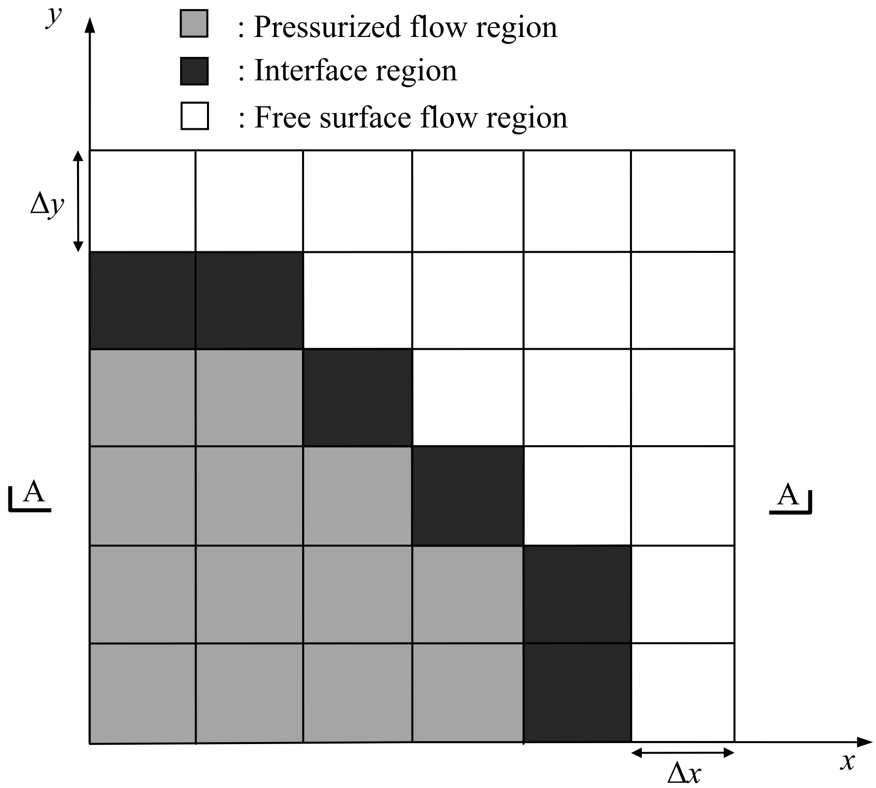

Figure 6.2: Top view of flow regions in 2D Benjamin flow (Free surface flow, interface flow, and pressurized flow).

6.3.1.2 Pressurized flow

The continuity and momentum equations in x and y-directions are followed by

$$\frac{\partial uH}{\partial x}+\frac{\partial vH}{\partial y}=0 \tag{6.6}$$

$$\frac{\partial uH}{\partial t}+\frac{\partial Hu^2}{\partial x}+\frac{\partial Huv}{\partial y}=-\frac{H}{\rho}\frac{\partial P_H}{\partial x}-gH\frac{\partial H}{\partial x}-2\frac{\tau_{bx}}{\rho} \tag{6.7}$$

$$\frac{\partial vH}{\partial t}+\frac{\partial Huv}{\partial x}+\frac{\partial Hv^2}{\partial y}=-\frac{H}{\rho}\frac{\partial P_H}{\partial y}-gH\frac{\partial H}{\partial y}-2\frac{\tau_{by}}{\rho} \tag{6.8}$$

where H = the initial flow depth (pressurized region); and P_H = pressure beneath the roof.

6.3.1.3 Interface flow

The side view of A-A section in Figure 6.2 is shown in Figure 6.3. The equations of motion for interface c in x and y-direction are derived by integrating of Equations (6.2) and (6.7) from $x_{i-1/2}$ to $x_{i+1/2}$ and Equations (5.3) and (5.9) from $y_{j-1/2}$ to $y_{j+1/2}$, respectively.

$$\frac{\partial M}{\partial t}\Delta x+(uM)_{x_{i+1/2}}-(HM)_{x_{i-1/2}}+\frac{\partial vM}{\partial y}\Delta x= \\ -g\left(\frac{h^2}{2}\right)_{x_{i+1/2}}+\left(H\frac{P_H}{\rho}+\frac{gH^2}{2}\right)_{x_{i-1/2}}-gH-\left(\frac{\tau_{bx}}{\rho}\right)_{x_i}\frac{3\Delta x}{2} \tag{6.9}$$

$$\frac{\partial N}{\partial t}\Delta y+(vN)_{y_{j+1/2}}-(HN)_{y_{j-1/2}}+\frac{\partial uN}{\partial x}\Delta y= \\ -g\left(\frac{h^2}{2}\right)_{y_{j+1/2}}+\left(H\frac{P_H}{\rho}+\frac{gH^2}{2}\right)_{y_{j-1/2}}-gH-\left(\frac{\tau_{by}}{\rho}\right)_{y_j}\frac{3\Delta y}{2} \tag{6.10}$$

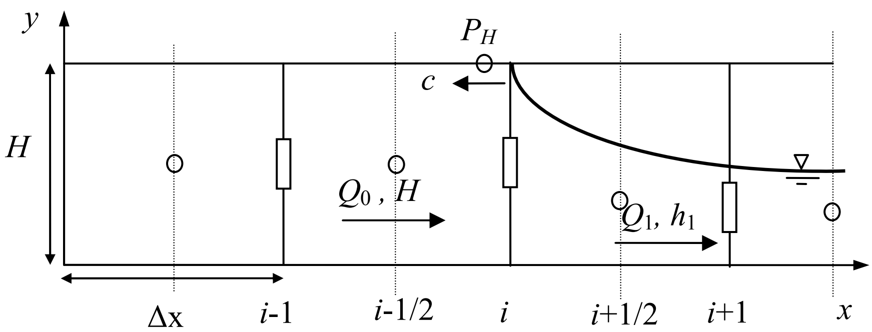

Figure 6.3: Side view of flow regions along A - A line.

6.3.1.4 Pressure drop at interfaces

Regarding previous studies, considering the pressure drops at interfaces are necessary (Bashiri-Atrabi et al., 2015a; Bashiri-Atrabi et al., 2015b). The pressure drop at an interface in 1D flow followed by:

$$\frac{P_H}{\rho g}=H-\frac{c^2}{2g} \tag{6.11}$$

$$c = \kappa \frac{Q_0 - Q_1}{A_a}; \qquad \kappa = 0.5 \tag{6.12}$$

where c is the celerity of cavity; Q_0 and Q_1 are the discharge of water upstream and downstream of a cavity, respectively; and κ is a constant pressure drop coefficient.

For determination of pressure drop at interfaces for 2D Benjamin flow, we considered three cases. As Figure 6.4 shows, we divided the cases based on the alignment of cells. For 2D flow, we used average values for $Q_0 - Q_1$ and A_a in Equation (6.12). The procedure of considering the pressure drop at the interfaces for 2D Benjamin flow consists of below steps:

1. Determination of interface cells between pressurized and free surface flows
2. Determination of cells situation around the interface cells (four cells around each cell)
3. Calculate an average water depth and discharge around each interface cell
4. Calculate the pressure drop

```
% JEND AND IEND: BOUNDARY CELLS
     DO 77 J = 1, JEND
     DO 88 I = 1, IEND
% INTERFACE BETWEEN PRESSURIZED AND FREE SURFACE FLOW: IHB(I,J).EQ.1
       IF(IHB(I,J).NE.1)THEN
% HPDAM(I,J): VALUE OF PRESSURE DROP AT THE INTERFACE CELL
        HPDAM(I,J)=0.D0
        GOTO 88
       ENDIF

       IF(IHB(I,J).EQ.1) THEN
% INN=0: NORTH CELL IS FREE SURFACE
        INN=0
% INE=0: EAST CELL IS FREE SURFACE
        INE=0
% INW=0: WEST CELL IS FREE SURFACE
        INW=0
% INS=0: SOUTH CELL IS FREE SURFACE
        INS=0

        IF(J.LE.JEND-1 .AND. IHB(I,J+1)==0) INN=1
        IF(I.LE.IEND-1 .AND. IHB(I+1,J)==0) INE=1
        IF(I.GE.2      .AND. IHB(I-1,J)==0) INW=1
        IF(J.GE.2      .AND. IHB(I,J-1)==0) INS=1
```

```
        IF(INN+INE+INW+INS==0)THEN
         HPDAM(I,J)=H(I,J)
        ELSE

% HN: AVERAGE OF WATER DEPTH IN NORTH DIRECTION
         HN=REAL(INN)*(H(I,J+1)+H(I,J+2)+H(I,J+3))/3.D0
% HS: AVERAGE OF WATER DEPTH IN SOUTH DIRECTION
         HS=REAL(INS)*(H(I,J-1)+H(I,J-2)+H(I,J-3))/3.D0
% HE: AVERAGE OF WATER DEPTH IN EAST DIRECTION
         HE=REAL(INE)*(H(I+1,J)+H(I+2,J)+H(I+3,J))/3.D0
% HW: AVERAGE OF WATER DEPTH IN WEST DIRECTION
         HW=REAL(INW)*(H(I-1,J)+H(I-2,J)+H(I-3,J))/3.D0

% DQN: AVERAGE OF DISCHARGE IN NORTH DIRECTION
         DQN=REAL(INN)*(FY(I,J)-FY(I,J+2))
% DQS: AVERAGE OF DISCHARGE IN SOUTH DIRECTION
         DQS=REAL(INS)*(FY(I,J-1)-FY(I,J+1))
% DQE: AVERAGE OF DISCHARGE IN EAST DIRECTION
         DQE=REAL(INE)*(FX(I,J)-FX(I+2,J))
% DQW: AVERAGE OF DISCHARGE IN WEST DIRECTION
         DQW=REAL(INW)*(FX(I-1,J)-FX(I+1,J))

% Equation (6.12); DA: DUCT HEIGHT
         CN=1.D0*DQN/(DA-HN)
         CS=1.D0*DQS/(DA-HS)
         CE=1.D0*DQE/(DA-HE)
         CW=1.D0*DQW/(DA-HW)

         IF(INN+INS/=0.AND.INW+INE/=0)THEN
         CCC =((ABS(CN+CS)/REAL(INN+INS))
     1            +(ABS(CE+CW)/REAL(INE+INW)))
         ELSEIF(INN+INS/=0)THEN
         CCC =((ABS(CN+CS)/REAL(INN+INS)))
         ELSE
         CCC =((ABS(CE+CW)/REAL(INW+INE)))
         ENDIF

% Equation (6.11)
         DQ=CCC*CCC/2.D0/G
         HPDAM(I,J)=DA-(PARAP*DQ)

         IF(HPDAM(I,J).GE.0.D0.OR.HPDAM(I,J).LT.DA) THEN
          HP(I,J) = HPDAM(I,J)
         ELSE
          HP(I,J) = H(I,J)
         END IF

        ENDIF

      ENDIF
  88 CONTINUE
        77 CONTINUE
```

6.3.2 Numerical considerations

A Cartesian staggered grid system was used for calculation of the flow. According to Figure 6.5, which shows a staggered grid system in x and y-direction, the pressure and depth nodes lie at the cell centers and the velocity and flux are defined at each cell face. The convective flux was evaluated by a finite volume first-order upwind scheme. The first order explicit Euler method was used for time integration of fluxes. The HSMAC method was used for correction of pressure and velocity in the pressurized part (Hirt and Cook, 1972). Supposing that M, N and P_H are known at $t = n \cdot \Delta t$, the hydraulic variables at $t = (\mathrm{n}+1) \cdot \Delta t$ are calculated by following steps:

- M* and N* are recalculated by

$$\frac{M^{*}-M^{n}}{\Delta t}=-(\text{inertia})^{n}-(\text{pressure})^{n}-(\text{wall shear})^{n} \tag{6.13}$$

$$\frac{N^{*}-N^{n}}{\Delta t}=-(\text{inertia})^{n}-(\text{pressure})^{n}-(\text{wall shear})^{n} \tag{6.14}$$

- The pressure in full pipe region (P_H) is corrected by

$$P_H^{*}=P_H^{n}+\delta P_H^{*} \tag{6.15}$$

where P_H^* is the corrected pressure; and δP_H^* for $P_{H_{i+1/2,j+1/2}}$ is calculated by

$$\delta P_{H_{i+1/2,j+1/2}}^{*}=-\frac{\omega\varepsilon^{*}}{2D\Delta t\left(\frac{1}{\Delta x^{2}}+\frac{1}{\Delta y^{2}}\right)} \quad , \quad \omega=0.5 \tag{6.16}$$

- M* and N* are recalculated by substituting into Equations (6.13) and (6.14), respectively. If $\left|\varepsilon^{*}\right|$ < er (criterion error), then M* and N* are considered as M^{n+1} and N^{n+1} at $t = (n+1).\Delta t$, otherwise the same procedure is continued until $\left|\varepsilon^{*}\right|$ < er. The depth and cavity front positions at $t = (n\text{-}1/2).\Delta t$ and M, N at $t = \mathrm{n}.\Delta t$ are known. The depth of free surface region at $t = (n+1/2).\Delta t$ is calculated by Equation (6.1). If $h^{n+1/2} > H$, then the control volume regarded as pressurized flow region, otherwise considered as a free surface region and a new position of an interface is determined.

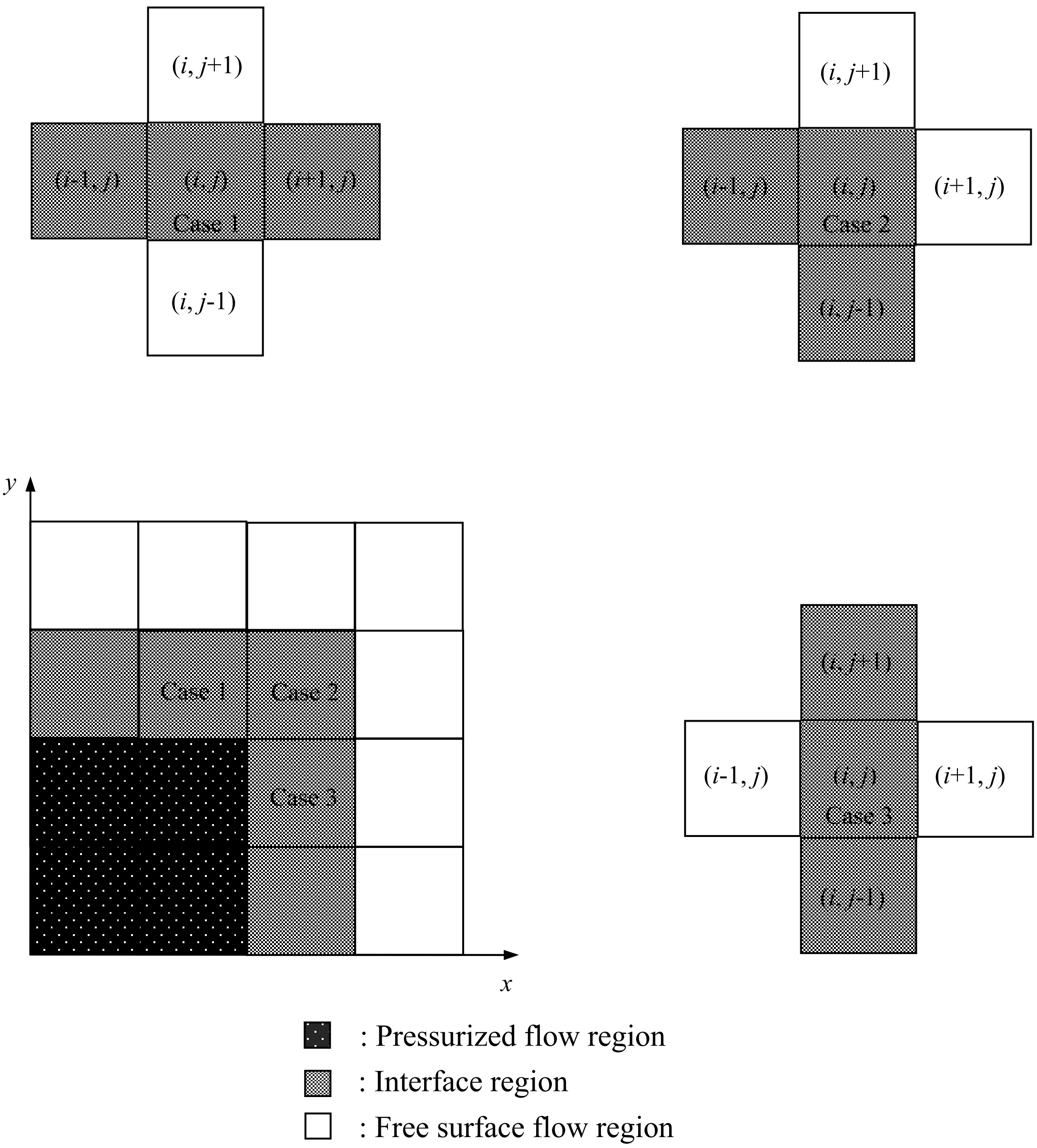

Figure 6.4: Procedure of pressure drop at interfaces in 2D flow.

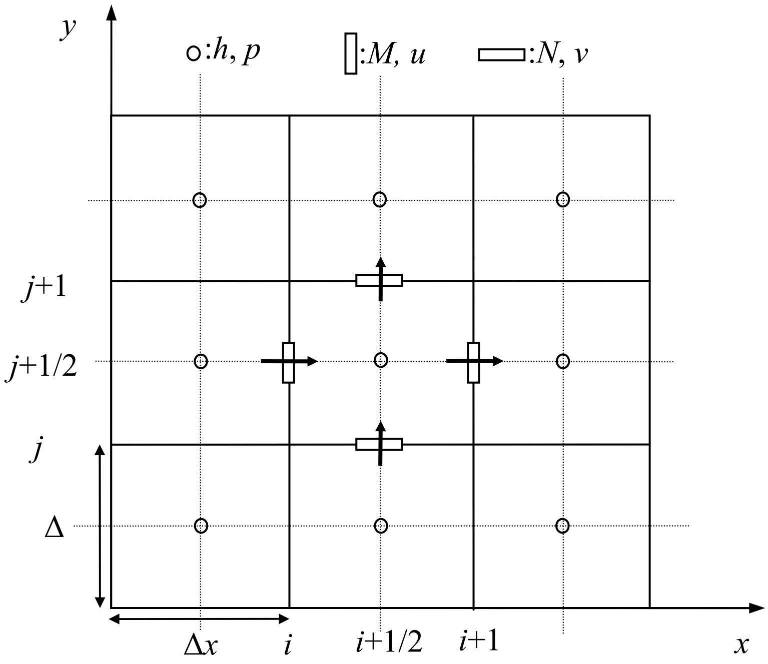

Figure 6.5: 2D Cartesian staggered grid system.

6.4 Results

The numerical algorithm described in the previous section is validated by comparing the numerical results with the experimental data for the surface profile and cavity front position. The numerical computations were performed with $\Delta x = 0.005$ m, $\Delta y = 0.005$ m, $\Delta t = 0.0005$ s, and $n = 0.01$ $m^{-1/3}s$. The bed slope was equal to zero in all the computations. Figure 6.6 shows computed results without considering the pressure drops at air-water interfaces at $t = 0.0333$ and 0.2 s. To avoid the gap between simulated cavity front position and experimental data, especially in the pressurized region, adding sufficient pressure drop at interfaces was necessary as Equation (6.12).

Results with a pressure drop ($\kappa = 0.5$) are shown in Figure 6.7. As Figure 6.7 shows, cavity front without using pressure drop will vanish soon. Figure 6.8 shows the water surface profile with and without using pressure drop. Based on this Figure, it is necessary to take into account the pressure drops at interfaces for getting better results.

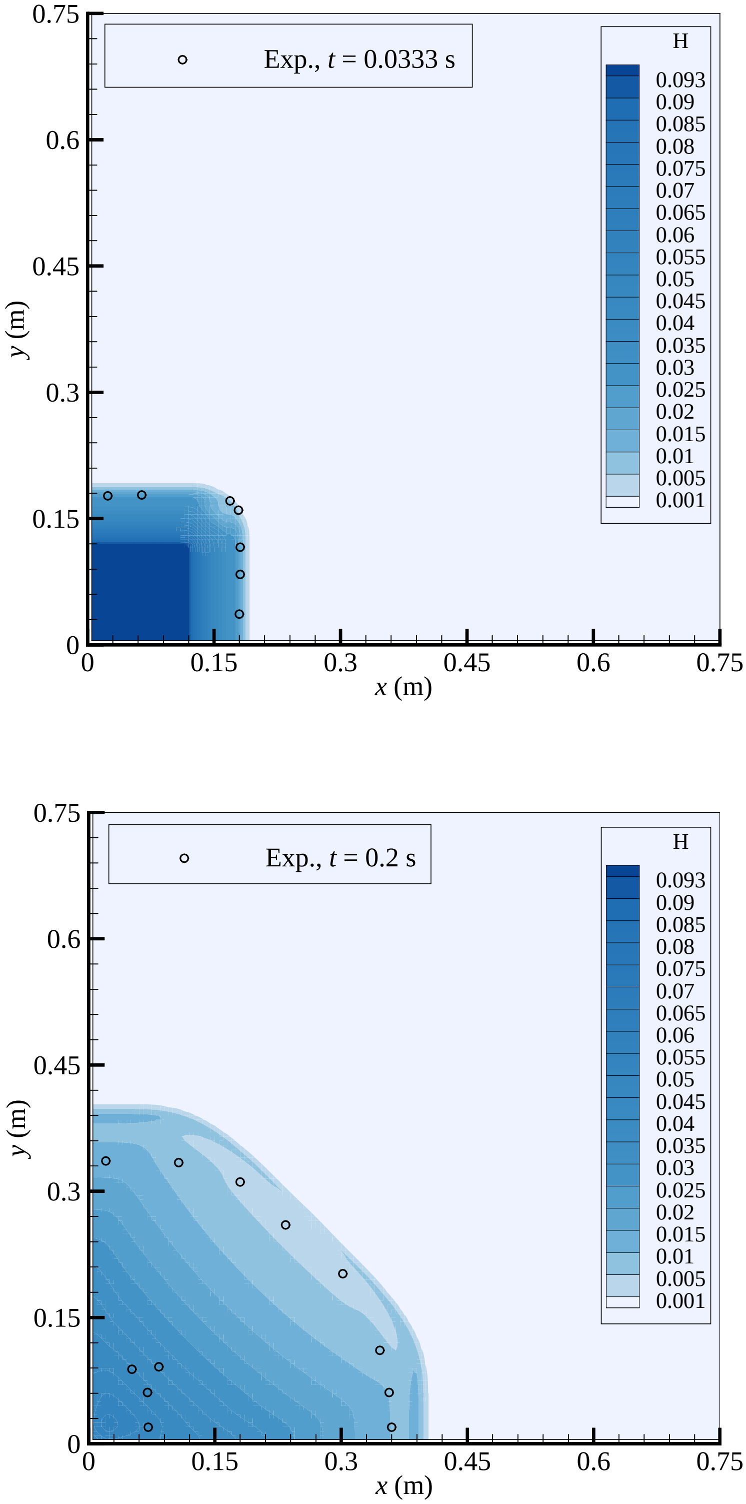

Figure 6.6: Comparison between experimental and numerical results without pressure drop consideration; $\kappa = 0$ (top view).

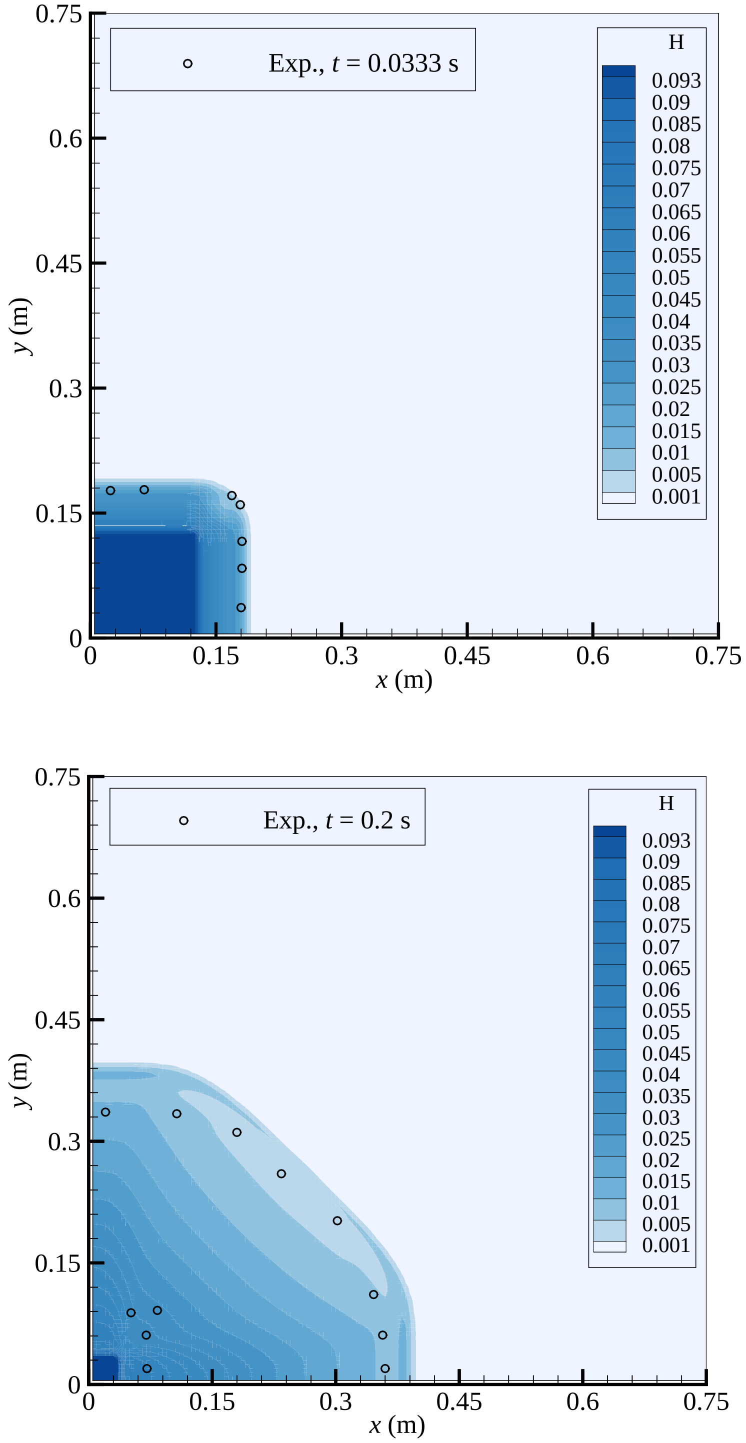

Figure 6.7: Comparison between experimental and numerical results with pressure drop consideration; $\kappa = 0.5$ (top view).

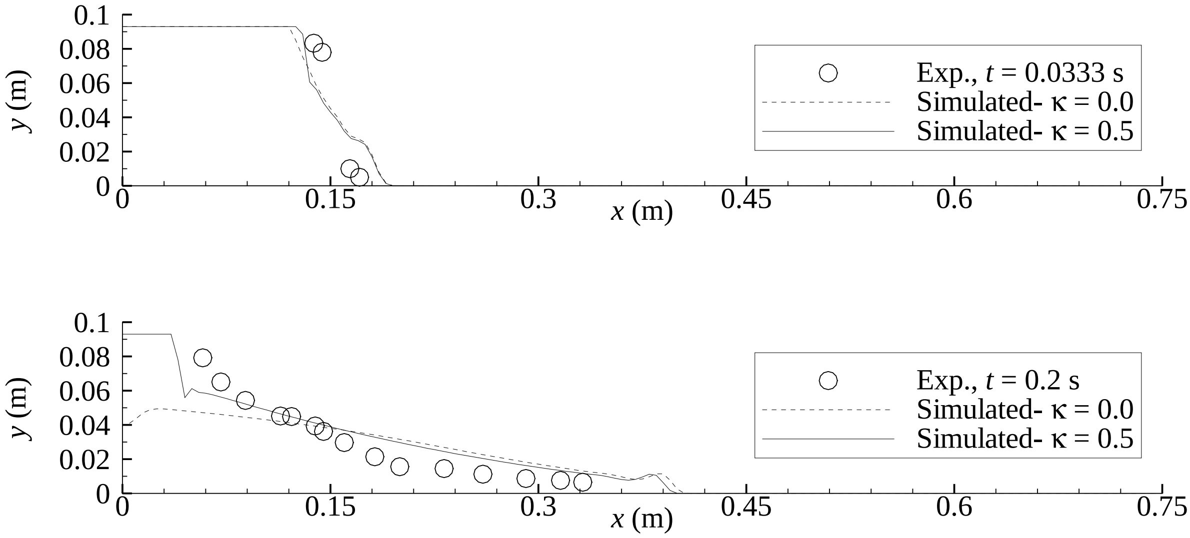

Figure 6.8: Simulated and experimental data of water surface profile (κ = 0 and 0.5).

Although these results are relatively good, non-hydrostatic models can reproduce more accurate water surface profile, especially near the cavity front. Non-hydrostatic model (Boussinesq model) can reproduce a continuous profile in front of the cavity and also simulate undular bore on the water surface. By adding eddy viscosity term and surface tension into the right-hand side of the momentum equation, we can get better agreement with experimental data for cavity front positions.

6.5 Summary

The objective of this chapter was to simulate the 2D pressurized-free surface flow in a square box. For an observation of this kind of flow, a few experiments were conducted, and cavity front positions and water surface profile data were extracted using recorded videos. A 2D model based on the finite volume method in a staggered grid system was developed to model the experiments. In this study, a hydrostatic pressure assumption was implemented, and fundamental continuity and momentum equations were used for pressurized, free surface and interface regions. A pressure drop model was developed at interfaces. The HSMAC and the flood invasion (Inoue, 1986) methods were used for pressurized and free surface flow, respectively.

For an evaluation of the numerical method, experimental data compared with simulated results with considering the pressure drop at interfaces and neglecting it. As numerical results showed it is necessary to use pressure drop strategy at interfaces and select a proper pressure drop coefficient, otherwise the cavity front positions and water surface profiles are not matched with the experimental data. This model is applicable for simulation of 2D transient flow from pressurized to free surface flow. Further experimental and numerical researches are necessary for developing more accurate models for pressure drop at interfaces and water surface profile.

6.6 References

Baines, W. D. (1991). "Air cavities as gravity currents on slope." *J. Hydraul. Eng.*, 117 (12), 1600–1615.

Bashiri-Atrabi, H., Shirai, H., and Hosoda, T. (2015a). "Experimental and numerical analysis of air cavity intrusion in a horizontal circular pipe." *Journal of Japan Society of Civil Engineers, Ser. B1 (Hydraulic Engineering),* 71 (4), 181_I-186_I.

Bashiri-Atrabi, H., Hosoda, T., and Tada, A. (2015b). "Simulation of air cavity advancing into a straight duct." *J. Hydraul. Eng.,* 141 (1), 04014068.

Benjamin T. B. (1968). "Gravity currents and related phenomena." *J. Fluid Mech.*, 31 (2), 209–248.

Fennema, R. J., and Chaudhry, M. H. (1990). "Explicit methods for 2-D transients free-surface fellows." *J. Hydraul. Eng.*, 116 (8), 1013–1034.

Hirt, C. W., and Cook, J. L. (1972). "Calculating three-dimensional flows around structures and over rough terrain." *J. Comput. Phys.*, 10 (2), 324–340.

Inoue, K., (1986). "Studies on the numerical methods of the unsteady flows in open channels and their applications in hydraulic engineering.” Ph.D. dissertation, Kyoto University, Japan (in Japanese).

Sharifi, E., Unami, K., Mohawesh, O., Nakamichi, T., Kinjo, N., and Fujihara, M. (2015). Design and construction of a hydraulic structure for rainwater harvesting in arid environment. *Proceedings of the 36th IAHR World Congress*, 28 June-3 July, The Hague, the Netherlands.

Unami, K., Tawachi, K., Babar, M. M., and Itagaki, H. (1999). “Two-dimensional numerical model of spillway flow.” *J. Hydraul. Eng.,* 125 (4), 369–375.

Wilkinson, D. L. (1982). “Motion of air cavities in long horizontal ducts.” *J. Fluid Mech.*, 118, 109–122.

Yoon, T. H. and Kang, S-K. (2004). “Finite volume model for two-dimensional shallow water flows on unstructured grids.” *J. Hydraul. Eng.*, 130 (7), 678–688.

Zhao, D. H., Shen, H. W., Tabios, G. Q., Lai, J. S., and Tan, W. Y. (1994). “Finite-volume two-dimensional unsteady-flow model for river basins.” *J. Hydraul. Eng.*, 116 (8), 863–883.

Chapter 7

Conclusions

7.1 Summary of Findings

To understand and simulate the fundamental characteristics of transient mixed flows in rectangular and circular ducts, several experimental and numerical studies have been developed. Firstly, we developed one-dimensional hydrostatic and Boussinesq models to simulate the transient flow from pressurized to free surface flow. We showed that an analytical solution can reproduce the air cavity profile inside a rectangular duct. Results showed that it is necessary to consider the air pressure change inside a confined cavity to reproduce the cavity profile.

In the case of a circular pipe, we conducted some experiments to observe the different types of flow and analyze them. We also derived a Boussinesq equation for depth greater than the radius and simulated the profiles using hydrostatic and non-hydrostatic models. To understand the characteristics of 2D Benjamin bubble, we conducted some experiments and simulated the transient mixed flow with a 3D model. Also, we developed a 2D model and considered a pressure drop model at the interface between pressurized and free surface flow. The summary of these studies is concluded below under the respective topics.

7.1.1 One-dimensional depth-averaged model

In this chapter, we studied mixed flows in horizontal and inclined rectangular ducts. We proposed hydrostatic and Boussinesq models to simulate the different types of cavity advancing into a rectangular duct. Numerical simulations were examined by some previous experimental data. Results showed that it is necessary to use a pressure drop equation at the interface for better agreement with the observed stagnation points.

We showed that a solitary wave solution could reproduce the air cavity profile. In contrast to the Hydrostatic model, the Boussinesq model showed better agreement with the experimental data and the solitary wave solution. To examine the ability of Boussinesq model for the generation of undular bores, we also used a damping function.

7.1.2 The motion of confined cavity in an inclined duct

In the case of confined cavity, we developed a 1D model with considering the air pressure change inside the confined cavity (Boyle's law) and also used a pressure drop at the interface. Comparisons of numerical results with experimental data showed that this model can be used for the simulation of an entrapped cavity in a rectangular duct. To simulate the confined air, it is necessary to consider the pressure drop in front of the confined air cavity; otherwise the confined air cavity vanishes rapidly. While emptying duct, the confined air cavity can be modeled through Boyle's law.

7.1.3 Air cavity intrusion in circular pipes

Transient one-dimensional flow with the propagation of an interface between the open channel free surface flow and the pressurized pipe flow had studied experimentally and numerically in chapter 4. The comparisons of numerical results with the experimental data lead to the following conclusions:

(1) Theoretical analysis showed a good agreement with the experimental results.

(2) The numerical simulation results showed that to reproduce the air intrusion in the pipe, it is necessary to consider the pressure drop at the interface.

(3) It should be pointed out that the model is applicable to simulate the hydraulic

transients in horizontal and inclined circular pipes.

(4) In the case of circular cross-section, although the results showed that the both hydrostatic and Boussinesq model can reproduce the air cavity front shape, but the non–hydrostatic model had better agreement with the experimental data.

(5) Boussinesq model is applicable to reproduce the undular bore in circular pipes.

7.1.4 Three-dimensional simulation of transient mixed flows

In this section, we studied the propagation of a 2D air cavity in transient pressurized-free surface flow in a channel of square cross-section experimentally and numerically. We conducted two series of experiments in which we measured the front positions and water surface profiles. The aim of conducting two sets of experiments was observation of Benjamin bubble in two directions and compare the results with the simple dam-break problem. The fresh water and air were selected as two-phase flow in the experiments. 3D computation with URANS-type turbulence model was developed and verified trough a series of test problems. This model was compared with the 1D non-hydrostatic model. The model utilized the full staggered grid system and applied the FVM scheme to the continuity and the momentum equations.

The computational results for the problems pointed acceptable accuracy of the 3D URANS model to a wide range of mixed flow problems in a rectangular duct. The positions of interfaces, front positions of free surface flow, and water surface profiles were quite well simulated. Although the 1D Boussinesq model showed good results in the first case, it has limitations in simulating the complex transient flows. For the simulation of 1D Benjamin bubble, the 1D model has superiority in less consumption of time, and economic cost compare to the 3D model.

Finally, it was concluded that the 3D model was more stable and sufficiently accurate.

7.1.5 A two-dimensional depth-averaged model for mixed flows

The objective of this chapter was to simulate the 2D pressurized-free surface flow in a square box. For an observation of this kind of flow, a few experiments were conducted, and cavity front positions and water surface profile data were extracted using recorded videos. A 2D model based on the finite volume method in a staggered grid system was developed to model the experiments. In this study, a hydrostatic pressure assumption was implemented, and fundamental continuity and momentum equations were used for pressurized, free surface and interface regions. A 2D pressure drop model was developed at interfaces. The HSMAC and the flood invasion methods were used for pressurized and free surface flow, respectively.

For an evaluation of the numerical method, experimental data compared with simulated results with considering the pressure drop at interfaces and neglecting it. As numerical results showed it is necessary to use the pressure drop strategy at interfaces and select a proper pressure drop coefficient, otherwise the cavity front positions and water surface profiles are not matched with the experimental data. This model is applicable for simulation of 2D transient flow from pressurized to free surface flow.

7.2 Recommendation for Future Studies

Based on the numerical results of proposed models, this research leads to following recommendations for the future works:

Although a good agreement between the model results and the observations tends to validate the proposed models, further studies are essential to illustrate the advantages or disadvantages of the fundamental model in comparison with other numerical models. Also, it is necessary to investigate the undular bore with partial breaking using a refined Boussinesq equation, although a simple model was proposed by authors.

For the two-dimensional model, it is necessary to propose different pressure drop models to reproduce the better water surface profile and stagnation points.